

Raman Imaging of Small Atomic Ensembles Inside an Optical Cavity

Maximilian Ammenwerth

Masterarbeit in Physik
angefertigt im Institut für Angewandte Physik

vorgelegt der
Mathematisch-Naturwissenschaftlichen Fakultät
der
Rheinischen Friedrich-Wilhelms-Universität
Bonn

August 2020

I hereby declare that this thesis was formulated by myself and that no sources or tools other than those cited were used.

Bonn,
Date

.....
Signature

- 1. Gutachter: Prof. Dr. Dieter Meschede
- 2. Gutachter: Prof. Dr. Simon Stellmer

Contents

1	Introduction	1
1.1	The Experimental Apparatus	3
1.2	Cavity-Based State Detection	4
2	Differential Light Shifts During Continuous Raman Sideband Cooling	7
2.1	Raman Spectroscopy in Optical Dipole Traps	7
2.2	Resolved Raman Sideband Cooling	10
2.2.1	Continuous versus Pulsed Raman Sideband Cooling	10
2.3	Light Shifts Induced by the Near-Resonant Optical Pumping Beams	11
2.3.1	Detecting the Light Shifted Sideband Frequency	12
2.3.2	Model for Continuous Raman Sideband Cooling	13
2.3.3	Systematic Characterization of Differential Light Shifts	15
2.3.4	Cooling Efficiency as Function of Repumper Detuning	20
3	Raman Imaging of Atoms in an Optical Cavity	23
3.1	New Imaging System	24
3.2	Optimizing the Raman Imaging	25
3.2.1	Optimization of the Signal-to-Noise Ratio	26
3.2.2	Resonant versus Off-Resonant Repumping	27
3.3	Towards Counting of Atoms	29
4	Photon Generation in an Atom-Cavity System	33
4.1	Photon Generation in the Adiabatic Regime	34
4.2	High-Bandwidth Photon Generation beyond the Adiabatic Regime	36
4.3	Chirp Compensation with Polychromatic Driving Fields	39
4.3.1	Adiabatic Approximation	40
4.3.2	Chirp Compensation.	43
4.4	Photon Generation in a Two-Mode Cavity with Multilevel Atoms	45
5	Summary and Outlook	47
	Bibliography	49
A	Photon Generation in the Adiabatic Regime	57
B	Describing Photon Generation with an Effective Operator Formalism	61
B.1	Extension to a two-tone driving field	63

Introduction

Experimental research in the field of atomic physics has seen tremendous progress over the past decades which was triggered by the development of precise lasers [1, 2]. Pre-cooled by magneto-optical traps [3] and confined by optical dipole potentials [4], ensembles of neutral atoms can be isolated and their internal state can be manipulated with laser light [5]. Advanced laser cooling techniques, such as polarization gradient cooling [6] or Raman sideband cooling [7, 8] have in addition enabled control over the motional degrees of freedom. These techniques have facilitated the study of intriguing quantum effects such as superposition and entanglement [9, 10].

Nowadays we are not only able to control quantum systems to an unprecedented precision [11], but also envisage to exploit their fascinating properties for new quantum technologies [12]. Possible applications range from quantum key distribution [13], over precision measurements and sensing [14] to quantum simulations of many-body physics [15, 16]. These applications are based on precise and coherent control over individual quantum states. Using these quantum states in interconnected remote quantum devices motivates the development of methods for transmitting quantum states in quantum networks [17]. Here, we consider that different quantum nodes which are able to process [18] and store [19] quantum states are connected via single-mode optical fibers. In order to transmit quantum information the nodes exchange single photons which are the ideal information carrier (also called “flying qubit”), since they interact only weakly with the environment and travel at the speed of light. However, inevitable losses along the path limit the range of these point-to-point connections, since direct amplification is prohibited by the No-Cloning theorem [20]. Transmitting quantum states directly over more than a few hundred kilometres is thus impractical and one has to make use of quantum teleportation protocols [21]. The latter is based on sets of entangled quantum emitter pairs being shared between the sending and the receiving nodes. Thus, entanglement can be considered as a resource required for the operation of a quantum network. Quantum repeater technology can be used to distribute entanglement over large distances using intermediate nodes [22]. Reliable fiber-based quantum network operation, therefore, depends on highly efficient light-matter interfaces that allow for transferring the quantum information from the “stationary qubit” of the quantum memory onto a single photon and vice-versa.

In our experiment, we employ ^{87}Rb -atoms coupled to an optical high-finesse Fiber Fabry-Pérot cavity that serves as light-matter interface. When coupled to the resonator mode, the emission properties of the atoms are modified by the Purcell-effect that enhances the emission into the mode of the resonator compared to free-space emission [23] and which facilitates the coupling of a neutral

atom to a fiber-based network. Besides neutral atoms, other platforms such as semiconductor quantum dots [24, 25], color centers [26] or ions [27] are currently being explored as potential platforms for quantum repeaters. Different emitter platforms have their own (dis-)advantages and differ considerably in terms of achievable repetition rate and transition linewidth 2γ of the used emitter. Interconnecting different emitters to a hybrid network requires matching the spectral width of temporally short photons with the finite emitter bandwidth. This can be done by shaping the temporal wavefunction of the generated photons [28] and in addition exploiting the Purcell-enhancement to increase the bandwidth of the coupled emitter-cavity system [29]. The latter makes use of “open” cavities with linewidth 2κ exceeding the atomic linewidth ($\kappa \gg \gamma$). For efficient atom-light interaction it is required that the atom-cavity coupling strength g exceeds the decay rates of the system ($g \geq \kappa \gg \gamma$) [23]. The coupling strength $g \propto \frac{1}{\sqrt{V}}$ is inversely proportional to the square-root of the mode-volume V which motivates the use of miniaturized fiber-based cavities that provide a small mode volume. The effective coupling strength $g_{\text{eff}} = \sqrt{N} \cdot g$ can be increased even further by coupling N identical atoms to the same cavity mode. Moreover, the collective coupling of small atomic ensembles to one cavity mode can be used to create multi-particle entangled states [30].

In order to facilitate experiments with more than one atom we would like to count the number of atoms inside the resonator mode by means of fluorescence imaging. The near-resonant scattering of imaging light inevitably induces heating of the atoms which has to be compensated by suitable cooling [31]. Fluorescence imaging of ^{87}Rb has been demonstrated with molasses cooling [32]. However, in our experiment we can not implement three-dimensional molasses cooling, due to the limited optical access where one direction is blocked by the cavity itself. We therefore implement Raman imaging which is based on detecting the repumper fluorescence during Raman sideband cooling and allows for exposure times exceeding 1 s [33, 34]. The (near-)resonant repumper beam induces a differential light shift onto the ground-states that are coupled via the Raman transfer and shifts the two-photon resonance. The strength of the differential light shift depends on the repumper intensity and detuning and hence the two-photon detuning can not be optimized independently. A precision measurement of repumper-induced differential light shifts is presented in chapter 2. We identify the optimal cooling parameters and confirm that near ground-state cooling is achieved. Subsequently, the Raman imaging is described in chapter 3. The improved imaging setup is introduced and the optimization of the signal-to-noise ratio is discussed. Raman imaging was successfully applied to image small atomic ensembles inside the resonator mode which is the first step towards exploring the collective coupling of multiple atoms to the resonator.

Using single-photons as information carriers in quantum networks requires precise control over their spatio-temporal wavefunction [35]. Exploring the limit of the short temporal single-photon pulse generation, we theoretically study the atom-cavity dynamics beyond the well explored adiabatic regime [36] in chapter 4. Here, we compute the photon generation fidelity for pulses of variable duration and explore the limits of adiabatic photon generation by means of numerical simulations. Prominent theoretical work on photon generation considers the atom as a Λ -system with two metastable ground-states and one electronic excited state [36–39]. We generalize this result to a Tripod level configuration [29] that takes into account a second degenerate cavity mode with orthogonal polarization. It is found that in this case the off-resonant coupling [40] to additional electronically excited states can be exploited to tune the branching ratio of photon emission into the two polarization modes. This provides means of maximizing the Bell state projection probability of entanglement distribution schemes [27, 41]. In addition, we study photon generation with a bichromatic driving field

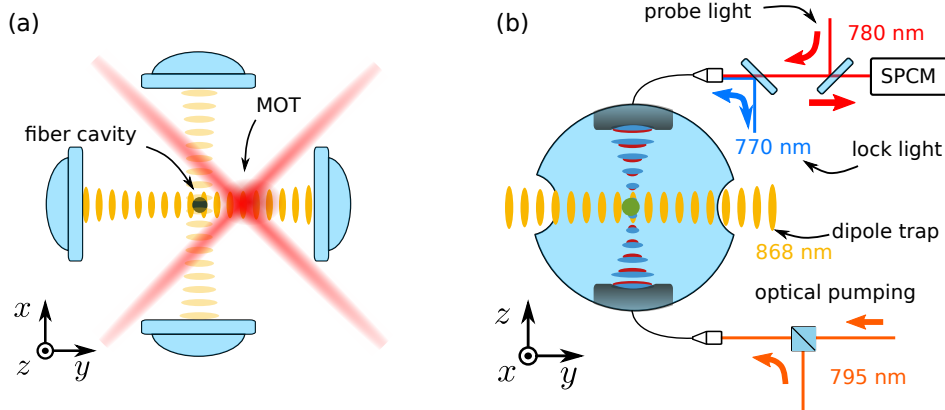


Figure 1.1: (a) Top view of the fiber cavity placed at the common focus of four in-vacuum lenses. A small magneto-optical trap (MOT) is created about 1 mm away from the cavity center. Atoms are transported into the cavity center using an optical conveyor belt. (b) Side view of the setup showing the most important laser beams. The resonance frequency of the cavity is referenced to a dedicated lock laser (770 nm). The reflection of a weak probe beam (780 nm) is monitored with a single photon counting module (SPCM). Optical pumping light (795 nm) is off-resonantly coupled through the lower cavity mirror. The atoms are trapped in a three-dimensional optical lattice. The vertical confinement is given by the blue-detuned intra-cavity lock laser lattice. Confinement along the two horizontal axes is provided by red-detuned dipole traps at a wavelength of 868 nm.

and solve the corresponding equations of motion analytically by means of an adiabatic approximation technique [42]. We find that for certain parameter choices two-tone driving can be used to suppress spurious phase-chirps originating from a time-dependent light shift induced by the control laser beam [40].

A more technical introduction to the experiment is given in the following part. The cavity-based state detection is explained and a brief introduction to the apparatus is given.

1.1 The Experimental Apparatus

Our experiment is based on a high-finesse fiber Fabry-Pérot cavity [23]. Its center is aligned with the common focus of four high NA ($NA=0.5$) lenses as sketched in Fig. 1.1(a). An experimental run starts by loading a small magneto-optical trap [43] that captures a few tens of ^{87}Rb atoms from the background vapour at a pressure of a few 10^{-10} mbar. The atoms are pre-cooled via optical molasses cooling [6] on the D2-line and subsequently transferred into a red-detuned standing wave optical dipole trap [44] at a wavelength of 868 nm. The optical lattice serves as conveyor belt [45] and is used to transport the atoms over a distance of about 1 mm into the center of the cavity. The atoms are initially cooled by means of degenerate Raman Sideband cooling (dRSC) inside the cavity [46]. This technique makes use of Raman transitions driven by the dipole traps themselves and requires a precise tuning of the Zeeman shift, which has to be equal to the spacing between adjacent motional states [47]. The resonance frequency of the cavity is actively stabilized with the Pound-Drever-Hall (PDH) technique [48] and is referenced to a dedicated laser (lock laser) operating at 770 nm. The lock laser is in turn referenced to an optical frequency comb [49, 50] and generates an intra-cavity blue-detuned lattice along the cavity. Atoms in the cavity center are thus confined in a three-dimensional optical

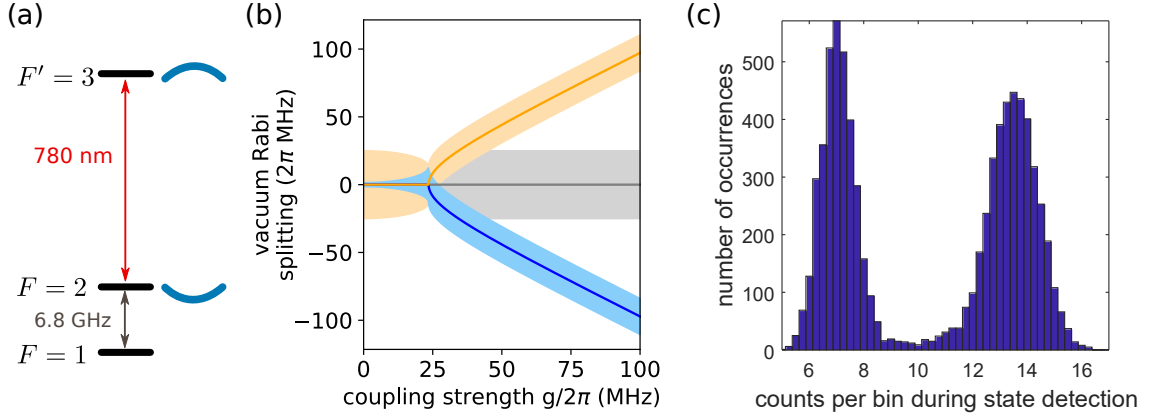


Figure 1.2: (a) Simplified level scheme of ^{87}Rb showing the two hyperfine ground states. The cavity is tuned into resonance with the $F = 2 \rightarrow F' = 3$ transition of the D2-line. (b) Eigenenergies of the coupled atom-cavity system as function of coupling strength g (blue and yellow). The shaded areas show the linewidth of the corresponding dressed state. For a coupling strength exceeding a critical point the eigenenergies split which yields the so called vacuum Rabi splitting. Atoms in the uncoupled $F = 1$ hyperfine state do not cause a splitting (grey). The state dependent coupling enables cavity-based state detection. (c) Histogram of the number of detected photons per bin during state detection. Each bin corresponds to a duration of 200 μs .

lattice. The highly reflective coatings of the two cavity mirrors are chosen to be asymmetric such that light predominantly leaves the cavity via the upper “high-transmission” (HT) mirror. The reflection of weak resonant light pulses from the HT mirror is monitored with a single photon counting module (SPCM) as shown in Fig. 1.1(b). This enables cavity-based state detection which is explained in Sec. 1.2. Optical pumping light at a wavelength of 795 nm (D1-line) is off-resonantly coupled through the lower cavity mirror.

1.2 Cavity-Based State Detection

In our experiment we use neutral ^{87}Rb atoms coupled to a high-finesse fiber Fabry-Pérot resonator [51]. The hyperfine level structure of ^{87}Rb contains two meta-stable ground-states with $F = 1$ and $F = 2$ quantum number [52] separated by an energy difference of about 6.8 GHz [53] as shown in Fig. 1.2(a). The cavity with a linewidth of about 40 MHz is tuned into resonance with the $F = 2 \rightarrow F' = 3$ transition of the D2-line which leaves the lower $F = 1$ hyperfine state uncoupled. For an atom being prepared in the upper $F = 2$ hyperfine state the system is well described by the Jaynes-Cummings Hamiltonian [54] shown in Eq. (1.1).

$$H_{\text{JC}} = \hbar\omega_a |e\rangle \langle e| + \hbar\omega_c a^\dagger a + \hbar g \left(a^\dagger |g_2\rangle \langle e| + |e\rangle \langle g_2| a \right) \quad (1.1)$$

Here ω_a (ω_c) denotes the resonance frequencies of the atom (cavity). The operator $|e\rangle \langle g_2|$ excites the atom from the ground-state $|g_2\rangle$ into the excited state $|e\rangle$ and the operator a denotes the annihilation operator of the intra-cavity field. Here the $|g_2\rangle$ state corresponds to the $F = 2$ hyperfine ground state and $|e\rangle$ corresponds to the $F' = 3$ excited state of the D2-line of ^{87}Rb . The atom-cavity coupling at rate g gives rise to new eigenstates called “dressed states” [55]. The eigenenergies of the coupled atom-cavity system are shifted by the so called vacuum Rabi splitting (VRS) which is shown in

Fig. 1.2(b) as a function of coupling strength g . The eigenenergies of the atom-like state (blue) and cavity-like state (yellow) are split in energy by an amount $2g$ for a resonant cavity ($\omega_c = \omega_a$). This splitting occurs only if the atom is prepared in the $F = 2$ ground-state which couples to the cavity mode. In order to detect the internal state of the atom, we monitor the reflection of a weak resonant beam impinging onto the cavity input mirror. If the atom is uncoupled ($F = 1$) the resonant light enters the cavity. A low count rate is measured with the SPCM, due to internal losses of the cavity. If the atom couples to the cavity ($F = 2$) the resonance is shifted by the VRS and the light is predominantly reflected yielding an enhanced count rate at the SPCM [51]. A histogram of the number of detected photons per bin is shown in Fig. 1.2(c) for a bin width of $200 \mu\text{s}$. The bimodal distribution corresponds to the two hyperfine states and enables cavity-based non-destructive state detection with high fidelity. We use this state detection technique in order to carry out experiments and probe the internal state of an atom in an experimental sequence. In addition to state detection, the same technique is used to probe the presence of an atom inside the mode of the resonator. This is done by simultaneously activating an additional repumper that optically pumps the atoms from the uncoupled $F = 1$ state into the coupled $F = 2$ hyperfine state.

The experimental setup and the cavity-based state detection technique allow us to perform experiments with neutral ^{87}Rb atoms strongly coupled to an optical resonator as will be seen in the rest of this thesis.

Differential Light Shifts During Continuous Raman Sideband Cooling

This chapter gives an introduction to Raman sideband cooling [56]. The optical pumping scheme is described and Raman spectroscopy is applied to calibrate the trap frequencies of the far-detuned optical dipole traps [57]. The calibration is used to overlap the trap frequencies of the three spatial directions [58]. This allows for cooling along all three spatial directions with a single Raman beam. Efficient three-dimensional Raman cooling facilitates experiments that reuse the same atom for multiple measurements which greatly increases the data acquisition rate. The optimization of Raman cooling is discussed and near ground-state cooling is achieved. We find that a differential light shift induced by the near-resonant optical pumping beam shifts the two-photon resonance. This hinders the independent optimization of two-photon detuning and repumper parameters. A precise characterization of the differential light shifts is carried out in order to optimize the cooling efficiency. We model the differential light shifts with a three-level system that contains the coherent Raman and repumper couplings and dissipative decay [59]. The detailed characterization is subsequently used to implement a feed-forward of the two-photon detuning. Thereby, the resonance with the Raman cooling sideband is maintained when the repumper power or repumper detuning is varied. This simplifies the optimization of Raman imaging which is discussed in chapter 3.

2.1 Raman Spectroscopy in Optical Dipole Traps

Optical dipole traps are based on the far off-resonant coupling of atomic states with laser fields [44]. The potential U_{dip} induced by an optical dipole trap scales as $\propto \Delta_{\text{DT}}^{-1}$ whereas the scattering rate scales as $\propto \Delta_{\text{DT}}^{-2}$ with the detuning Δ_{DT} . For large detunings the influence of such a trap is thus well described by an energy shift with negligible scattering rate [44].

$$U_{\text{dip}}(r) = \frac{3\pi c^2 \Gamma}{2\omega_0^3} \frac{1}{\Delta_{\text{DT}}} I(r) \quad (2.1)$$

Here the constant c denotes the speed of light, Γ denotes the transition linewidth and $\Delta_{\text{DT}} = \omega_0 - \omega_{\text{DT}}$ denotes the detuning of the dipole trap operating at frequency ω_{DT} from the atomic resonance ω_0 . The potential is proportional to the laser intensity $I(r)$ which typically follows a Gaussian envelope

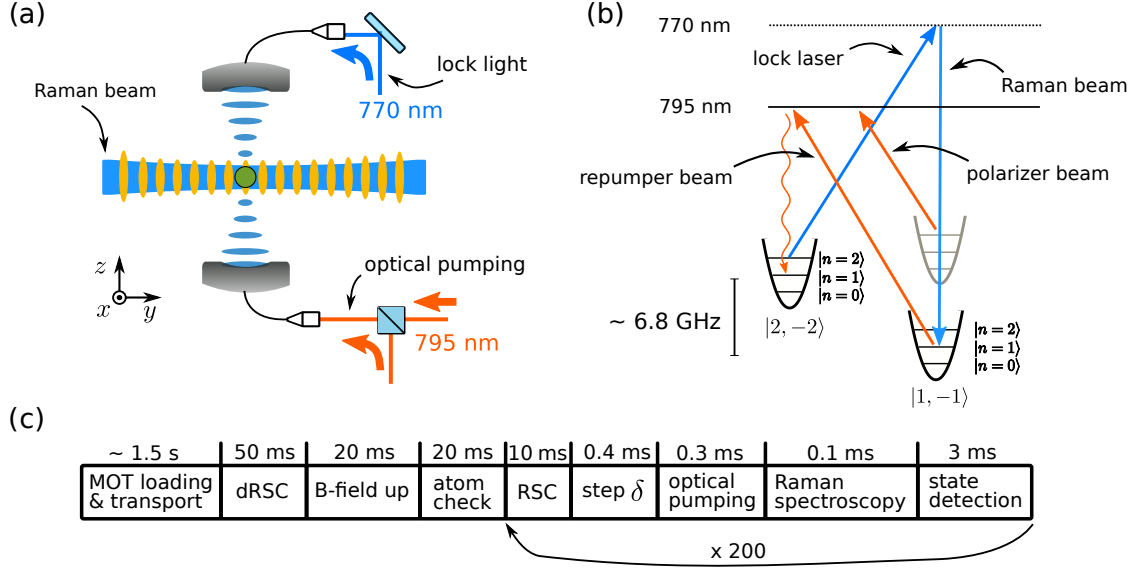


Figure 2.1: (a) A simplified sketch of the relevant beams used to trap and manipulate the atom is shown. The atom is trapped in a 3D optical lattice inside the resonator. The running wave Raman beam is shine in from the side and is phase-locked to the intra-cavity blue detuned lock laser field. Optical pumping light on the D1 transition is off-resonantly coupled through the lower cavity mirror. (b) Atomic level structure involved in the Raman process. The two-photon detuning δ is adjusted to drive transitions that lower the number of motional excitation n . Optical repumping is done with σ^- polarized light on the D1-line at 795 nm. (c) The experimental sequence used for Raman spectroscopy is shown. The atom is “recycled” 200 times for subsequent measurements.

along the radial direction. In the experiment we make use of two counter-propagating beams that interfere and form a lattice which yields an axial intensity distribution following a sin-squared shape. The trapping potential can be approximated with a harmonic potential along the tightly confining axial direction. The harmonic approximation defines the trap frequency ν that is given by Eq. (2.2). Here, U_0 denotes the potential maximum, m denotes the atomic mass and λ_{DT} denotes the wavelength of the dipole trap [60].

$$\nu = 2\pi \sqrt{\frac{2U_0}{m\lambda_{\text{DT}}^2}} \quad (2.2)$$

For sufficiently cold atomic ensembles the trapping potential is well approximated by an harmonic potential and the external degrees of freedom are given by harmonic oscillator states $|n\rangle$ ($n = 0, 1, 2, \dots$) with a certain number of motional excitations n . Adjacent motional states are separated by the trap frequency ν which is of the order of a few hundred kHz in our experiment.

In order to calibrate the trap frequencies we carry out Raman spectroscopy. After loading a single ^{87}Rb atom into the cavity as described in Sec. 1.1, we prepare the atom in the state $|F = 2, m_f = -2\rangle$ via optical pumping. To this end we apply a magnetic field of about 1.8 G in order to lift the degeneracy between different m_f states which yields a Zeeman splitting of 1.2 MHz between adjacent m_f states [52]. The magnetic field defines the quantization axis along the cavity direction which

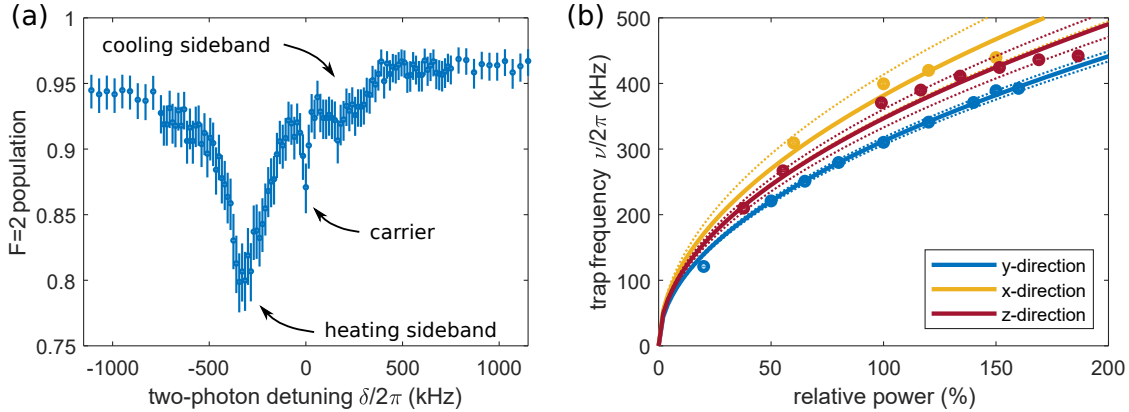


Figure 2.2: (a) Raman spectrum taken after cooling the atoms via Raman sideband cooling. The reduced depth of the cooling sideband indicates that near ground-state cooling is achieved. (b) Raman spectroscopy is used to measure the trap frequency along the three directions as function of dipole trap power. The trap frequency is shown here as function of relative power.

enables optical pumping with σ^- polarized light through the cavity mirrors. The atomic level scheme is sketched in Fig. 2.1(b) where the repumper beam couples the $F = 1 \rightarrow F' = 2$ transition of the D1-line. Thereby, atoms are pumped into the $F = 2$ hyperfine state. In order to prepare the atoms in the correct m_f -state we simultaneously activate a weak polarizer beam on the $F = 2 \rightarrow F' = 2$ transition. The state $|F = 2, m_f = -2\rangle$ is dark with respect to the σ^- polarized repumper and polarizer beam and thus the population accumulates in the desired state.

Raman transitions are driven by a linewidth-reduced distributed Bragg-reflector (DBR) laser which is phase-locked to the intra-cavity lock laser field [58]. The two-photon detuning δ of the Raman beam is adjusted to match the hyperfine splitting corrected for Zeeman shifts. After optical pumping into the state $|F = 2, m_f = -2\rangle$ for $300 \mu\text{s}$, a Raman pulse of $100 \mu\text{s}$ duration transfers the population into the state $|F = 1, m_f = -1\rangle$. We carry out Raman spectroscopy by measuring the population transfer as function of two-photon detuning δ . Restricting the analysis to the first order sidebands, we find three peaks corresponding to transitions that change the motional quantum by $\Delta n = 0, \pm 1$. The cooling sideband ($\Delta n = -1$) and the heating sideband ($\Delta n = +1$) are positioned at a relative two-photon detuning of $\delta = \pm\nu$ with respect to the carrier transition ($\Delta n = 0$) [56, 58]. Note that the carrier transition is suppressed, since one of the Raman beams also acts as blue detuned intra-cavity lattice [57]. The Raman beam propagates along the y-direction as shown in Fig. 2.1(a) and hence one would expect that sidebands corresponding to the orthogonal x-direction do not occur. It has, however, turned out that we can detect sidebands from the x-direction, because of small angles between the propagation directions [58].

We calibrate the trap frequency ν as function of dipole trap power by taking Raman spectra for different powers. The measurement is presented in Fig. 2.2(b) for the three dipole trap directions. The relative power corresponds to about 70 mW for the x- and y-trap and about $3.7 \mu\text{W}$ for the z-trap. Note that the intra-cavity field is enhanced by the cavity and thus less power is required in comparison to the horizontal dipole traps. The fits are of the form $\nu \propto \sqrt{P}$ similar to Eq. (2.2) and serve as guide to the eye. An effective trap-depth reduction due to gravitational sag can be neglected due to the deep trap depth of about 1.2 mK originating from focussing the light to a Gaussian waist of roughly $13 \mu\text{m}$.

The gravitational potential of $0.1 \mu\text{K} \mu\text{m}^{-1}$ for ^{87}Rb is thus negligible over the spatial extent of the optical dipole trap. With the trap frequency calibration at hand we overlap all trap frequencies at about 350 kHz. This simplifies the implementation of three-dimensional RSC, since a single Raman beam is sufficient to cool all spatial directions.

2.2 Resolved Raman Sideband Cooling

Efficient cooling of atoms inside the resonator makes it possible to perform multiple measurements with the same atom. This greatly reduces the amount of required measurement time, since the lengthy loading phase has to be performed less often. Raman cooling relies on coherent two-photon transitions that couple different motional states. In order to sequentially reduce the number of motional excitations by several quanta optical repumping is required as it is sketched in Fig. 2.1(b). We optimize the Raman cooling efficiency which depends on the used Raman power, the repumper power as well as the two-photon detuning and the repumper detuning. With all the three trap frequencies being overlapped we perform 3D Raman sideband cooling by tuning the two-photon detuning into resonance with the cooling sideband. We cool a single ^{87}Rb atom and subsequently perform Raman spectroscopy to evaluate the cooling performance and investigate the motional state distribution. The experimental sequence is sketched in Fig. 2.1(c). The atom is cooled by means of Raman sideband cooling for 10 ms and Raman spectroscopy is performed subsequently. One atom is reused 200 times where the two-photon detuning δ is varied for each repetition in order to carry out the Raman spectroscopy. The resulting spectrum is shown in Fig. 2.2(a). As the most dominant feature we identify the heating sideband separated by about -350 kHz from the carrier. The broad width of the heating sideband is attributed to an inhomogeneous positioning of atoms in the 3D lattice leading to a distribution of trap depth and therefore trapping frequencies. The reduced depth of the cooling sideband positioned at 350 kHz with respect to the carrier indicates that near ground-state cooling is achieved.

2.2.1 Continuous versus Pulsed Raman Sideband Cooling

During continuous Raman sideband cooling (cRSC) the optical pumping (OP) beams are activated simultaneously with the Raman beams. Alternatively, during pulsed Raman sideband cooling (pRSC) the OP beams and the Raman beams are switched on and off in an alternating manner. In this case one has to optimize the pulse durations in addition to frequencies and power levels which results in a larger parameter space. The Raman pulse duration $\tau_R = \frac{1}{2\Omega_R}$ is ideally chosen to yield a π -like transfer on the cooling sideband. In our experiment we want to cool the atom along all three spatial directions which have different Lamb-Dicke factors [57, 58]. Therefore, the Raman Rabi frequency Ω_R , which is proportional to the Lamb-Dicke factor, is different for each direction which makes it difficult to find a suitable pulse duration that yields good population transfer along all directions simultaneously.

In case of cRSC one has to optimize only the powers of Raman and OP beams and the single- and two-photon detunings. However, the (near-)resonant optical repumper beam induces a light shift onto the atomic levels. Since the $|F = 2, m_f = -2\rangle$ is dark with respect to the OP beams this light shift affects only the $|F = 1, m_f = -1\rangle$ state and thus the two-photon resonance is shifted. The strength of this differential light shift depends on the power and detuning of the repumper beam which means that the parameters are coupled and can not be optimized individually. A detailed characterization is presented in Sec. 2.3.

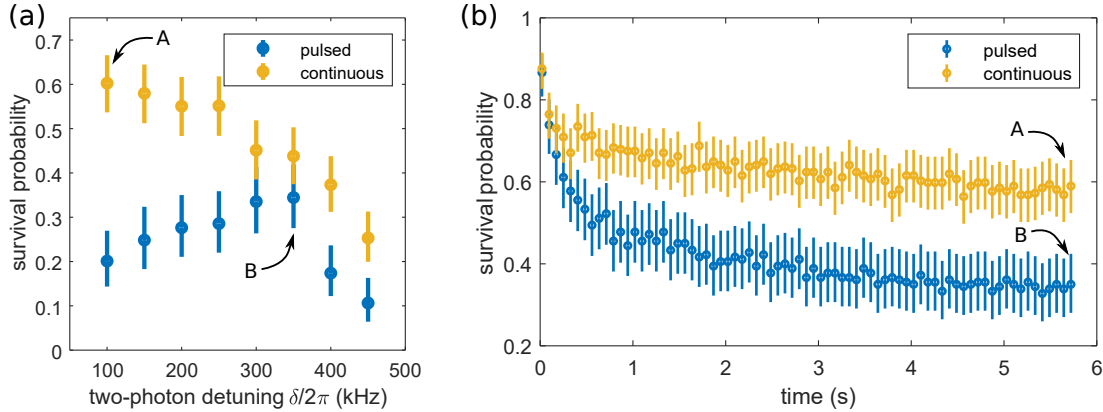


Figure 2.3: (a) Survival probability after 5.8 s using pulsed and continuous Raman sideband cooling. For continuous cooling the peak position is shifted away from the cooling sideband transition at 350 kHz, because of repumper-induced differential light shifts. (b) Survival probability as function of time for pulsed and continuous Raman sideband cooling. The points marked with A (B) are the same in both plots.

A comparison of pulsed and continuous Raman sideband cooling is shown in Fig. 2.3(a). For this measurement we load a single atom into the resonator and use the cavity-based atom detection to probe the presence of an atom after fixed cooling duration. We then obtain the probability that an atom “survives” the probing duration and plot the survival probability as function of two-photon detuning. One can see that in case of pRSC the survival probability peaks at a two-photon detuning of about 350 kHz with respect to the carrier which corresponds to a two-photon detuning that equals the trap frequency ($\delta \approx \nu$). However, in case of cRSC the survival seems to favour a lower two-photon detuning. This shift is attributed to a differential light shift induced by the repumper beam that shift the frequency of the carrier and sideband transitions. Note that for this measurement the pulsed Raman cooling was not fully optimized. The shift of the peak position is nonetheless clearly visible. The survival as function of time is shown in Fig. 2.3(b). By measuring the survival as function of probing duration we are able to fit the data with an exponential function and extract the lifetime. After optimization of continuous Raman sideband cooling we obtain lifetimes of up to 55 s which are believed to be vacuum-limited [61].

2.3 Light Shifts Induced by the Near-Resonant Optical Pumping Beams

This section describes a systematic characterization of differential light shifts that occur during continuous Raman sideband cooling. As already mentioned cRSC has a smaller parameter space that needs to be explored in order to find the optimum cooling condition than pRSC. In case of continuous cooling there is no need to choose a Raman pulse duration τ_R which is difficult to optimize for three-dimensional cooling. We therefore implement continuous Raman sideband cooling which requires precise knowledge of the induced differential light shifts.

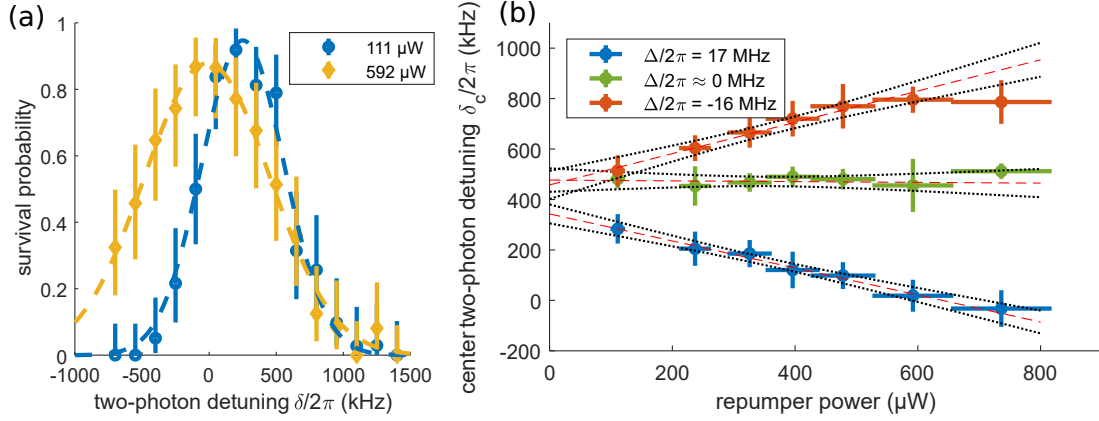


Figure 2.4: (a) The survival probability is shown as function of two-photon detuning δ for two different powers of the repumper beam. Because of differential light shifts the center two-photon detuning δ_c that maximizes the survival probability depends on the power of the repumper beam. (b) The center two-photon detuning is shown as function of the power of the repumper beam for three different repumper detunings. See the main text for a detailed discussion.

2.3.1 Detecting the Light Shifted Sideband Frequency

For the characterization of differential light shifts we investigate the dependence of the survival probability on the two-photon detuning and repumper power and detuning. The survival probability is measured after 500 ms of continuous Raman sideband cooling. In order to keep the experimental sequence reasonable short we alternately cool the atom for 1 ms and subsequently wait for 24 ms in order to allow for heating effects to take place. That way the atom is heated out of the trap if the cooling is not efficient enough. We measure the survival probability as function of the two-photon detuning δ and extract from a Gaussian fit the center two-photon detuning δ_c which maximizes the survival (see Fig. 2.4(a)). Repeating the measurement for several repumper powers reveals that the center two-photon detuning δ_c depends on the repumper power. We identify the center two-photon detuning δ_c as the light shifted sideband frequency and extract the light shift δ_{LS} according to Eq. (2.3).

$$\delta_c = \nu + \delta_{\text{LS}} \quad (2.3)$$

The center two-photon detuning δ_c is shown in Fig. 2.4(b) as function of the repumper power for three different repumper detunings. The linear slope clearly shows that the differential light shift δ_{LS} is proportional to the repumper power P as it is well known for dipole potentials [44].

$$\delta_{\text{LS}} \propto -\frac{1}{\Delta} \cdot P \quad (2.4)$$

In addition it can be seen in Fig. 2.4(b) that the sign of the differential light shift depends on the sign of the repumper detuning with vanishing light shift on resonance¹. We want to find the optimum combination of two-photon detuning, repumper detuning and repumper power and hence introduce a model to explain the measurements.

¹ Note that the atom is trapped in an optical dipole trap and thus the atomic transition frequency is shifted. The detuning presented in the label of Fig. 2.4(b) is taken with respect to the light shifted resonance frequency. For a detailed discussion see Sec. 2.3.3.

2.3.2 Model for Continuous Raman Sideband Cooling

Before we proceed with the systematic experimental characterization we present the model used to fit the measurement. We model our system following Ref. [59] and show the relevant atomic levels in Fig. 2.5(a). Here the Raman cooling cycle starts in the state $|2, -2, n\rangle$ that describes an atom in the internal state $|F = 2, m_f = -2\rangle$ with n motional excitations. The Raman coupling at a Rabi frequency Ω and a two-photon detuning δ' transfers the atom into the state $|1, -1, n - 1\rangle$ and thereby reduces the number of motional excitations by one. Note that here the Raman two-photon detuning is denoted with δ' instead of δ , since we consider only the Raman cooling sideband and neglect carrier and heating transitions. For resonant addressing of the cooling sideband we thus consider $\delta' = 0$ which corresponds to $\delta = \nu$. In addition to the Raman coupling we consider optical repumping at a Rabi frequency ω via the excited state $|2', -2, n^* - 1\rangle$ with a repumper detuning Δ . The number of motional excitations of the excited state is here labelled with n^* , since this state experiences a different trapping potential than the ground-states. The excited state decays, either into the state $|1, -1, n - 1\rangle$ at a rate γ_1 or into the state $|2, -2, n - 1\rangle$ at a rate γ_2 . In the latter case the cooling cycle is completed and the atom was cooled from the n -manifold into the $(n - 1)$ -manifold. Following Ref. [59] we note that the cooling occurs through the scattering mediated via the excited state $|2', -2, n^* - 1\rangle$. The cooling rate is therefore proportional to the population of the excited state as long as the system does not reach the motional ground-state.

Assuming that the population in the motional ground-state is negligible we are interested in finding a steady-state solution of the excited state population ρ_{ee} . Note that under steady-state conditions the population in each n -manifold is constant and the decay into the manifold has to be equal to the decay rate out of the manifold [59]. This is the case when the decay $|2', -2, n^*\rangle \rightarrow |2, -2, n\rangle$ equals the decay $|2', -2, n^* - 1\rangle \rightarrow |2, -2, n - 1\rangle$ shown in Fig. 2.5(a). In this case we can regard the γ_2 -decay and obtain the closed three-level system shown in Fig. 2.5(b). The system dynamic is described via a Lindblad master equation shown in Eq. (2.5). The equation describes the time evolution of the atomic density matrix ρ under the combined action of coherent couplings (included via the Hamiltonian \hat{H}) and dissipative decay (included via the collapse operators \hat{C}_l) [62]. A solution of the excited state population is given by Eq. (2.6) which fulfils $\frac{\partial \rho_{ee}^{\text{st}}}{\partial t} = 0$ and thus describes a steady-state solution [59].

$$\dot{\rho} = \hat{\mathcal{L}}\rho = -\frac{i}{\hbar} [\hat{H}, \rho] + \sum_l \hat{C}_l \rho \hat{C}_l^\dagger - \frac{1}{2} \left(\hat{C}_l^\dagger \hat{C}_l \rho + \rho \hat{C}_l^\dagger \hat{C}_l \right) \quad (2.5)$$

$$\rho_{ee}^{\text{st}} = \frac{\omega^2 \Omega^2}{2\Omega^2 \left(\Gamma^2 + \Omega^2 + (1 - \alpha) \left(2\delta'^2 + \omega^2 \right) + 4\tilde{\delta}(\Delta - 2\alpha\delta') \right) + \alpha \left(4\Gamma^2 \delta'^2 + \left(\omega^2 + 4\delta' \tilde{\delta} \right)^2 \right)} \quad (2.6)$$

Here the relative detuning $\tilde{\delta} = \Delta - \delta'$ has been introduced together with the atomic linewidth $\Gamma = 2(\gamma_1 + \gamma_2)$ and the effective repumping efficiency $\alpha = \frac{\gamma_2}{\gamma_1 + \gamma_2}$. In the limit of $\Gamma \gg \omega \gg \Omega$ an approximate solution is given by Eq. (2.7) and shown in Fig. 2.5(c) as function of two-photon detuning and repumper detuning [59].

$$\rho_{ee}^{\text{st}} \approx \frac{\omega^2 \Omega^2}{2\Omega^2 \left(\Gamma^2 + 4\Delta^2 \right) + 4\alpha\delta'^2 \Gamma^2 + \alpha \left(\omega^2 + 4\delta' \tilde{\delta} \right)^2} \quad (2.7)$$

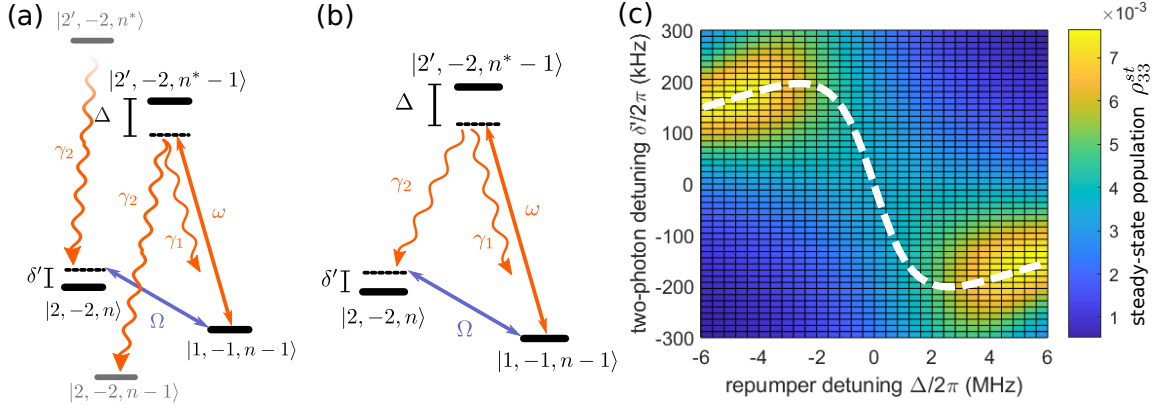


Figure 2.5: (a) Relevant states used to model the Raman cooling process. The Raman coupling with Rabi frequency Ω reduces the number of motional excitations and the optical repumper with Rabi frequency ω prepares the atom for another cooling cycle. See Sec. 2.3.2 for details. (b) Closed three-level system used to find a steady-state solution under Raman cooling conditions. (c) Steady-state excited state population under Raman cooling conditions as function of two-photon detuning δ' and repumper detuning Δ . The two-photon detuning that maximizes the excited state population is shown as dashed line.

In order to relate this three-level model to our measurements we claim that the survival probability is proportional to the cooling rate which is in turn proportional to the steady-state excited state population ρ_{ee}^{st} . We are thus interested in finding the two-photon detuning δ'_m that maximizes the excited state population and model the differential light shift as $\delta_{\text{LS}} = \delta'_m$. By imposing the condition $\frac{\partial \rho_{ee}^{\text{st}}}{\partial \delta'} = 0$ we find that δ'_m obeys Eq. (2.8). The two-photon detuning δ'_m derived from Eq. (2.8) is shown as white dashed line in Fig. 2.5(c). Note that the solution of Eq. (2.8) depends on the repumper Rabi frequency ω and the repumper detuning Δ and serves as model for fitting the differential light shift measurements.

$$0 = (\delta'_m)^3 - \frac{3}{2}\Delta (\delta'_m)^2 + \left[\frac{1}{2}\Delta^2 - \frac{1}{4}\omega^2 + \frac{1}{8}\Gamma^2 \right] \delta'_m + \frac{1}{8}\Delta\omega^2 \quad (2.8)$$

In order to gain some more intuitive physical insight we compare the results of the three-level model to a simpler two-level system that includes only the repumper coupling. To this end, we consider the ground-state $|1, -1\rangle$ that is coupled to the excited state $|2', -2\rangle$ with a repumper Rabi frequency ω and a detuning Δ as shown in Fig. 2.6(a). The system is described by the non-Hermitian Hamiltonian (2.9) where the $i\gamma$ term has been introduced in order to account for the finite linewidth of the optical transition [51, 63, 64]. The light shift for this two-level system is obtained by computing the eigenenergies E that are shown in Eq. (2.10).

$$H = \hbar \begin{pmatrix} \Delta - i\gamma & \omega \\ \omega & 0 \end{pmatrix} \quad (2.9)$$

$$E = \frac{\hbar}{2} \Re \left(\Delta - i\gamma \pm \sqrt{(2s-1)\gamma^2 + \Delta^2 - 2i\gamma\Delta} \right) \quad (2.10)$$

Here \Re takes the real part of the expression and $2\gamma = \Gamma \approx 2\pi \cdot 6$ MHz denotes the linewidth of the transition. Note that the repumper Rabi frequency ω is included via the saturation parameter $s = I/I_{\text{sat}}$

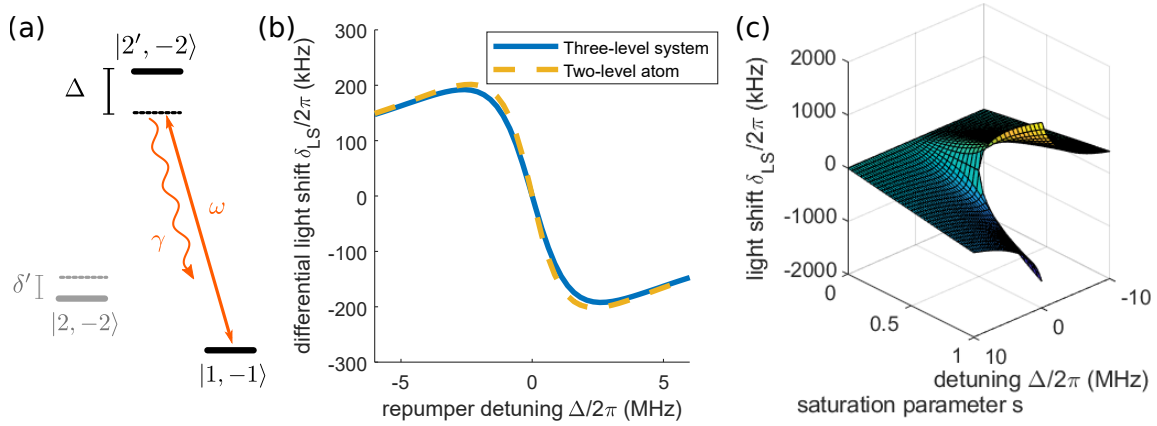


Figure 2.6: (a) Relevant level scheme of the simpler two-level model used to describe the light shift induced by the repumper beam. The repumper with Rabi frequency ω and detuning Δ couples the $|1, -1\rangle$ state to the excited state and thereby induces a light shift. (b) Comparison of the three-level model with the two-level model. For sufficiently low repumper intensities the predictions are quantitatively similar. (c) Light shift predicted by the two-level model as function of repumper saturation parameter s and detuning Δ . For intensities exceeding $s = 0.5$ the model becomes discontinuous on resonance.

which expresses the intensity I in units of the saturation intensity I_{sat} . Equation (2.11) shows the relation between Rabi frequency ω and saturation parameter [53].

$$s = 2 \left(\frac{\omega}{\Gamma} \right)^2 \quad (2.11)$$

A comparison of the three-level model with the simpler two-level model is shown in Fig. 2.6(b) for a saturation parameter of $s = 0.25$. Both models make quantitatively similar predictions for the differential light shift as long as the repumper intensity is sufficiently small. The light shift computed with the two-level model is shown in Fig. 2.6(c) as function of repumper saturation parameter s and repumper detuning Δ . Note that for intensities exceeding $s = 0.5$ the two-level model becomes discontinuous on resonance, due to an emerging Autler-Townes splitting [65, 66]. The three-level model however remains continuous even for higher intensities.

2.3.3 Systematic Characterization of Differential Light Shifts

In order to experimentally characterize the light shifts induced by the repumper beam we carry out a 3-dimensional parameter scan that spans 21 repumper detunings, 7 repumper powers and 15 Raman two-photon detunings and measure the survival probability for each point. Note that the repumper power is measured in free-space before coupling the light into the fiber of the lower cavity mirror. The D1-light is off-resonant with the cavity and thus only a small fraction leaks into the cavity. Since the physically relevant quantity is intensity instead of power we calibrate the intra-cavity intensity at the position of the atoms by measuring optical pumping rates. To this end, we load a single atom into the resonator and prepare it in the $F = 1$ hyperfine state. We then shine optical pumping light on the $F = 1 \rightarrow F' = 2$ (D1) transition with a fixed power for variable duration and subsequently perform a cavity-based state detection. The measurement is shown in Fig. 2.7(a) where the population $\rho_{F=2}$ of the $F = 2$ hyperfine state is shown as function of optical pumping duration. The fit is based on

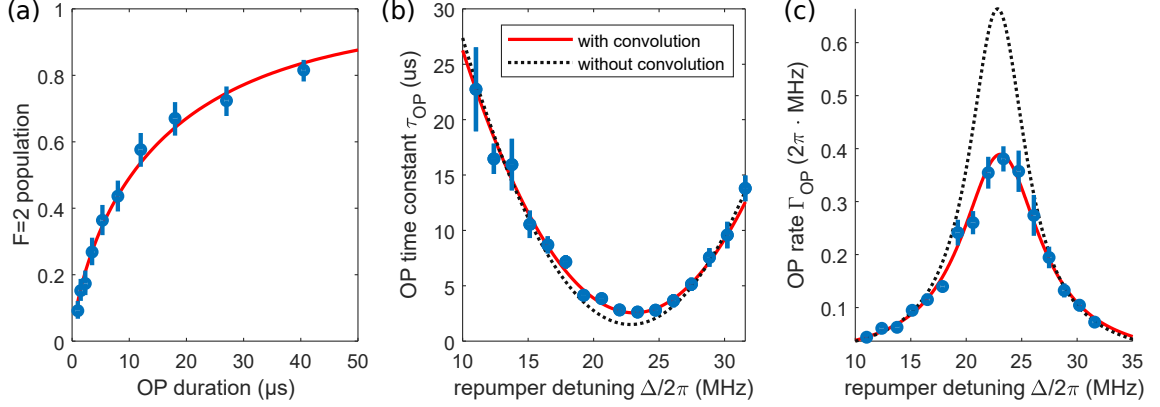


Figure 2.7: (a) Population of the $F = 2$ state as function of optical pumping (OP) duration. The fit is a stretched exponential as explained in the main text. (b) The OP time constant extracted from a stretched exponential fit is shown as function of the repumper detuning Δ . The black dotted line corresponds to a fit of Eq. (2.13). The solid red line takes fluctuations of the detuning into account and is based on Eq. (2.15). (c) The data from (b) is presented in terms of optical pumping rates $\Gamma_{\text{OP}} = \tau_{\text{OP}}^{-1}$. The deviation between the measurement and the fit (2.13) becomes more noticeable when the data is presented in terms of rates.

a stretched exponential following Eq. (2.12). Here the stretching factor β is introduced to account for inhomogeneous effects [51, 67]. We measure the optical pumping time constant τ_{OP} for various repumper detunings Δ and fixed repumper power.

$$\rho_{F=2} = 1 - \exp\left(- (t/\tau_{\text{OP}})^\beta\right) \quad (2.12)$$

The pumping rate $\Gamma_{\text{OP}} = \tau_{\text{OP}}^{-1} = \alpha \cdot \Gamma_{\text{scat}}$ is proportional to the scattering rate Γ_{scat} and the constant repumping efficiency $\alpha \approx 0.58$. Taking the expression for the scattering rate from Ref. [53] we obtain Eq. (2.13) that describes the OP time constant as function of repumper detuning Δ .

$$\tau_{\text{OP}}(\Delta) = \frac{2}{\alpha\Gamma} \frac{1 + 4(\Delta/\Gamma)^2 + s}{s} \quad (2.13)$$

A fit of Eq. (2.13) to the measurement is presented in Fig. 2.7(b). Here the optical pumping time constant τ_{OP} is shown as function of repumper detuning Δ . The fit of Eq. (2.13) deviates from the measurement in the vicinity of the resonance. This deviation becomes more noticeable when the same data is presented in terms of optical pumping rates $\Gamma_{\text{OP}} = \tau_{\text{OP}}^{-1}$. We attribute the deviation in the vicinity of the resonance to a fluctuation of the repumper frequency. The repumper frequency is referenced by means of polarization spectroscopy to a vapour cell which guarantees good long term stability [68]. However, due to the finite slope of the error signal we nonetheless observe frequency fluctuations of the order of a few MHz.

In order to take the fluctuation of the detuning into account we assume that the detuning follows a Gaussian probability density function (PDF) with a center detuning $\bar{\Delta}$ and a width σ_Δ . We thus compute a convolution of τ_{OP} in Eq. (2.13) with a Gaussian g_{PDF} shown in Eq. (2.14). The convolution is presented in Eq. (2.15).

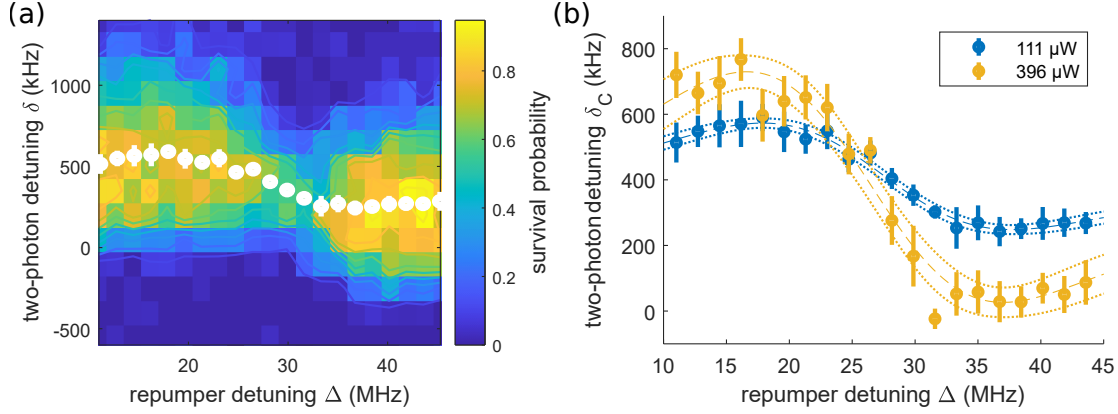


Figure 2.8: (a) Measurement of survival probability as function of two-photon detuning δ and repumper detuning Δ for a fixed repumper power of $P = 111 \mu\text{W}$. For each repumper detuning Δ we obtain the center two-photon detuning δ_c that maximizes the survival probability (white points). (b) Center two-photon detuning δ_c in dependence of the repumper detuning extracted from the 2D-scan shown in (a). It shows the expected dispersive shape when varying the repumper detuning across the resonance. Note that the amplitude of the dispersive shape increases with repumper power. The dashed lines are a fit based on the three-level model.

It turns out that the resulting expression is of the same form as Eq. (2.13) with an effective detuning $\Delta_{\text{eff}}^2 = \Delta^2 + \sigma_\Delta^2$.

$$g_{\text{PDF}}(\Delta, \bar{\Delta}, \sigma_\Delta) = \frac{1}{\sqrt{2\pi}\sigma_\Delta} \exp\left(-\frac{1}{2} \left(\frac{\Delta - \bar{\Delta}}{\sigma_\Delta}\right)^2\right) \quad (2.14)$$

$$\begin{aligned} \bar{\tau}_{\text{OP}}(\Delta) &= \int_{-\infty}^{\infty} g_{\text{PDF}}(\Delta', \Delta, \sigma_\Delta) \cdot \tau_{\text{OP}}(\Delta') d\Delta' \\ &= \frac{2}{\alpha\Gamma} \frac{1 + 4(\Delta_{\text{eff}}/\Gamma)^2 + s}{s} \end{aligned} \quad (2.15)$$

We fit expression (2.15) to the measurement with the Gaussian width σ_Δ as an additional free parameter. Plotting the measurement in terms of optical pumping rate reveals that Eq. (2.15) describes the data significantly better than Eq. (2.13). From the fit we extract $\sigma_\Delta = (3.0 \pm 0.5) \text{ MHz}$ and calibrate the intra-cavity repumper intensity as function of repumper power P . We can therefore express the intensity in terms of the saturation parameters $s = c_s \cdot P$ and obtain the proportionality constant $c_s = (7.7 \pm 0.7) \times 10^{-4} \mu\text{W}^{-1}$.

Fitting the Differential Light Shift Measurement

With the intra-cavity intensity calibration at hand we can now compare the measurement of differential light shifts to the previously introduced model. One subset of the dataset is shown in Fig. 2.8(a) for a fixed repumper power of $P = 111 \mu\text{W}$. For each scan of the two-photon detuning we obtain the center two-photon detuning δ_c that maximizes the survival probability and present it as function of repumper detuning Δ in Fig. 2.8(b). The same dispersive shape as predicted by the theoretical model emerges (Fig. 2.6(b)) when scanning the repumper detuning Δ across the resonance. In addition it can

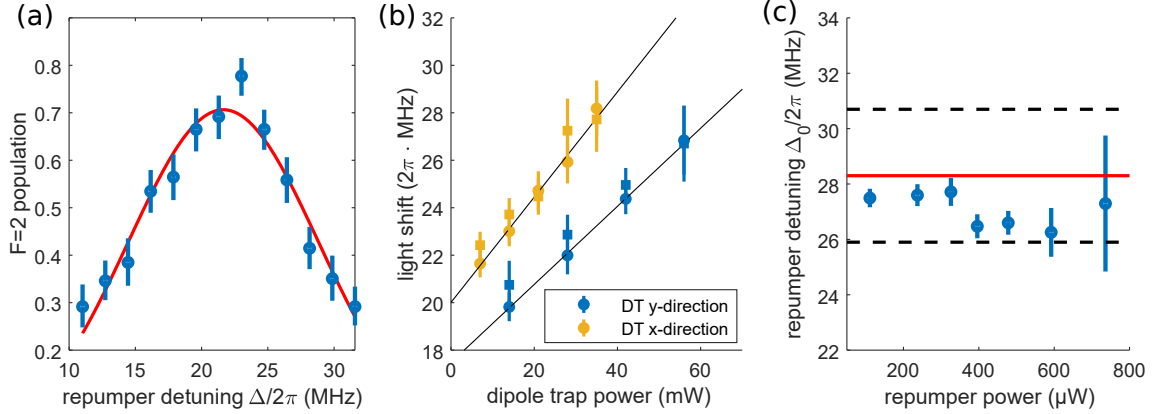


Figure 2.9: (a) The $F = 2$ population is shown as function of repumper detuning Δ with respect to the free-space transition for a fixed duration of optical pumping in order to characterize the light-shift induced by the dipole traps. The resonance frequency is extracted from a Gaussian fit. (b) The resonance frequency of the D1 $F = 1 \rightarrow F' = 2$ transition (circles) and the $F = 2 \rightarrow F' = 2$ transition (squares) is shown as function of dipole trap power for the x - and y -direction. The light shifted resonance is extracted by projecting the linear fit onto the point of operation. (c) The resonance frequency Δ_0 is shown that yields vanishing differential light shift for the different repumper powers. The independent characterization of the light shift induced by the dipole traps is shown in red with the 95 % confidence intervals shown as dashed lines.

be seen that the amplitude of the dispersive shape increases with repumper power. The dashed lines in Fig. 2.8(b) show a fit based on Eq. (2.3) where the differential light shift δ_{LS} is modelled via the three-level model. In order to fit the three-level model to the measured data we use 4 free parameters: the resonance frequency Δ_0 with respect to the free space transition, the intensity calibration factor c_s , the width σ_Δ of the Gaussian distribution for the detuning and a constant offset $\delta_{c,0}$ to the differential light shift which takes the role of the trap frequency ν in Eq. (2.3). The data is fitted as function of repumper detuning Δ for each repumper power separately. In order to evaluate the agreement between the theoretical three-level model and the measured data we analyze the fitting parameters as function of repumper power.

Note that the repumper detuning Δ is defined here with respect to the free-space transition as retrieved by the vapor cell reference. For the following discussion it is useful to distinguish the free-space detuning Δ from the detuning with respect to the light shifted transition Δ_d . The latter takes into account the dressing of the optical dipole traps which induces a light shift $\Delta_{\text{LS}} = \Delta - \Delta_d$. In the following we discuss the results obtained from the fitting.

The resonance frequency Δ_0 extracted from the fit of the differential light shift is shown in Fig. 2.9(c). It coincides with the light shifted transition frequency of the $F = 1 \rightarrow F' = 2$ D1 transition ($\Delta_0 \approx \Delta_{\text{LS}}$). For this comparison we characterized the light shift induced by the two red-detuned dipole traps running at 868 nm separately. To this end we perform spectroscopy by preparing the atoms in the lower $F = 1$ hyperfine state. We then shine an optical pumping pulse for fixed duration but variable detuning. The measurement is presented in Fig. 2.9(a) showing the population of the upper $F = 2$ hyperfine state as function of repumper detuning Δ . We repeat the measurement for multiple dipole trap powers and obtain for each power the resonance position from a Gaussian fit. The resonance frequency is shown in Fig. 2.9(b) as function of dipole trap power for the $F = 1 \rightarrow F' = 2$ and $F = 2 \rightarrow F' = 2$ transition of the D1-line. From a linear fit we obtain the light shift of the $F = 1 \rightarrow F' = 2$

2.3 Light Shifts Induced by the Near-Resonant Optical Pumping Beams

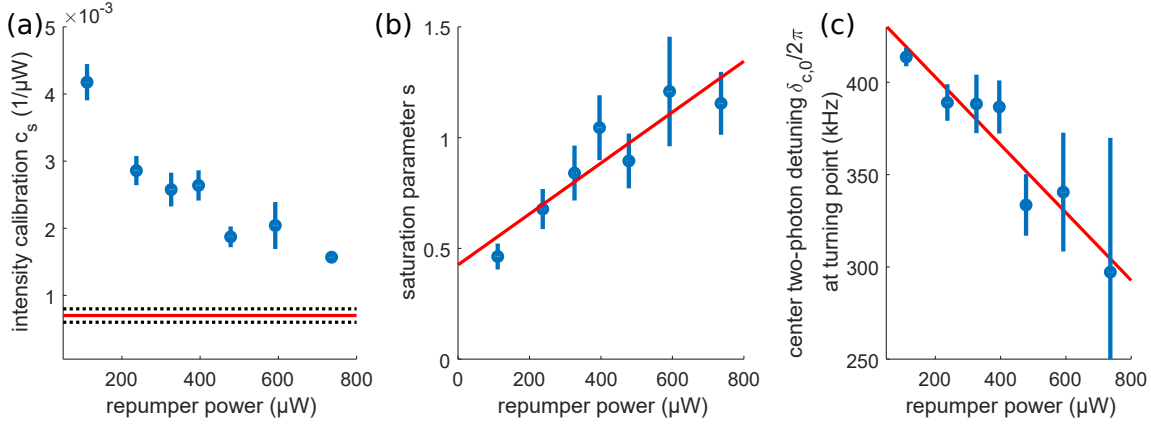


Figure 2.10: (a) The intensity calibration factor c_s extracted from the fit is shown as function of repumper power. The independent measurement of the intensity calibration factor is given in red with 95 % confidence bounds shown as dotted lines. (b) The fitted saturation parameter computed from the intensity calibration in (a) is shown. (c) The center two-photon detuning $\delta_{c,0}$ that maximizing the survival probability on resonance is shown. The interpretation of the residual slope is discussed in the main text.

transition of $(0.16 \pm 0.01) \text{ MHz mW}^{-1}$ and $(0.22 \pm 0.04) \text{ MHz mW}^{-1}$ for the dipole trap along the x - and y -direction, respectively. From this calibration we extract a light shift of $\Delta_{\text{LS}} = (28.4 \pm 2.5) \text{ MHz}$ at the point of operation which is shown as a red line (for reference) in Fig. 2.9(c).

In addition to the resonance frequency Δ_0 we extract the corresponding center two-photon detuning $\delta_{c,0}$ that maximizes the survival probability on resonance. In accordance with Eq. (2.3) we expect $\delta_{c,0} = \nu$ for $\Delta = \Delta_0$, i.e. on resonance with the light shifted transition ($\Delta_d = 0$). The extracted fitting parameter is shown in Fig. 2.10(c) and shows a systematic dependence on the repumper power instead of being constant. We consider an additional light shift induced by the polarizer beam on the $F = 2 \rightarrow F' = 2$ transition as a possible explanation. However, the lower hyperfine state $|F = 1, m_f = -1\rangle$ is about 6.8 GHz detuned, such that the light shift induced onto this state is negligible. The upper hyperfine state $|F = 2, m_f = -2\rangle$ is a dark state with respect to the polarizer beam assuming that the polarization is set to be σ^- . An additional light shift induced by an imperfection of the polarization can not explain the residual slope of $(-0.18 \pm 0.07) \text{ kHz } \mu\text{W}^{-1}$. The effect is only considerable for a very strong polarization imperfection that would spoil the optical pumping efficiency. We therefore conclude that an additional light shift can not be the (only) explanation for the systematic shift of the center two-photon detuning $\delta_{c,0}$ as function of repumper power.

The intensity calibration factor c_s extracted from each separate fit is shown in Fig. 2.10(a). Since non-linear absorption effects should not play a role we expect the intensity calibration factor c_s to be constant as function of repumper power. However, we observe a systematic dependence of c_s on the repumper power. Furthermore, we compute the corresponding saturation parameter $s = c_s \cdot P$ for each repumper power P and fit $s(P)$ with a polynomial of first order. Fig. 2.10(b) shows an offset of $s = 0.42 \pm 0.26$ for vanishing repumper power $P = 0$. This physically impossible result indicates that additional effects have to be taken into account that are not captured by the current model.

In Fig. 2.4(b) we present the differential light shift as function of repumper power P instead of repumper detuning Δ . Since the light shift depends linearly on the repumper power P we fit the measurement with a polynomial of first order. The extracted slope and offset for the various repumper

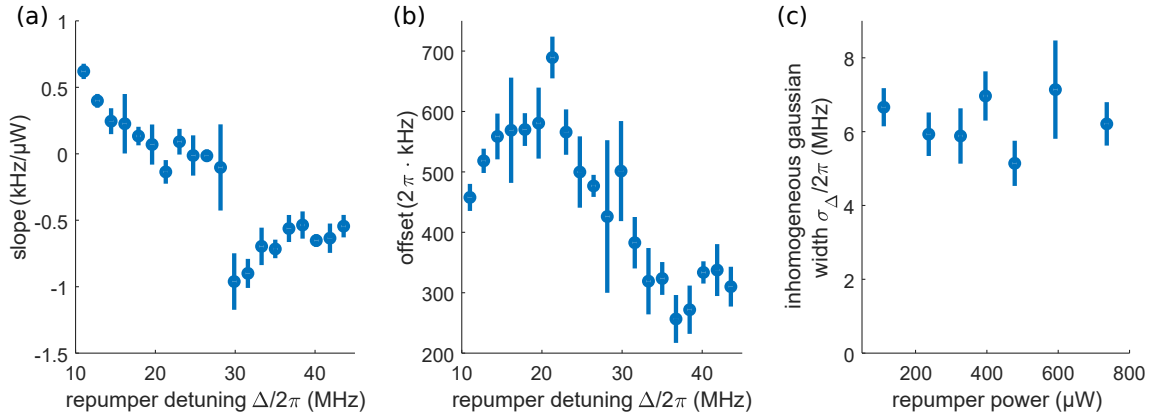


Figure 2.11: (a) The fitting parameter σ_Δ used for the convolution is shown as function of repumper power. (b+c) The differential light shift is fitted as function of repumper power (see Fig. 2.4(b)) for various repumper detunings separately. The slope (b) and the offset (c) of the fitted first order polynomial is shown as function of repumper detuning Δ . The slopes (b) are asymmetric for blue- and red-detunings.

detunings are shown in Fig. 2.11(a) and Fig. 2.11(b), respectively. For near-resonant blue repumper detunings the slopes reach values down to about $-1 \text{ kHz } \mu\text{W}^{-1}$. For similar red-detunings the slope is however consistent with zero and only for higher detunings of about 3Γ the slope reaches values up to $0.5 \text{ kHz } \mu\text{W}^{-1}$. Clearly the strength of the differential light shift is asymmetric with respect to the detuning. Note that the presented fitting model is strictly symmetric with respect to the simultaneous sign flip $\Delta \rightarrow -\Delta$ and $\delta_{\text{LS}} \rightarrow -\delta_{\text{LS}}$, and hence does not include any asymmetric effects. Fitting the symmetric model to the asymmetric data might explain the observed systematic shift of fitting parameters (see Fig. 2.10(a-c)). However, a detailed discussion of possible extensions is beyond the scope of this thesis.

To complete the discussion of extracted fitting parameters we obtain the Gaussian width σ_Δ used to describe an inhomogeneous distribution of detuning. The extracted fitting parameter is shown in Fig. 2.11(c) as function of repumper power with a mean value of about $\sigma_\Delta/2\pi \approx 6 \text{ MHz}$. This value deviates from the previously found value of $(3.0 \pm 0.5) \text{ MHz}$ used to calibrate the intra-cavity intensity. However, since the assumption of a Gaussian probability distribution was somewhat arbitrary we do not give a physical interpretation of the deviation and emphasize instead that the parameter is constant as function of repumper power.

2.3.4 Cooling Efficiency as Function of Repumper Detuning

The presented analysis in the previous sections describes the differential light shifts induced by the near-resonant repumper beam and is based on extracting the light shifted sideband frequency. In addition to the characterization of light shifts we are interested in identifying parameter regimes that are well suited for cooling. Fig. 2.12(a-c) show the survival probability as function of two-photon detuning δ and repumper detuning Δ for three different repumper powers. The survival probability drops when the repumper is tuned into resonance with the light-shifted optical transition at $\Delta/2\pi \approx 28 \text{ MHz}$. This drop in survival probability is explained by so called *dipole-force fluctuations* [31]. At a trapping wavelength of 868 nm the excited state experiences an anti-trapping potential which is even stronger

than the trapping potential of the ground state [69]. In order to understand the drop in survival probability for resonant illumination we model the optical pumping process with a simple two-level system following Ref. [34]. We consider the dressing of the bare states $|G, N\rangle$ and $|E, N-1\rangle$. Here $|G\rangle$ and $|E\rangle$ refer to the internal state of the two-level atom and $|N\rangle$ refers to the number of repumper photons being present. Following the notation of Ref. [34] the dressed states $|g, N\rangle$ and $|e, N\rangle$ are shown in Eq. (2.16).

$$\begin{aligned} |g, N\rangle &= \cos(\theta) |G, N\rangle - \sin(\theta) |E, N-1\rangle \\ |e, N\rangle &= \sin(\theta) |G, N\rangle + \cos(\theta) |E, N-1\rangle \end{aligned} \quad (2.16)$$

Here the mixing angle θ is defined by $\tan(2\theta) = -\omega/\Delta_d$ and depends on the repumper Rabi frequency ω and the repumper detuning Δ_d with respect to the light-shifted transition. Note that the dressed state $|g, N\rangle$ is ground-state like (for small θ) and experiences a trapping potential. In contrast the dressed state $|e, N\rangle$ experiences an anti-trapping potential. From Eq. (2.16) one obtains the spontaneous transition rates Γ_{ge} between dressed states $|g, N\rangle$ and $|e, N-1\rangle$ as $\Gamma_{ge} = \Gamma |\langle e, N-1|G, N-1\rangle|^2 |\langle E, N-1|g, N\rangle|^2$. The resulting transition rates between dressed states are shown in Eq. (2.17).

$$\begin{aligned} \Gamma_{ge} &= \Gamma \sin^4(\theta) \\ \Gamma_{gg} &= \Gamma_{ee} = \Gamma \sin^2(\theta) \cos^2(\theta) \\ \Gamma_{eg} &= \Gamma \cos^4(\theta) \end{aligned} \quad (2.17)$$

In the limit of large detunings $|\omega/\Delta_d| \ll 1$ we approximate $\cos^2(\theta) \approx 1$ and $\sin^2(\theta) \approx \epsilon = \omega^2/(4\Delta_d^2)$. Assuming that the atoms are initially prepared in the trapped state $|g, N\rangle$ the ratio of decay into an anti-trapping state versus the decay into a trapped state is given by $\Gamma_{ge}/\Gamma_{gg} \approx \epsilon$. For an atom being prepared in an anti-trapped state $|e, N\rangle$ the same consideration yields a decay ratio of $\Gamma_{ee}/\Gamma_{eg} \approx \epsilon$. This means that for $\epsilon \ll 1$ the atom predominantly decays into dressed states which experience a trapping potential [34]. The condition $\epsilon = \omega^2/(4\Delta_d^2) \ll 1$ motivates to use a detuning $|\Delta_d| > 0$ for the repumper beam. Note that on resonance ($\Delta_d = 0$) one obtains $\cos(\theta) = \sin(\theta) = \frac{1}{\sqrt{2}}$ and thus none of the dressed states is trapped since the anti-trapping potential of the excited state contributions is stronger than the trapping potential of the ground-state contribution.

In addition to the the drop in cooling efficiency for resonant repumping we observe an asymmetry with respect to the repumper detuning. This becomes apparent in Fig. 2.12(a-c) where the survival probability is shown as function of two-photon detuning δ and repumper detuning Δ for different repumper powers. While the survival probability reaches similar values for red- and blue-detunings at rather low repumper powers (Fig. 2.12(a)) it becomes asymmetric for higher repumper powers (Fig. 2.12(c)). In this case a higher survival probability is obtained for blue instead of red repumper detunings. Since both, the presented two-level model and the presented three-level model are symmetric with respect to the repumper detuning Δ it remains an open question if the asymmetry has a physical or a technical cause. An off-resonant coupling to an additional electronically excited state is an unlikely explanation, since the excited-state hyperfine splitting of the D1-line of ^{87}Rb exceeds 800 MHz and is thus much larger than the explored variation of the repumper detuning. On the technical side an inhomogeneous distribution of atom positions in the optical dipole trap would yield an inhomogeneous distribution of resonance conditions for the repumper beam. Such a distribution

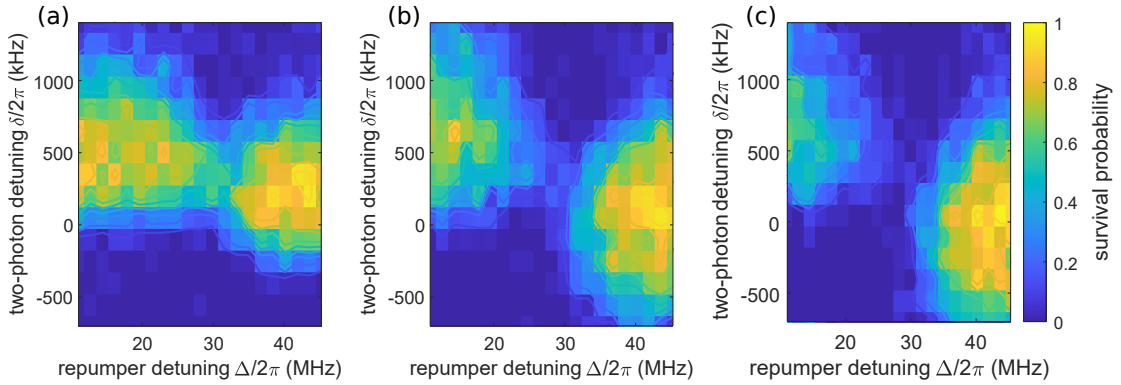


Figure 2.12: The survival probability is shown as function of two-photon detuning δ and repumper detuning Δ for a repumper power of (a) $111 \mu\text{W}$, (b) $396 \mu\text{W}$ and (c) $736 \mu\text{W}$. One can see that the survival probability drops when the repumper is tuned on resonance ($\Delta/2\pi \approx 28 \text{ MHz}$) with the light-shifted transition. The colorbar is the same for all three plots.

might have an asymmetric tail towards red detunings which would not occur for blue-detunings. However, a detailed modelling of inhomogeneous effects is beyond the scope of this thesis.

In conclusion, we optimize Raman sideband cooling in order to increase the data acquisition rate of future measurements. We obtain vacuum-limited lifetimes up to 55 s and confirm that near ground-state cooling is achieved. A precision measurement of repumper-induced differential light shifts is discussed. Precise knowledge of this effect is needed in order to simultaneously optimize the Raman two-photon detuning together with the repumper detuning and repumper power. We present a model of continuous Raman sideband cooling [59] that takes into account the coherent Raman and repumper couplings and dissipative decay and obtain qualitative agreement with the measurement. We observe that dipole-force fluctuations [31] induce heating when the repumper is tuned into resonance with the light shifted transition. It is therefore beneficial to detune the repumper beam away from resonance [34]. The precise characterization of differential light shifts is used to implement a feed-forward of the two-photon detuning. This simplifies the parameter space since the resonance with the cooling sideband is maintained when the repumper detuning or repumper power are varied. The following chapter describes the fluorescence imaging of atomic ensembles inside the resonator by means of Raman imaging. For the measurements presented therein the two-photon feed-forward is used in order to simplify the optimization.

Raman Imaging of Atoms in an Optical Cavity

In order to experimentally investigate effects associated to the collective coupling of multiple atoms to the same cavity mode we aim to prepare atomic ensembles inside the resonator. The optimization of this process is based on the ability to count the number of atoms inside the resonator. For our cavity parameters this counting can not be implemented by probing the cavity reflection, since a single atom is sufficient to induce a vacuum-Rabi splitting. We thus implement the counting of atoms by means of fluorescence imaging. The scattering of near-resonant imaging light inevitably induces heating of the atoms which has to be compensated by a cooling mechanism [31]. Fluorescence imaging of ^{87}Rb with molasses cooling is nowadays a standard technique [32, 70]. However, in our experiment we can not implement three-dimensional molasses cooling, due to the limited optical access where one direction is blocked by the cavity itself. A previous attempt to image the atoms during degenerate Raman sideband cooling [47] did not reach the signal necessary to count atoms, since they were lost before a sufficient number of photons could be detected. We therefore implement Raman imaging which is based on detecting the repumper fluorescence during continuous Raman sideband cooling.

Raman imaging is frequently used in the context of quantum gas microscopy, in particular for the imaging of fermionic ^{40}K and ^6Li species [34, 71, 72] and allows for exposure times exceeding 1 s [33]. We detect the fluorescence of the repumper and polarizer beams that are (near-)resonant with the D1 transition of ^{87}Rb and are coupled off-resonantly to the cavity via the lower cavity mirror (see Fig. 3.1(a)). Using off-resonant D1 light instead of resonant D2 light is beneficial, because of the Purcell-effect which channels resonant light predominantly into the cavity mode. This effects makes an optical cavity an efficient light-matter interface, but at the same time hinders efficient fluorescence imaging. To overcome this detrimental effect we therefore use light off-resonant with respect to the cavity for the fluorescence imaging. This chapter starts by introducing the improved imaging setup. A spatial filter was set up in order to suppress scattered light originating from spurious reflections at the upper cavity mirror. Furthermore, the optimization of the imaging parameters is described. The influence of the repumper detuning onto the achievable signal-to-noise ratio is described and a preliminary analysis of individual atom pictures is presented. Moreover, the influence of the motional ground-state is discussed, which is dark with respect to the Raman transfer and the optical pumping beams and thus does not generate fluorescence.

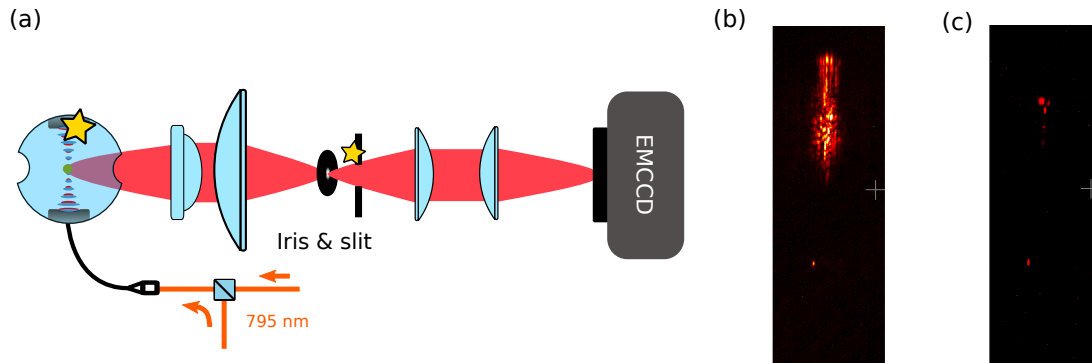


Figure 3.1: (a) The new imaging setup is sketched. The repumper light is injected through the lower cavity mirror and off-resonantly coupled into the cavity. In order to remove spuriously scattered light reflected from the upper cavity mirror, a slit is used to spatially filter the unwanted reflection without blocking most of the atomic fluorescence. This filter exploits that the spurious scattering focusses at a different axial position than the light originating from the atoms. (b) Image taken without the newly installed spatial filter showing the spurious scattering. (c) Image taken after installing the spatial filter. The spurious scattering is suppressed significantly. The residual light originates from the lock laser light at 770 nm and can be filtered out with a narrowband frequency filter.

3.1 New Imaging System

The atomic fluorescence is collected by the in-vacuum ($NA=0.5$) lens and imaged onto an electron multiplying charged coupled device (EMCCD) camera [73]. Since the fluorescence rate of Raman imaging is rather low [74] a long exposure time of the order of a second is typically needed [34]. We observed that for an exposure times of 1 s a very strong background is accumulated in the image (see Fig. 3.1(b)). This background originates from spurious reflections at the upper cavity mirror and prevented long exposure times without saturating the camera. It furthermore limited the possible amplification of the signal by the EMCCD camera and thereby prohibited the imaging of atoms. In order to suppress the spurious light we installed an improved imaging setup that spatially filters out the unwanted reflection. The new imaging setup is shown in Fig. 3.1(a) and includes an intermediate imaging plane where we use an iris and a slit to spatially block the light originating from the upper cavity mirror. The implementation of the spatial filter exploits that the light of the atoms focusses 8 mm before the unwanted reflection. By installing a slit at the focal plane of the spurious light we block it without significantly reducing the amount of detected atomic fluorescence. Fig. 3.1(c) shows that the spurious reflection is blocked by partially closing the slit. The intermediate image plane is relayed onto the EMCCD camera with a one-to-one telescope. Achromatic air-spaced doublet lenses are used in the new imaging system in order to suppress aberrations. The optics of the new imaging setup are mounted in tubes in order to suppress stray light. The axial position of the lenses can be adjusted with rotating adjustable lens mounts. This allows to optimize the focussing while looking at atom pictures. In addition to the spatial filtering we employ narrow frequency band-pass filters used to suppress any light other than the fluorescence light at 795 nm.

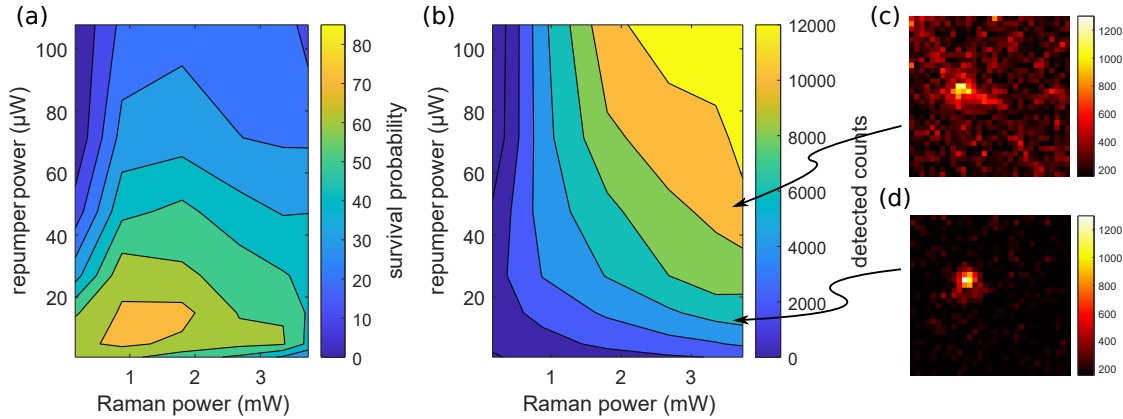


Figure 3.2: The survival probability (a) measured with the cavity-based atom detection and the fluorescence detected with the EMCCD camera (b) are shown for a parameter scan of repumper power and Raman power. (c+d) Two selected pictures are shown corresponding to two different repumper powers. For a repumper power of $48 \mu\text{W}$ (c) the atom does not gain brightness in comparison to (d) which was taken for a repumper power of $15 \mu\text{W}$. Instead the background increases which limits the signal-to-noise ratio.

3.2 Optimizing the Raman Imaging

For the optimization of the fluorescence we detect the scattered repumper photons in a region of interest (ROI) of $12 \mu\text{m} \times 12 \mu\text{m}$. The number of integrated fluorescence counts is computed after subtraction of a corresponding background image. In addition, we detect the presence of an atom before and after each picture by probing the cavity reflection as explained in Sec. 1.2. We average only over images for which the atom survived the 1 s exposure. This post-selection enables an independent characterization of survival probability and fluorescence. For the measurements presented here the Raman two-photon detuning δ is chosen to maximize the cooling efficiency based on the detailed characterization presented in chapter 2. A feed-forward is used to maintain the resonance with the Raman cooling transition when varying other parameters such as repumper power or detuning.

In order to characterize the fluorescence we vary the repumper power and the Raman power. The measured survival probability and EMCCD counts for a repumper detuning of $\Delta_d = 0$ with respect to the light shifted D1 transition are shown in Fig. 3.2(a) and Fig. 3.2(b), respectively. The measurement of fluorescence shows that higher powers yield more fluorescence. However, increasing the fluorescence comes at a price of significantly reducing the survival probability. For a resonant repumper ($\Delta_d = 0$) the survival probability does not exceed 70% and is rather sensitive with respect to variations of repumper power or Raman power. This behaviour is expected for a resonant repumper from the discussion in Sec. 2.3.4 and confirms that it is beneficial to detune the optical pumping beams away from resonance.

By visually inspecting individual images we observe that we are able to image single atoms by means of Raman imaging. Two examples are shown in Fig. 3.2(c,d) for a Raman power of about 3.7 mW and two different repumper powers. In both cases one can see a single atom well localized in the 3D lattice. However, the brightness of the atom does not increase for higher repumper power. Instead the brightness of the background increases which originates from residual unwanted scattering that is not blocked by the spatial filtering system. To confirm that the main source of background is

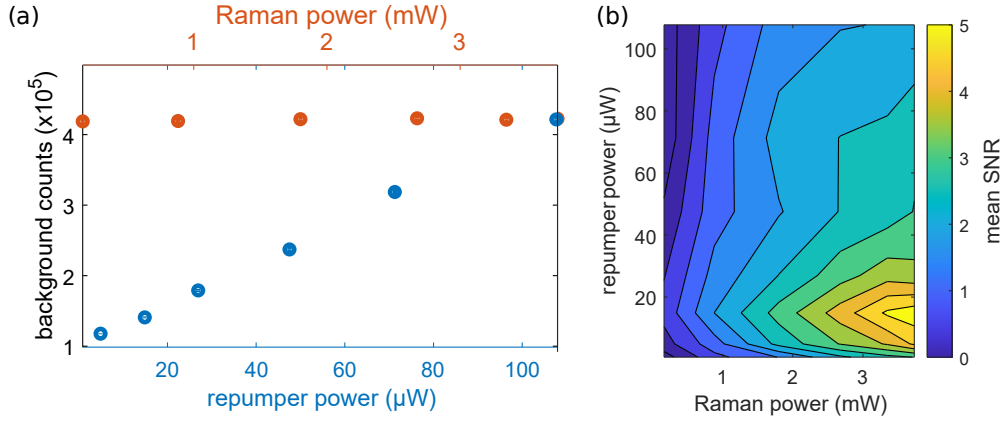


Figure 3.3: (a) Detected counts in background images (i.e. without an atom being present) as function of repumper power and Raman power. The background light originates from the D1 beam. Residual scattering of the Raman beam is suppressed by narrowband frequency filtering. (b) The SNR as defined by Eq. (3.1) is shown corresponding to the fluorescence measurement shown in Fig. 3.2(b). The SNR serves as figure of merit for the optimization of the imaging in addition to the survival probability.

given by the D1 light we integrate the ROI of background images where no atom is present. As shown in Fig. 3.3(a) the number of detected background counts depends linearly on the repumper power and is independent of the Raman power. This increase of the background entails an increase of the image noise that reduces the fluorescence signal-to-noise ratio. Consequently, as a figure of merit for the optimization of the imaging we use the mean signal-to-noise ratio in order to account for the detrimental effect of spurious background.

3.2.1 Optimization of the Signal-to-Noise Ratio

In order to optimize the physical parameters for imaging we use the signal-to-noise ratio (SNR) as figure of merit in addition to the survival probability. For each parameter set we take multiple images and use the cavity-based atom detection to post-select those where the atom survived the exposure time. We compute the mean integrated fluorescence of the region of interest μ_{Fluo} averaged over the post-selected pictures and subtract the corresponding average of background images μ_{BG} , i.e. where no atom is present. The mean background-subtracted fluorescence is then compared to the standard deviation of the background counts σ_{BG} to yield the SNR as defined by Eq. (3.1).

$$SNR = \frac{\mu_{\text{Fluo}} - \mu_{\text{BG}}}{\sigma_{\text{BG}}} \quad (3.1)$$

The SNR corresponding to the measurement presented in Fig. 3.2(b) is shown in Fig. 3.3(b). The maximum is reached for rather low repumper powers in comparison to the maximum of fluorescence shown in Fig. 3.2(b). Note that the atomic fluorescence starts to saturate for a given repumper power while the amount of background light increases linearly with repumper power. Thus the SNR is expected to exhibit a distinct optimum as function of repumper power.

The survival probability corresponding to the maximal SNR reaches only about 40%. Moreover, in the parameter regime of best survival the SNR reaches only values of about unity. The presented

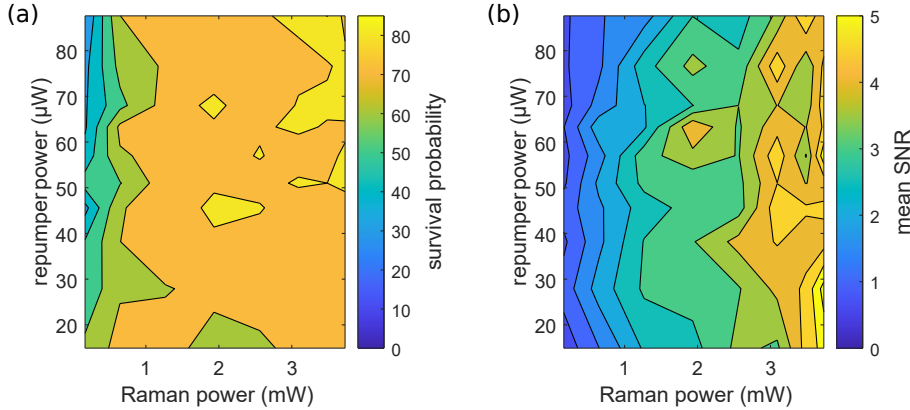


Figure 3.4: Survival probability (a) and mean signal-to-noise ratio (b) as function of Raman power and repumper power for a repumper detuning of $\Delta \approx \Gamma$. The survival probability exceeds 80 % and is rather insensitive with respect to variations of the powers.

parameter regime with resonant repumper is therefore not well suited to image small atomic ensembles. Since we would like to count atoms based on the detected fluorescence we have to avoid atom loss during imaging. The case of loss of atoms during the imaging would correspond to an effective non-integer atom number and would therefore wash out fluorescence histograms.

3.2.2 Resonant versus Off-Resonant Repumping

As explained in Sec. 2.3.4 the survival probability is enhanced when the repumper is tuned away from resonance. We therefore repeat the characterization of the signal-to-noise ratio as function of repumper and Raman power for a small repumper detuning of $\Delta_d \approx 1 \Gamma$ with respect to the light-shifted D1 transition. We obtain the survival probability and mean SNR shown in Fig. 3.4(a) and Fig. 3.4(b), respectively. The survival probability exceeds 80 % and in addition becomes insensitive with respect to variations of repumper or Raman power. Moreover, we observe that for suitable parameter choices a survival probability of 80 % can be combined with a mean SNR of about 4.5. From this measurement it becomes clear that the repumper detuning is an important parameter for the implementation of non-destructive imaging with good signal-to-noise ratio. We therefore proceed to study the influence of the repumper detuning on the survival probability and signal-to-noise ratio.

In order to find a repumper detuning which combines good signal-to-noise ratio and high survival probability we experimentally vary the repumper detuning. Since this affects the scattering rate we also vary the repumper power in order to compensate the reduction of scattering rate for the detuned case. The obtained survival probability and the mean SNR are shown in Fig. 3.5(a) and Fig. 3.5(b), respectively. We observe that the survival probability is reduced for a repumper detuning $\Delta_d = \Delta - \Delta_{LS} \approx 0$ in the vicinity of the light shifted resonance at $\Delta_{LS}/2\pi \approx 28$ MHz, as expected from the discussion in Sec. 2.3.4. Slices of the survival probability as function of repumper detuning are shown in Fig. 3.5(f) for three repumper powers. Note that the drop in survival probability on resonance becomes more severe for increased repumper power. In addition, it seems that the center of the dip shifts as function of repumper power. However, by comparison with Fig. 3.5(a) it can be seen that for increasing repumper power the dip extends more towards red-detunings without any

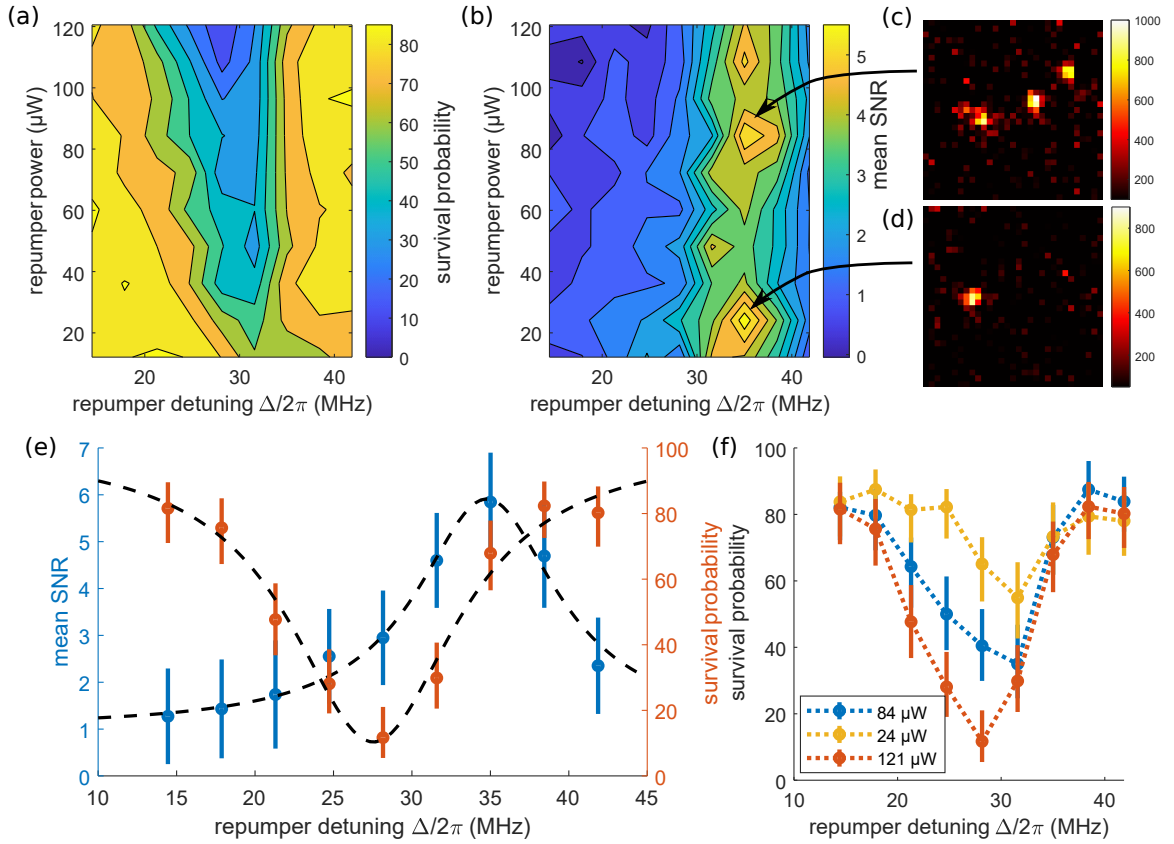


Figure 3.5: Survival probability (a) and mean signal-to-noise ratio (b) as function of repumper detuning and repumper power. On resonance the survival probability is reduced significantly. The signal-to-noise ratio shows an asymmetry and seems to favour blue-detuning of the order of the transition linewidth. (c,d) Two specific background-subtracted images taken during the measurement. (e) Signal-to-noise ratio (SNR) and survival probability as function of repumper detuning. The SNR shown here corresponds to the maximum SNR achievable for the given repumper detuning Δ . The trace of the survival probability corresponds to a fixed repumper power of 121 μW and reaches its minimal value on resonance with the light-shifted D1 transition. In contrast the SNR is highest for a detuning of (34.8 ± 0.9) MHz which corresponds to a blue detuning of about 1 Γ with respect to the light-shifted transition. The fits have a Lorentzian shape and serve as guide to the eye. (f) The survival probability is shown as function of repumper detuning for three different powers. The survival probability drops on resonance with the light-shifted transition.

broadening towards blue detunings. This effect might be caused by an inhomogeneous distribution of atoms in the optical dipole trap which has a Gaussian envelope. Atoms outside the center region experience a weaker light shift and therefore the resonance of the light-shifted transition would occur at smaller repumper detunings Δ with respect to the free-space transition.

In addition we also find that the highest SNR of about 6 is reached for a repumper detuning of $\Delta/2\pi = (34.8 \pm 0.9)$ MHz with respect to the free-space transition which corresponds to a detuning of about $\Delta_d \approx 1 \Gamma$ with respect to the light-shifted transition. Interestingly no enhancement of the SNR is observed for a corresponding red detuning. This asymmetry is visualized in Fig. 3.5(e) showing the maximum SNR obtained for a given repumper detuning. Note that the model for continuous Raman

sideband cooling (cRSC) presented in Sec. 2.3.2 is symmetric with respect to the repumper detuning as long as the differential light shifts are taken into account. In particular the model is symmetric for a detuning $\pm\Delta_d$ with respect to the light-shifted transition and the corresponding two-photon detuning $\delta = \nu \pm \delta_{LS}$. Indeed we observe that cooling can be efficiently implemented for red and blue repumper detunings while the mean SNR is enhanced only for blue detunings. For the measurement presented in Fig. 3.5 we used a feed-forward of the two-photon detuning δ and hence maintained the two-photon resonance with the cooling sideband for all settings. The asymmetry of the signal-to-noise ratio is therefore not caused by differential light shifts. We are currently working on more advanced models of cRSC that take into account the existence of the dark state and include the harmonic ladder explicitly. In addition we consider technical explanations such as effects associated to the polarizer beam. However, so far a comprehensive explanation of the observed behaviour remains elusive.

3.3 Towards Counting of Atoms

In order to exploit the collective coupling of multiple atoms to the resonator mode we would like to carry out experiments with well known atom number. Therefore, we would like to count the atoms inside the resonator mode based on the fluorescence images taken via Raman imaging. In some cases we are able to identify individual atoms that are spatially separated, as shown in Fig. 3.5(c). However, this technique works only if the atoms are located in sufficiently separated lattice sites. A short calculation reveals that we do not expect to resolve individual lattice sites separated by $\frac{\lambda_{DT}}{2}$. For our dipole trap wavelength of $\lambda_{DT} = 868$ nm this corresponds to a lattice spacing of about 434 nm which is far below the diffraction limited resolution given by the Rayleigh limit d_R shown in Eq. (3.2) [75, 76].

$$d_R = 0.61 \frac{\lambda_{Fluo}}{NA} \quad (3.2)$$

For a fluorescence wavelength of $\lambda_{Fluo} = 795$ nm and a numerical aperture of $NA = 0.5$ this corresponds to a limit of $d_R = 970$ nm. Thus we do not resolve individual lattice sites and have to rely on the integrated fluorescence in order to count atoms. Note that this estimation assumes that the numerical aperture is limited by the first in-vacuum lens and that further reductions caused by e.g. the iris or the slit are negligible.

In order to characterize the new imaging system we are interested in finding its point-spread-function (PSF) which describes how an idealized point-source is imaged by an optical system. A detailed analysis of the PSF provides insight into aberrations of the imaging system and the achieved resolution [77]. In order to find the PSF we identify individual atoms that are well localized on a clean background [78]. We then fit the atomic fluorescence with a two-dimensional gaussian and align multiple images to a common center given by the peak position of the gaussian fit. In order to align several images with sub-pixel resolution we perform zero-padding in Fourier space. To this end, we compute the two-dimensional fourier transform of the image and extend the spectrum towards higher frequencies by appending zeros. Afterwards the inverse fourier transform yields an upsampled image. The PSF is then found by averaging over the aligned pictures. We calibrate the magnification of our imaging system taking two consecutive images and displacing the atom in between by a well known distance. The cross-correlation of the two images – before and after displacement – reveals the shift detected with the camera and corresponds to the distance over which the atoms got transported [79]. Using the optical conveyor belt we are able to accurately displace individual atoms and calibrate the

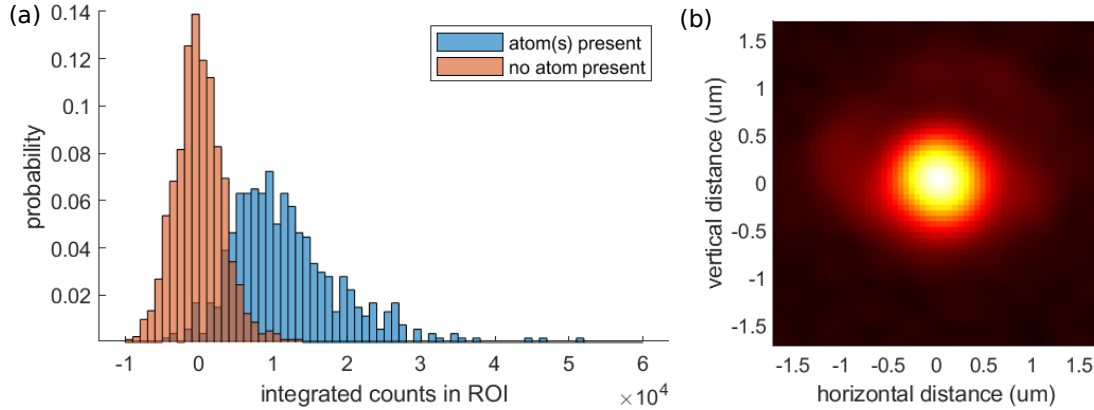


Figure 3.6: (a) Histogram of detected counts inside a region of interest (ROI) after background subtraction. The histogram of background-counts centered at zero overlaps with the histogram of counts with at least one atom present. The datasets corresponding to the two histograms are post-selected via the cavity-based atom detection. (b) By superimposing 50 images of individual atoms we obtain a preliminary point-spread-function (PSF). The PSF shown here is upsampled by a factor 7 following the technique described in the main text.

images to a dimension of $0.4 \mu\text{m pixel}^{-1}$. That way we obtain the preliminary point-spread-function shown in Fig. 3.6(b). The PSF has a Gaussian full width at half maximum of about $0.9 \mu\text{m}$ which confirms that the lattice spacing lies below the resolution limit of our imaging system. In the following we present an outlook regarding the next steps needed to optimize the imaging in order to count atoms by means of Raman imaging.

Fluorescence Histograms

Since we do not spatially resolve neighbouring lattice sites of the 868 nm dipole trap we want to count atoms by the amount of detected fluorescence. We thus integrate a region of interest and compute histograms of counts for multiple images after subtracting the mean background. A histogram is presented in Fig. 3.6(a) showing the distribution of counts for images without and with an atom being present. Here, we use the cavity-based atom detection to independently probe the presence or absence atoms. The histogram of background counts (where no atom was present) is centered at zero, since we subtract the mean number of background counts. The histogram of detected fluorescence with a mean of about 1.2×10^4 counts is taking only images into account where the atom survived the exposure time of 1 s. Note that the overlap between both histograms is considerable which limits the atom counting fidelity based on fluorescence detection. This makes evident the need to find ways to further increase the fluorescence emitted by atoms without increasing the background.

Since we induce the fluorescence by means of Raman cooling we simultaneously reduce the number of motional excitations until the atom is cooled to its motional ground-state. The motional ground-state is dark with respect to the Raman cooling transition and also dark with respect to the repumper and polarizer beam. Thus atoms in the motional ground-state do not yield fluorescence which hinders the fluorescence-based atom counting. We verified my means of Raman spectroscopy that near ground-state cooling is achieved. The Raman spectrum presented in Fig. 2.2(a) shows that the depth of the cooling sideband is reduced compared to the heating sideband, which indicates that a considerable fraction of the atoms is cooled to the 3D motional ground-state [58]. In order to investigate the effect

of the motional ground-state we envisage to apply a weak parametric excitation by modulating the intensity of the optical dipole trap at twice the trapping frequency [74]. That way atoms are expected to be lifted out of the motional ground-state and yield more fluorescence.

Photon Generation in an Atom-Cavity System

This chapter gives an introduction to the theoretical description of photon storage and retrieval in an atom-cavity system. In a typical Λ -scheme of an atom-cavity system, two atomic ground states are coupled via the cavity interaction and an additional control laser in Raman resonance [28, 80]. Single photons are generated into the cavity mode via a stimulated Raman adiabatic passage [81]. Control over the temporal wavefunction is given by tailoring the corresponding control laser pulse [36]. The derivation of the required control laser pulse is presented in the adiabatic regime for a sufficiently long temporal width of the single photon wavefunction. Beyond the adiabatic regime analytic solutions are not available and we compute the photon generation fidelity and photon storage efficiency numerically.

One important concern for photon generation in a cavity is the phase of the generated photon. The time-dependent control laser pulse induces a dynamical light shift onto the atomic states which in turn imprints a phase-chirp onto the generated photon [40]. The compensation of this chirp requires a phase-modulation of the control laser pulse. As an alternative to active phase modulation we present passive chirp compensation based on a bichromatic driving field. In this case, the suppression of phase chirps is based on mutual cancellation of the light shift induced by two optical frequency components. In order to find an analytic solution of the photon generation process, the equations of motion are typically solved by means of adiabatic elimination of the excited states. However, the standard method of carrying out the adiabatic elimination – which is commonly used in the literature [36, 40] – fails to provide a solution under two-tone driving conditions. Two alternative methods are presented based on an effective operator formalism [82] and based on an adiabatic approximation technique [42].

Extending the commonly considered Λ -system, we study photon generation in a more complex Tripod-system [29] that includes two degenerate cavity modes with orthogonal polarization. This level choice is considered for entanglement distribution in quantum networks [83]. The entanglement distribution rate is proportional to the Bell state projection probability [27] which depends on the branching ratio of the photon emission into the two polarization modes. For a Tripod system with a single excited state the branching ratio depends on the relative dipole transition strength and is thus fixed. We found that the off-resonant coupling to additional electronically excited states can be used to tune the branching ratio by adapting the single-photon detuning.

Note that the nomenclature used in this chapter is independent of definitions made in previous chapters, such that variables and definitions used here are consistent only within this chapter and the appendices A and B.

4.1 Photon Generation in the Adiabatic Regime

This section contains an introduction to adiabatic photon generation in an atom-cavity system. The atom is described as a Λ -system as shown in Fig. 4.1(a) where one transition is coupled by the cavity and the other transition is driven by a classical light field with time-dependent Rabi frequency $\Omega(t)$ [84]. Such a system can be described with the Hamiltonian in Eq. (4.1).

$$H = \omega_e |e\rangle \langle e| + \omega_c a^\dagger a + [g a |g_2\rangle \langle e| + H.c.] + \frac{1}{2} [\Omega(t) e^{-i\omega_l t} |e\rangle \langle g_1| + H.c.] \quad (4.1)$$

Here, a is the annihilation operator of the intra-cavity field, g denotes the atom-cavity coupling strength, ω_l denotes the angular laser frequency and ω_e and ω_c denote the energy of the excited state and intra-cavity field, respectively. Note that we set $\hbar = 1$ throughout this chapter. Assuming that the atom is initially prepared in the state $|g_1\rangle$, the number of excitations in the system is limited to 1 and the Hilbert space can be truncated accordingly [36]. In this case a general state of the Hilbert space $\mathcal{H} = \mathcal{H}_{\text{atom}} \otimes \mathcal{H}_{\text{cavity}}$ is given by a superposition of three possible contributions as shown in Eq. (4.2).

$$|\Psi\rangle = S(t) |g_1, 0\rangle + P(t) |e, 0\rangle + \mathcal{E}(t) |g_2, 1\rangle \quad (4.2)$$

Here $|i, n\rangle = |i\rangle \otimes |n\rangle$ denotes a state with the atom being in $i = g_1, g_2, e$ and $n = 0, 1$ photons in the cavity mode. A cavity-assisted stimulated Raman adiabatic passage (STIRAP) transfers the system from its initial state $|g_1, 0\rangle$ into the final state $|g_2, 1\rangle$ mediated via the excited state $|e, 0\rangle$ [35]. Thereby a photon with temporal envelope $\mathcal{E}(t)$ is generated in the cavity mode. The evolution of the state $|\Psi\rangle$ under the combined action of the Hamiltonian as well as dissipative processes can be described by a set of coupled ordinary linear differential equations [36]. The differential equations for the probability amplitudes S , P and \mathcal{E} are readily found by considering the Schrödinger equation $i\partial_t |\Psi\rangle = H |\Psi\rangle$ for the non-Hermitian Hamiltonian [85] shown in Eq. (4.3) written in a frame co-rotating with the laser frequency ω_l .

$$H = (\Delta - i\gamma) |e\rangle \langle e| + (\delta - i\kappa) a^\dagger a + [g a |g_2\rangle \langle e| + H.c.] + \frac{1}{2} [\Omega(t) |e\rangle \langle g_1| + H.c.] \quad (4.3)$$

Here Δ denotes the single-photon detuning of the control laser beam with respect to the atomic transition and δ denotes the two-photon detuning of the cavity with respect to the control laser frequency. In addition, we have introduced complex energies in order to account for decay of the excited states [63]. Here 2γ denotes the atomic linewidth and 2κ denotes the linewidth of the cavity.

According to prominent theoretical work (Ref. [36–38, 40]) one obtains a maximal photon generation efficiency of $\frac{2C}{2C+1}$ for an atomic Λ -system. Any desired temporal shape can be obtained as long as the dynamics are adiabatic. A sufficient condition for adiabaticity is given by $T_c C \gamma \gg 1$ with the cooperativity $C = \frac{g^2}{2\kappa\gamma}$ and the characteristic time T_c of the generated photon given by Eq. (4.4) [36, 39].

$$T_c = \sqrt{\langle t \rangle^2 + \langle t^2 \rangle} \quad (4.4)$$

$$\langle t^x \rangle = \int_{-\infty}^{+\infty} t^x |e(t)|^2 dt \quad (4.5)$$

If imperfections of the cavity mirrors are taken into account the photon retrieval efficiency becomes

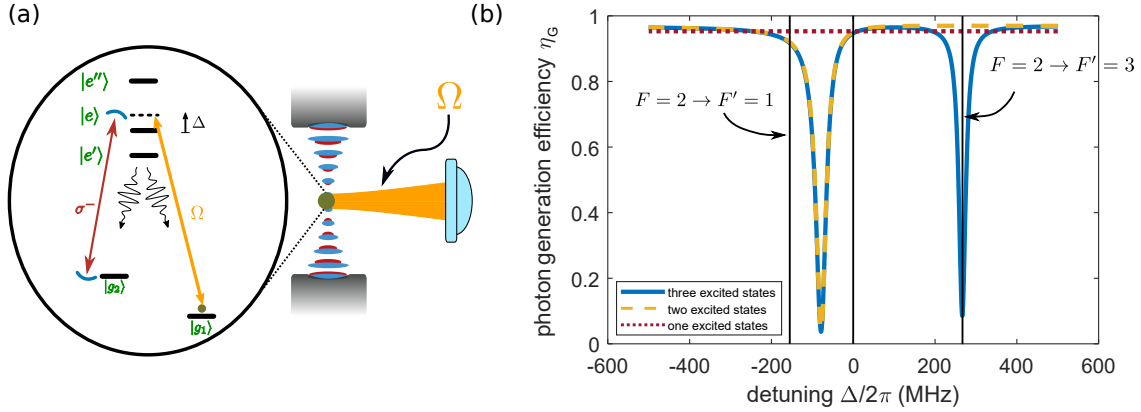


Figure 4.1: (a) Atomic level structure used to model cavity-based photon generation. The atom is initially prepared in the state $|g_1\rangle$ which is coupled to the excited state $|e\rangle$ with time-dependent Rabi frequency $\Omega(t)$. The atom-cavity coupling at strength g enables the generation of single photons inside the mode of the resonator. The off-resonant couplings to additional excited states ($|e'\rangle$ and $|e''\rangle$) modifies the photon generation efficiency. (b) The photon generation efficiency is shown as function of detuning Δ with respect to the $F = 2 \rightarrow F' = 2$ (D2) transition in ^{87}Rb . Because of the off-resonant coupling to multiple excited states the efficiency depends on the detuning. Here we show the efficiency taking only one excited state ($|e\rangle$), two excited states ($|e, e'\rangle$) and all three excited states ($|e, e', e''\rangle$) into account.

$\eta_R = \frac{\kappa_c}{\kappa} \frac{2C}{2C+1}$ with $\kappa = \kappa_c + \kappa_l$ [39]. Here κ_c denotes the rate at which photons leak out of the cavity into the transmission line and κ_l accounts for parasitic losses due to e.g. scattering at the cavity mirrors. Note that we distinguish between the photon generation efficiency η_G that describes the efficiency to generate a photon inside the cavity mode and the retrieval efficiency $\eta_R = \eta_G \cdot \eta_{\text{esc}}$. The latter takes the out-coupling of the photon into consideration and accounts for parasitic losses by multiplying the generation efficiency η_G with the escape efficiency $\eta_{\text{esc}} = \frac{\kappa_c}{\kappa_c + \kappa_l}$. For the calculations presented in this chapter we assume the CQED parameters $(g, \kappa_c, \kappa_l, \gamma)/2\pi = (50.2, 16, 25, 3)$ MHz of our experiment [29]. This corresponds to a cooperativity $C = 10.2$ and yields an optimum photon generation efficiency $\eta_R = 91\%$ and an escape efficiency of $\eta_{\text{esc}} = 39\%$.

Most of the available literature describes the atom as a three level Λ -system [36–39]. Ref. [40] presents a model that includes the off-resonant coupling to additional excited states. This extension renders the detuning Δ an important parameter, since a destructive interference occurs for certain choices of the parameters. The derivation of the maximally achievable photon retrieval efficiency η_R is presented in appendix A and includes (off-)resonant couplings to three excited states. The result is shown in Eq. (4.6).

$$\eta_G = \frac{|L|^2}{2\Re(K)} \quad (4.6)$$

Here L and K are constants that depend only on the level choice, CQED parameters and the detuning Δ . For a three-level Λ -system with one electronic excited state this expression reduces to the well known limit of $2C/(2C+1)$ that is also obtained in Ref. [36]. In this case the efficiency to generate a photon inside the cavity mode becomes independent of the detuning as shown in Fig. 4.1(b). However, if the off-resonant coupling to additional excited states ($|e'\rangle, |e''\rangle$) in Fig. 4.1(a) is taken into account,

the generation efficiency depends on the single-photon detuning Δ . It is shown in Fig. 4.1(b) that a destructive interference occurs when the cavity resonance is tuned between the $F = 2 \rightarrow F' = 1$ and $F = 2 \rightarrow F' = 2$ transition. Furthermore, if the upper excited state $|e''\rangle$ is taken into consideration, the generation efficiency drops when the cavity becomes resonant with the $F = 2 \rightarrow F' = 3$ transition. The $F' = 3$ excited state does not couple to the initial ($F = 1$) state and therefore does not mediate the STIRAP process. This result shows that the single-photon detuning Δ is an important parameter for cavity-based photon generation. The multi-level character of existing quantum emitters constrains the parameter choice for efficient photon generation. Quantitative knowledge of the effect is needed in order to guarantee efficient light-matter interaction.

Control laser pulse

In order to generate single photons with well controlled temporal wavefunction the control laser pulse with time-dependent Rabi frequency $\Omega(t)$ has to be chosen accordingly. In the adiabatic regime for sufficiently long and smooth photon pulses an analytic solution can be computed that yields a desired temporal wavefunction $e(t)$. The derivation of the corresponding control laser pulse $\Omega_M(t)$ introduced by Morin et. al. is presented in appendix A and shown in Eq. (4.7).

$$\Omega_M(t) = \frac{e(t)}{\sqrt{2\Re(K) \int_t^\infty |e(t')|^2 dt'}} \exp\left(-i \frac{\Im(K)}{2\Re(K)} \ln\left(\int_t^\infty |e(t')|^2 dt'\right)\right) \quad (4.7)$$

It can be seen that the magnitude as well as the phase of the control laser has to be modulated. The amplitude term in Eq. (4.7) determines the shape of the generated photon. In addition, the phase modulation is required to compensate time-dependent light shifts induced by the control pulse itself. Without compensation of this effect the generated photon would experience a phase-chirp that reduces the fidelity with the desired temporal wavefunction [40]. In Sec. 4.3 we present an alternative technique for compensating phase-chirps based on a bichromatic driving field. The limits of (near-)adiabatic photon generation for the CQED parameters of our experiment are discussed in Sec. 4.2.

4.2 High-Bandwidth Photon Generation beyond the Adiabatic Regime

In this section we analyze photon generation beyond the adiabatic regime described in Sec. 4.1. Using the control laser pulse $\Omega_M(t)$ shown in Eq. (4.7) we compute the photon generation fidelity F as function of the pulse duration. Note that here we are interested in the generation fidelity F rather than the efficiency, since we want to quantify the overlap of the generated wavefunction $\mathcal{E}_{\text{out}}(t)$ with the desired wavefunction $e(t)$. The fidelity is thus defined by a standard quantum mechanical overlap integral in Eq. (4.8).

$$F = \int_{-\infty}^{+\infty} \mathcal{E}_{\text{out}}(t) e^*(t) dt \quad (4.8)$$

In order to detect variations from the ideal adiabatic photon generation, the equations of motion (see appendix A) are solved numerically for 4 different pulse shapes. We proceed by presenting the required quantities for numerical calculations. This includes the pulse shape $e(t)$ which follows the normalization condition $\int_{-\infty}^{+\infty} |e(t)|^2 dt = 1$ and the pulse integral $I[e](t)$ as shown in Eq. (4.9). It is

4.2 High-Bandwidth Photon Generation beyond the Adiabatic Regime

	pulse shape $e(t)$	integral $I[e](t)$
secant hyperbolic	$\frac{1}{\sqrt{T}} \operatorname{sech}(2\frac{t-t_0}{T})$	$\frac{1}{2} - \frac{1}{2} \tanh(2\frac{t-t_0}{T})$
sin-squared	$\sqrt{\frac{8}{3T}} \sin(\pi \frac{t-t_0+T/2}{T})^2$	$\frac{1}{2} - \frac{t-t_0}{T} - \frac{2}{3\pi} \sin\left(\frac{2\pi(t-t_0)}{T}\right) - \frac{1}{12\pi} \sin\left(\frac{4\pi(t-t_0)}{T}\right)$
gaussian	$\frac{1}{\sqrt{\sqrt{2}\pi T}} e^{-\frac{(t-t_0)^2}{2T}}$	$\frac{1}{2} - \frac{1}{2} \operatorname{erf}\left(\frac{t-t_0}{\sqrt{2T}}\right)$
exponential	$\frac{1}{\sqrt{T}} e^{-\frac{ t-t_0 }{T}}$	$\frac{1}{2} - \operatorname{sign}(t-t_0) \frac{1}{2} \left(1 - e^{-2\frac{ t-t_0 }{T}}\right)$
	characteristic time T_c	truncated integral ζ
secant hyperbolic	$\frac{\pi}{4\sqrt{3}} T \approx 0.4535 T$	$\tanh(T_c/T)$
sin-squared	$\sqrt{\frac{1}{24} \left(2 - \frac{15}{\pi^2}\right)} T \approx 0.1414 T$	$\frac{T_c}{T} + \frac{8}{6\pi} \sin(\pi T_c/T) + \frac{1}{6\pi} \sin(2\pi T_c/T)$
gaussian	T	$\operatorname{erf}\left(\frac{T_c}{2\sqrt{2}T}\right)$
exponential	$\frac{1}{\sqrt{2}} T \approx 0.7071 T$	$1 - e^{-\frac{T_c}{T}}$

Table 4.1: Overview over different normalized pulse shapes and their properties. All pulses are time symmetric and centered at time t_0 . A plot of the expressions for the integral ζ can be found in Fig. 4.2(b).

beneficial to express the pulse integral $I[e](t)$ analytically in order to minimize numerical errors, since it is used to compute the time-dependent control laser pulse.

$$I[e](t) = \int_t^{+\infty} |e(t')|^2 dt' \quad (4.9)$$

In addition, to the photon pulses it is important to define a common time scale that enables a comparison of different pulse shapes. Note that the parameter T used in the definition of the pulse shapes in Tab. 4.1 does not define a common time-scale as we will see by considering a truncated integral of the photon pulse shapes. For a time-symmetric pulse centered at time t_0 the corresponding truncated integral is defined via Eq. (4.10).

$$\int_{t_0 - \frac{T_c}{2}}^{t_0 + \frac{T_c}{2}} |e(t)|^2 dt = \zeta \quad (4.10)$$

Here, we consider the integral of the photon pulse shape over a duration T_c that covers a fraction ζ of the normalized pulse shape. A comparison of the integral for the different pulse shapes is presented in Fig. 4.2(a) using the parameter T to define the truncation window ($T_c = T$). The parameter T is not a good measure of pulse duration, because the corresponding truncated integral differs considerably for the four pulse shapes. In Fig. 4.2(b) the truncated integral is computed using the characteristic

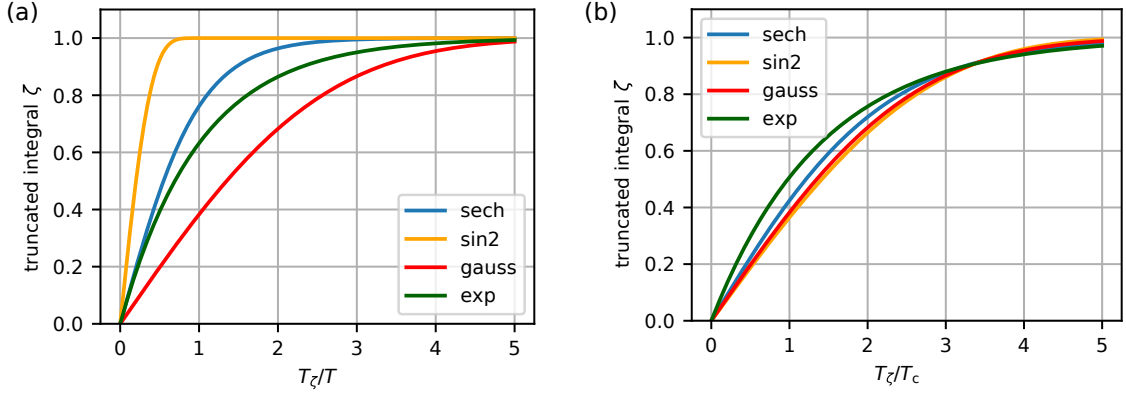


Figure 4.2: (a) Truncated integral as function of pulse duration parameter T for the four pulse shapes. The truncated integrals defined in Eq. (4.10) differs considerably which means that the parameter T is not well suited to define a common time-scale for different pulse shapes. (b) Truncated integral as function of the characteristic time T_c . The curves (for different pulse shapes) overlap and hence the parameter T_c is a reasonable measure of duration that enables a comparison of different pulse shapes.

time ($T_\zeta = T_c$) defined in Eq. (4.4). The time-scale T_c is a reasonable measure of pulse duration, since it yields a similar integral ζ for the considered pulse shapes. However, with the expressions for the truncated integral in Tab. 4.1, we are able to adapt the time scale parameter T such that the truncated integral takes the exactly same value for each pulse shape. We proceed by comparing the photon generation fidelity of different pulse shapes as function of the pulse duration.

Computing the generation fidelity as function of pulse duration

For benchmarking the different pulse shapes listed in Tab. 4.1, we compute the photon generation fidelity as function of pulse duration. We define the pulse duration by T_ζ for $\zeta = 0.99$ and use the expressions shown in Tab. 4.1 in order to compute the parameter T for each pulse shape. We then solve the system dynamics numerically for the control laser pulse in Eq. (4.7) and compute the fidelity as defined by Eq. (4.8). The result is presented in Fig. 4.3(a) showing the photon generation fidelity F as function of pulse duration T_ζ . For rather long durations $T_\zeta = 100$ ns (Fig. 4.3(c)) the pulses are centered at $t_0 = 0$. For shorter pulse durations a delay occurs with respect to the desired pulse shape (Fig. 4.3(d)) until the pulse shaping fails for even shorter pulses than $T_\zeta \approx 20$ ns. The latter corresponds to characteristic pulse times of about $T_c \approx 4$ ns (see Fig. 4.2(b)) which approaches timescales of the order of the inverse cavity linewidth $T_c \approx \kappa^{-1} = 3.9$ ns. In this regime the spectral extend of the photon pulse approaches the linewidth of the cavity such that the cavity starts to act as a frequency filter which is the ultimate limit for cavity-assisted photon generation.

The numerical analysis of the system dynamics shown in Fig. 4.3 confirms that for pulse durations $T_c \approx 1/(C\gamma)$ the adiabatic control pulse is insufficient. The comparison of four different pulse shapes shows that none of them yields significantly higher fidelities towards short ($T_c \approx 1/(C\gamma)$) pulse durations. Instead we observe for all pulses a rather sharp drop in fidelity (and generation efficiency) that occurs for $T_\zeta < 20$ ns which corresponds to $T_c C \gamma \lesssim 0.77$. This constitutes the limit of efficient light-matter interaction for our system.

In order to generate single photons with desired temporal envelope the control laser pulse with

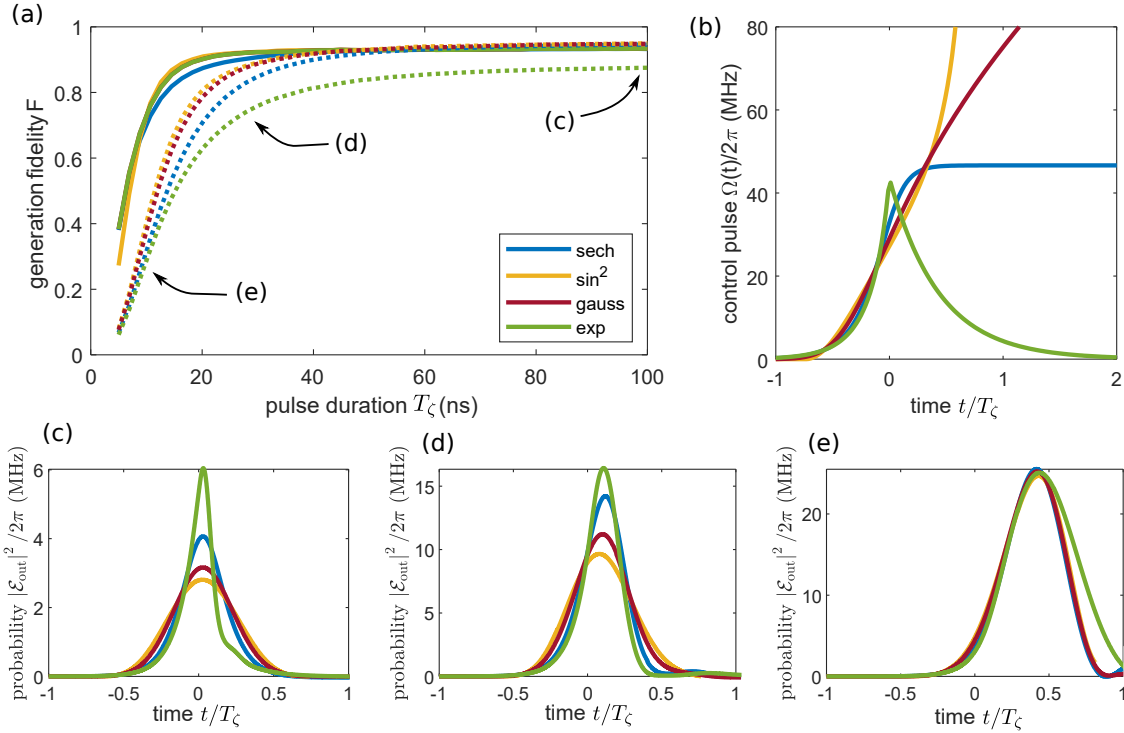


Figure 4.3: (a) Retrieval fidelity as function of pulse duration T_ζ . The dotted line shows the fidelity with respect to the desired shape and without taking any delay into account. The solid line takes the delay into account. Thereby, the fidelity can be enhanced in the regime of short pulses at $T_\zeta \approx 20$ ns (b) Time-dependent control pulse Rabi frequency $\Omega(t)$ for different pulse shapes. Note that the pulse strength diverges for a sin-squared shaped pulse, since the pulse has compact support. (c-e) Generated photon shapes for $T_\zeta = 100$ ns (c), $T_\zeta = 30$ ns (d) and $T_\zeta = 10$ ns (e).

time-dependent Rabi frequency $\Omega(t)$ has to be chosen according to Eq. (4.7). The time-dependent modulation shown in Fig. 4.3(b) induces a dynamical light shift onto the atomic levels which can give rise to phase-chirps of the generated photon. We proceed with the discussion of methods for the compensation of these phase-chirps.

4.3 Chirp Compensation with Polychromatic Driving Fields

The control laser pulse $\Omega_M(t)$ presented in Eq. (4.7) includes an active phase-modulation of the optical light field expressed by the complex exponential term. This phase modulation is required in order to compensate time-dependent light shifts induced by the control laser beam itself. Without active phase modulation a phase-chirp is imprinted onto the temporal wavefunction [40] that can be measured by means of homodyne detection [86].

In this section, an alternative method is presented based on a bichromatic control laser field having two optical frequency components called *master beam* and *support beam*. The compensation of the induced light shift is based on tuning the relative power and detuning such that the optical frequency components mutually cancel each others light shift. To this end, we introduce the time-dependent

Rabi frequency of the bichromatic driving fields. The effect of the second frequency component with relative detuning χ and relative electric field strength ξ is given by the *two-tone replacement* for the control laser Rabi frequency

$$\Omega(t) \rightarrow \Omega(t) \left[1 + \xi e^{-i\chi t} \right] \quad (4.11)$$

This replacement describes the effective Rabi frequency of the bichromatic driving field in the co-rotating frame of the master beam. The exponential term in Eq. (4.11) accounts for the relative detuning χ of the support beam with respect to the master beam [87, 88]. We are interested in finding a modified expression for the photon generation efficiency. However, reproducing the derivation presented in appendix A yields an invalid result. The result is independent of the newly introduced parameters χ and ξ , because it implicitly neglects the time-dependence of the control laser field. While this is a reasonable approximation for sufficiently smooth pulses, it fails to describe two-tone driving, since the Rabi frequency $\Omega(t)$ is accompanied by the exponential term which describes a rapidly rotating phase. Neglecting the time-dependence is therefore problematic, because even if the control pulse envelope varies sufficiently slowly the phase rotation might be considerable [42, 89]. Solving the system dynamics for single-tone and two-tone driving fields is achieved using a more sophisticated *adiabatic approximation* technique.

4.3.1 Adiabatic Approximation

In this section we use the methods of adiabatic approximation, presented in Ref. [42], for photon retrieval in an atom-cavity system. This requires considering the Schrödinger equation $i\partial_t |\Psi\rangle = H |\Psi\rangle$ with state vector $|\Psi\rangle = (\psi, \varepsilon)^T$. Here, ψ denotes the components of the ground-state Hilbert space and ε denotes the components of the excited state Hilbert subspace. We express the Hamiltonian into terms of submatrices that describe the evolution inside the ground state subspace (ω), the excited state subspace (Δ) and the coupling between the subspaces (Ω), as shown in Eq. (4.12). The goal is to find an effective Hamiltonian that describe the time-evolution of the ground states (ψ) upon adiabatic elimination of the excited states (ε).

$$H = \begin{pmatrix} \omega & \frac{1}{2}\Omega \\ \frac{1}{2}\Omega^\dagger & \Delta \end{pmatrix} \quad (4.12)$$

With this definition the Schrödinger equation can be written for the two subspaces separately.

$$i\partial_t \psi(t) = \omega \psi(t) + \frac{1}{2}\Omega \varepsilon(t) \quad (4.13)$$

$$i\partial_t \varepsilon(t) = \frac{1}{2}\Omega^\dagger \psi(t) + \Delta \varepsilon(t) \quad (4.14)$$

An equation for the evolution of the ground state subspace is obtained by formally integrating Eq. (4.14) and inserting the result into Eq. (4.13). Thereby, the excited Hilbert subspace is eliminated from the equations of motion and one obtains the integro-differential equation:

$$i\partial_t \psi(t) = \omega \psi(t) - \frac{i}{4}\Omega \int_0^t dt' e^{-i\Delta(t-t')} \Omega^\dagger \psi(t') \quad (4.15)$$

This remaining equation can be solved analytically for suitable approximations of the integral. Note that Eq. (4.15) is equivalent to the Schrödinger equation with the full Hamiltonian. So far we have only rewritten a first order differential equation (the Schrödinger equation) for two variables (ψ and ε) into a second order differential equation for one variable (ψ). The adiabatic elimination is carried out by approximating the integral.

Following Ref. [42] the easiest approximation is given by the *zero-th order Markov approximation* which sets $\psi(t') \approx \psi(t)$. Thereby, the integral in Eq. (4.15) can be solved and one obtains a first order differential equation describing the evolution of the ground state subspace. We neglect the time-dependence of the control laser Rabi frequency envelope under the approximation that it varies sufficiently slowly [36]. In order to derive a result for two-tone driving we instead treat the time-dependence originating from the two-tone replacement explicitly when approximating the integral in Eq. (4.15). The approximation is shown in Eq. (4.16), where we have used again the zero-th order Markov approximation in the first step.

$$\begin{aligned}
 i\partial_t\psi &= \omega\psi - \frac{i}{4}\Omega \left[1 + \xi e^{+i\chi t} \right] \int_{t_0}^t dt' e^{-i\Delta(t-t')} \left[1 + \xi e^{-i\chi t'} \right] \Omega^\dagger \psi(t') \\
 &\approx \omega\psi - \frac{i}{4}\Omega \left[1 + \xi e^{+i\chi t} \right] \left[\frac{1 - e^{-i\Delta t}}{i\Delta} + \xi \frac{e^{-i\chi t} - e^{-i\Delta t}}{i(\Delta - \chi)} \right] \Omega^\dagger \psi(t) \\
 &= \omega\psi - \frac{1}{4}\Omega \left[\frac{1 - e^{-i\Delta t}}{\Delta} + \xi \frac{e^{-i\chi t} - e^{-i\Delta t}}{(\Delta - \chi)} + \xi \frac{e^{+i\chi t} - e^{-i(\Delta - \chi)t}}{\Delta} + \xi^2 \frac{1 - e^{-i(\Delta - \chi)t}}{(\Delta - \chi)} \right] \Omega^\dagger \psi(t) \\
 &\approx \omega\psi - \frac{1}{4}\Omega \left[\Delta^{-1} + \xi^2 (\Delta - \chi)^{-1} \right] \Omega^\dagger \psi
 \end{aligned} \tag{4.16}$$

In the last step we have dropped all terms that correspond to quickly oscillating phase terms, because they average to zero on a time-scale much faster than the system dynamics. Eq. (4.16) gives rise to an effective Hamiltonian which contains two contributions associated to the two control laser fields where we have already set the ground state Hamiltonian $\omega = 0$.

$$H_{\text{eff}} = -\frac{1}{4}\Omega \left(\Delta^{-1} + \xi^2 (\Delta - \chi)^{-1} \right) \Omega^\dagger \tag{4.17}$$

$$i\partial_t\psi = H_{\text{eff}}\psi \tag{4.18}$$

These equations can now be applied to our specific system, i.e. photon generation in an atom-cavity system. We follow the notation of Ref. [40] that was already used in appendix A and define the Hamiltonian in the basis $|\Psi\rangle = (S, \mathcal{E}, P_1, P_2, P_3)^T$. The dynamics of the ground state $\psi = S$ are obtained upon adiabatic elimination of the excited states $\varepsilon = (\mathcal{E}, P_1, P_2, P_3)^T$.

$$H = \left(\begin{array}{c|cccc}
 0 & 0 & -\frac{1}{2}\Omega_1^* & -\frac{1}{2}\Omega_2^* & -\frac{1}{2}\Omega_3^* \\
 \hline
 0 & \delta - ik & -g_1 & -g_2 & -g_3 \\
 -\frac{1}{2}\Omega_1 & -g_1 & \Delta_1 - i\gamma & 0 & 0 \\
 -\frac{1}{2}\Omega_2 & -g_2 & 0 & \Delta_2 - i\gamma & 0 \\
 -\frac{1}{2}\Omega_3 & -g_3 & 0 & 0 & \Delta_3 - i\gamma
 \end{array} \right) = \left(\begin{array}{c|c}
 \omega & \frac{1}{2}\Omega \\
 \hline
 \frac{1}{2}\Omega^\dagger & \Delta
 \end{array} \right) \tag{4.19}$$

The Hamiltonian in Eq. (4.19) is divided into four submatrices and describes the couplings shown in Fig. 4.1(a). We use the abbreviation $\Omega_i = c_{si}\Omega$ and $g_i = c_{gi}g$ where c_{si} and c_{gi} are Clebsch-Gordan

coefficients that are introduced to describe the relative coupling strength of different transitions. We consider up to three (off-)resonant couplings with detunings Δ_i for the control beam and the cavity coupling and are thus able to describe any available level choice of ^{87}Rb . In order to find the effective Hamiltonian (4.17) we have to invert the matrix $\mathbf{\Delta}$ corresponding to the excited state Hilbert space [42]. The remaining differential equation (4.18) describes the evolution of the ground-state probability amplitude S and can be casted into the form $\dot{S} = -K' |\Omega|^2 S$ with the constant K' being defined in Eq. (4.20).

$$K' = iH_{\text{eff}} |\Omega|^{-2} = -i \frac{1}{4} \vec{c}^T \left(\mathbf{\Delta}^{-1} + \xi^2 (\mathbf{\Delta} - \chi)^{-1} \right) \vec{c} \quad (4.20)$$

$$\vec{c} = (0, c_{s1}, c_{s2}, c_{s3})^T \quad (4.21)$$

Here \vec{c} is a column vector containing the Clebsch-Gordan coefficients of the atomic levels. A solution for the time-evolution of the initial ground state is given in Eq. (4.22). The shape of the generated photon $\mathcal{E}_{\text{out}}(t)$ depends on the solution for S and defines the parameter L [40]. The solution for the constant parameter L is shown in Eq. (4.24) with $\vec{e}_1^T = (1, 0, 0, 0)$.

$$S = S(t_0) \exp \left(-K' \int_{t_0}^t dt' |\Omega(t')|^2 \right) \quad (4.22)$$

$$\mathcal{E}_{\text{out}} = \sqrt{\eta_{\text{esc}}} L \Omega S \quad (4.23)$$

$$L = \sqrt{2\kappa} \frac{1}{2} \vec{e}_1^T \mathbf{\Delta}^{-1} \vec{c} \quad (4.24)$$

With the parameters K' and L at hand we can compute the efficiency following Ref. [40], which takes the same form as in the case of a single control laser frequency. However, the parameter K' is modified by the second control beam. We obtain the optimal control pulse (4.7) with modified parameter $K \rightarrow K'$ and the corresponding photon retrieval efficiency η_R from the discussion in appendix A.

$$\eta_R = \int_{-\infty}^{+\infty} |\mathcal{E}_{\text{out}}|^2 dt \approx \eta_{\text{esc}} \frac{|L|^2}{2\Re(K')}$$

The photon generation efficiency $\eta_G = |L|^2 / (2\Re(K'))$ is shown in Fig. 4.4(a) as function of the detuning of the master beam Δ and relative detuning χ between the support beam and the master beam. Here, we assume two-photon resonance $\delta = 0$ of the cavity with the master beam and a relative field strength of the two optical components $\xi = 1$. For the sake of simplicity we only discuss the case of coupling to a single excited state. For certain parameter choices we recover an efficiency of $2C/(2C + 1)$ which is the maximally achievable efficiency for single-tone driving. Furthermore, we observe that the efficiency is reduced in the vicinity of $\chi = 0$ and $\Delta = \chi$. The latter case corresponds to a parameter choice sketched in Fig. 4.4(b) where the detuning of the support beam $\Delta_s = \Delta - \chi = 0$ vanishes. Since we assume two-photon resonance of the cavity with the master beam, this corresponds to a photon generation attempt that is effective highly two-photon off-resonant, since the resonant coupling of the support beam dominates the atomic driving. Note that the same result was obtained from a calculation based on the effective operator formalism presented in appendix B.

The efficiency reduction in the vicinity of $\chi = 0$ is a technical artefact attributed to the adiabatic approximation technique. In order to derive the effective Hamiltonian in Eq. (4.16) we have dropped

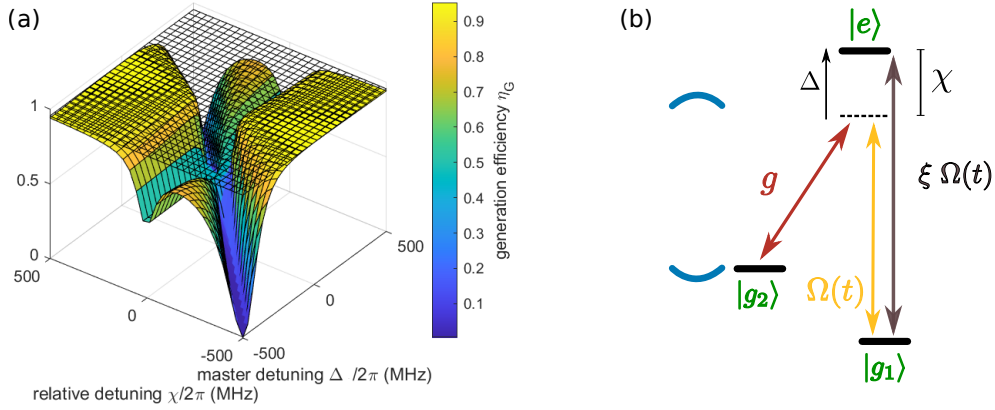


Figure 4.4: (a) Photon generation efficiency η_G as function of the detuning of the master beam Δ and relative detuning of the support beam with respect to the master beam χ . The maximal value of $2C/(2C + 1)$ is marked by the grid. Here, we take only the coupling to a single excited state into account. The level diagram is shown in (b) with the detunings corresponding to the case $\Delta = \chi$. In this case the photon generation efficiency is reduced.

contributions with rapidly rotating phase terms arguing that they average out on time-scales much faster than the system dynamics. However, the contributions of the form $e^{\pm i\chi t}$ depend on the relative detuning χ and are only negligible for sufficiently large relative detunings $\chi \gg 0$. In the vicinity of $\chi \approx 0$ we therefore observe “artificial resonances” that do not have a physical interpretation.

In this section we theoretically investigated photon generation with a bichromatic driving field. Using an adiabatic approximation technique we overcome technical limits of the commonly used adiabatic elimination technique. We find that the photon generation efficiency with a bichromatic driving field approaches the well known limit of $2C/(2C + 1)$ that is obtained also for single-tone control fields [36]. In the following we apply two-tone driving to compensate the dynamical light shift of the control pulse.

4.3.2 Chirp Compensation.

For any non-zero single photon detuning the control laser pulse with time-dependent Rabi frequency $\Omega(t)$ induces a time-dependent light shift [36]. In this section we will show that two-tone driving can provide build-in chirp compensation by choosing the relative strength ξ and detuning χ such that the dynamical light shift is suppressed. From Eq. (4.7) it can be seen that the required phase modulation is proportional to $\frac{\Im(K')}{2\Re(K')}$. The chirp is thus compensated whenever the imaginary part of the K' parameter vanishes. Our goal is to find an expression for the two-tone control laser parameters ξ and χ for such a scenario. We impose the condition $\Im(K') = 0$ and solve the equation for the relative field strength ξ which describes the relative strength of the support beam compared to the master beam. The resulting *chirp compensation equation* (4.25) specifies the relative strength of the support beam in order to guarantee chirp compensation.

$$\xi = \sqrt{\frac{-\Re(\vec{c}^T \Delta^{-1} \vec{c})}{\Re(\vec{c}^T (\Delta - \chi)^{-1} \vec{c})}} \quad (4.25)$$

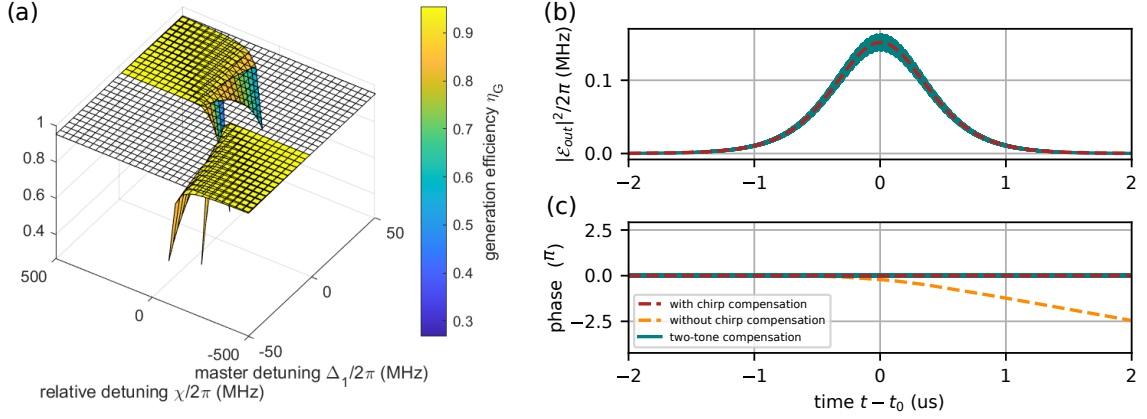


Figure 4.5: (a) Photon generation efficiency achieved under two-tone compensation conditions. For certain parameter choices the photon generation efficiency approaches the maximal value of $\eta_G = 2C/(2C + 1)$ marked by the grid. Here, we assume a three-level Λ -system with a single excited state. Similar results are obtained if the off-resonant coupling to additional electronically excited states is taken into account. (b-c) Comparison of two-tone compensation with active phase modulation based on numerically computed solutions of the equations of motion. The modulus squared (b) of the generated photon is shown for a hyperbolic secant with $T = 1 \mu\text{s}$. The shape obtained under two-tone compensation conditions is very similar to the result obtained for active phase modulation. The phase (c) of the generated photon is chirped in the absence of chirp-compensation. In contrast the phase is constant over time in case of two-tone compensation or active phase modulation.

We insert Eq. (4.25) into the expression for the efficiency and thereby find the achievable efficiency under chirp compensation conditions. The corresponding efficiency is shown in Fig. 4.5(a) and reaches the maximum value of $2C/(2C + 1)$.

In order to confirm that two-tone driving allows for built-in phase compensation we solve the system dynamics numerically. The results are presented in Fig 4.5(b-c). The phase of the generated photon is chirped if the control laser pulse does not include an active phase compensation. However, the phase of the generated photon remains constant when two-tone driving is used without active phase modulation of the control laser beam.

The presented two-tone chirp compensation technique provides an alternative to active phase modulation of the control laser pulse. Controlling the phase evolution of the single-photon temporal wavefunction is a requirement for efficient light-matter interaction [40]. In particular for the generation of temporally short photons the phase chirp reduces not only the generation fidelity, but also affects the spectral overlap with the cavity resonance. This can be seen by considering the Fourier transform $\mathcal{F}[e](\omega_{\mathcal{F}})$ for a photon pulse $e(t)$. Any time-dependent phase term of the form $e(t) \cdot e^{-i\phi(t)} = e(t) \cdot \Phi(t)$ affects the Fourier transform as shown in Eq. (4.26) according to the convolution theorem. Here $*$ denotes the convolution.

$$\mathcal{F}[e \cdot \Phi] = \sqrt{2\pi} (\mathcal{F}[e] * \mathcal{F}[\Phi]) (\omega_{\mathcal{F}}) = \sqrt{2\pi} \int_{-\infty}^{+\infty} \mathcal{F}[e](\omega_{\mathcal{F}} - \omega') \mathcal{F}[\Phi](\omega') d\omega' \quad (4.26)$$

Considering a time-dependent phase $\phi(t)$, we note that the first derivative $\dot{\phi}$ acts as a displacement on the frequency axis since it yields a Fourier transform of $\mathcal{F}[\Phi](\omega_{\mathcal{F}}) = \sqrt{2\pi} \delta(\omega_{\mathcal{F}} - \dot{\phi})$ if higher order derivatives are neglected. Here $\delta(\cdot)$ denotes the Dirac delta function and one obtains $\mathcal{F}[e \cdot \Phi](\omega_{\mathcal{F}}) =$

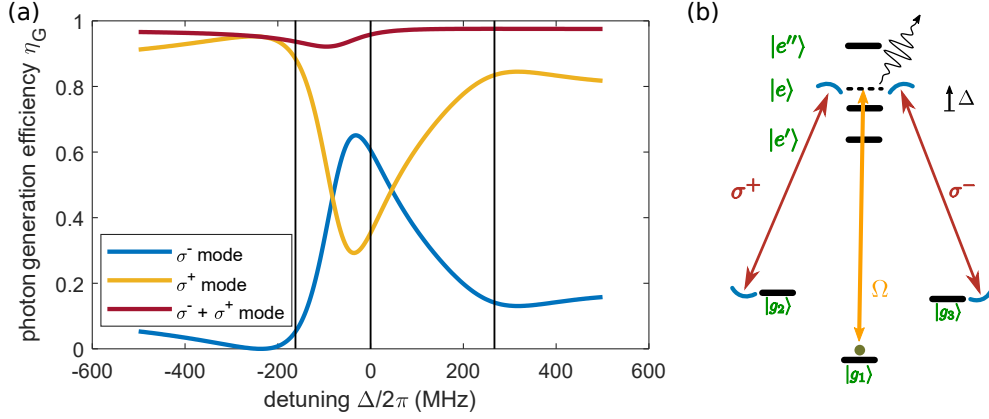


Figure 4.6: (a) The photon generation efficiency η_G is shown as function of the single-photon detuning Δ for a cavity with two degenerate polarization modes. The branching ratio of emission into the two degenerate modes can be tuned by exploiting the off-resonant coupling to three excited states. The total photon generation efficiency (given by the sum of σ^- and σ^+ mode) is only weakly affected by the detuning. (b) The atomic level scheme contains three ground-states that are coupled via the control laser beam and the cavity. Two degenerate cavity modes with orthogonal polarization are taken into account. The off-resonant coupling to three excited states allows to tune the ratio of photon emission into the two polarization modes.

$\mathcal{F}[e](\omega_{\mathcal{F}} - \phi)$. Therefore, a time-dependent phase modifies to first order the spectral overlap of the generated photon with the cavity linewidth which can become relevant for short pulses. Chirp-compensation is thus a requirement for efficient light-matter interaction and can be achieved either via active phase modulation of the control laser beam or by means of the presented two-tone compensation technique. The latter, requires only a single amplitude modulator and does not involve a phase modulation.

In the following we generalize the calculations to a cavity with two degenerate polarization modes.

4.4 Photon Generation in a Two-Mode Cavity with Multilevel Atoms

In this section we consider photon generation using a cavity with two degenerate and orthogonal polarization modes. Furthermore, we also take into account off-resonant couplings to three electronic excited states as sketched in Fig. 4.6(b). The presented results are valid for existing atomic levels in ^{87}Rb where the initial ground state $|g_1\rangle$ corresponds to the state $|F = 1, m_f = -1\rangle$. In order to derive an analytic solution for the photon generation efficiency η_R we follow the adiabatic approximation technique and start by extending the Hamiltonian (4.19) by a second cavity mode. Following the notation of Sec. 4.3.1 we obtain the extended Hamiltonian (4.27) written in the basis $|\Psi\rangle = (S, \mathcal{E}^+, \mathcal{E}^-, P_1, P_2, P_3)^T$.

$$H = \begin{pmatrix} 0 & 0 & 0 & -\frac{1}{2}\Omega_1^* & -\frac{1}{2}\Omega_2^* & -\frac{1}{2}\Omega_3^* \\ 0 & \delta - i\kappa & 0 & -g_1^+ & -g_2^+ & -g_3^+ \\ 0 & 0 & \delta - i\kappa & -g_1^- & -g_2^- & -g_3^- \\ -\frac{1}{2}\Omega_1 & -g_1^+ & -g_1^- & \Delta_1 - i\gamma & 0 & 0 \\ -\frac{1}{2}\Omega_2 & -g_2^+ & -g_2^- & 0 & \Delta_2 - i\gamma & 0 \\ -\frac{1}{2}\Omega_3 & -g_3^+ & -g_3^- & 0 & 0 & \Delta_3 - i\gamma \end{pmatrix} = \begin{pmatrix} \omega & & \\ & \frac{1}{2}\Omega^\dagger & \\ & & \Delta \end{pmatrix} \quad (4.27)$$

Here, we use again $\Omega_i = c_{si}\Omega$ to describe the coupling strength of the ground state to the excited state $|P_i\rangle$ and $g_i^\pm = c_{gi}^\pm g$ to describe the coupling strength of state $|P_i\rangle$ to the σ^\pm polarized cavity mode. We carry out adiabatic elimination of the excited Hilbert space and cast the remaining differential equation into the form $\dot{S} = -K'' |\Omega|^2 S$. Here the constant K'' depends again on the matrix inverse Δ^{-1} of the excited state Hilbert subspace and is defined in Eq. (4.28). The probability amplitudes of the generated photons are given by $\mathcal{E}_{\text{out}}^\pm = \sqrt{\eta_{\text{esc}}} L^\pm \Omega S$ for σ^\pm polarization. The parameters L^+ and L^- are defined in Eq. (4.29) and Eq. (4.30), respectively.

$$K'' = -i \frac{1}{4} \vec{c}^T \Delta^{-1} \vec{c} \quad (4.28)$$

$$L^+ = \sqrt{2\kappa} \frac{1}{2} \vec{e}_1^T \Delta^{-1} \vec{c} \quad (4.29)$$

$$L^- = \sqrt{2\kappa} \frac{1}{2} \vec{e}_2^T \Delta^{-1} \vec{c} \quad (4.30)$$

Note that the excited state Hilbert space is 5-dimensional in this case and hence the vectors $\vec{c} = (0, 0, c_{s1}, c_{s2}, c_{s3})^T$, $\vec{e}_1 = (1, 0, 0, 0, 0)^T$ and $\vec{e}_2 = (0, 1, 0, 0, 0)^T$ are also 5-dimensional. We have expressed the relevant terms that are involved in calculating the photon generation efficiency with simple vector matrix products. This formulation simplifies the calculation of η_G considerably. The only task left to do is finding the inverse of the excited state Hilbert subspace Δ^{-1} which is readily available. Computing the remaining products is straight forward which makes the presented adiabatic approximation technique an extremely useful and versatile tool.

The photon generation efficiency $\eta_G^\pm = \frac{|L^\pm|^2}{2\Re(K'')}$ for the σ^\pm -mode is shown in Fig. 4.6(a) as function of the single-photon detuning Δ with respect to the $F = 2 \rightarrow F' = 2$ transition of ^{87}Rb . The emission efficiency of the two cavity modes depends on the single-photon detuning Δ . For example for a detuning of $\Delta/2\pi \approx -240$ MHz the emission into the σ^- -mode is suppressed in favour of emission into the σ^+ -mode. Moreover, for suitable parameter choices (e.g. $\Delta/2\pi \approx -80$ MHz) the emission probabilities can be matched in order to generate single photons in a balanced polarization state $|p\rangle = \frac{1}{\sqrt{2}} (|\sigma^+\rangle + |\sigma^-\rangle)$.

The precise control over the branching ratio of σ^+ and σ^- polarized photon emission can open up interesting possibilities in the context of quantum networks [17, 22]. For example such an atom-cavity system at the node of a quantum network can switch between emission into purely σ^+ polarized photons or emission into a balanced polarization superposition. The latter scenario is well known to create entanglement between the photonic polarization and the atomic spin states [90]. This forms the basis of entanglement distribution between such emitter systems via an optical Bell measurement [41, 91]. The projection probability onto a maximally entangled emitter-emitter state is given by Eq. (4.31) and reaches a maximum probability of 50% [27].

$$P_{\text{Bell}} = 2 \left(\frac{r}{r^2 + 1} \right)^2 \quad (4.31)$$

Here r denotes the branching ratio of emission into the σ^+ compared to emission into the σ^- mode. Note that the success rate for entanglement distribution is directly proportional to the Bell state projection probability P_{Bell} and hence its beneficial to maximize the later. This can be achieved by using the off-resonant coupling to additional electronically excited states in order to tune the branching ratio $r(\Delta)$ by choosing a suitable single-photon detuning Δ . Thereby a balanced emission into both cavity modes ($r = 1$) can be achieved which maximizes the Bell state projection probability.

Summary and Outlook

In this thesis, I presented fluorescence imaging of ^{87}Rb atoms inside an optical cavity using the Raman imaging technique. The first part describes precision measurements of differential light shifts that occur during continuous Raman sideband cooling. The light shifts are caused by the optical repumper beam and modify the two-photon resonance of the Raman coupling. The cooling process is modelled by means of a three-level system that takes into account the Raman coupling and the repumping process [59]. We find qualitative agreement between the estimated and the measured light shifts. In addition, we identified the optimum cooling parameters and confirmed that near ground-state cooling is achieved. We also observe that it is beneficial to detune the optical repumping beam away from resonance in order to suppress detrimental heating due to dipole-force fluctuations [31, 34].

The characterization of differential light shifts is subsequently used to optimize the fluorescence imaging of atoms inside the resonator. We implement Raman imaging which is based on detecting the repumper fluorescence during continuous Raman sideband cooling. The complexity of the parameter space is reduced via a two-photon feed-forward which maintains the resonance with the Raman cooling sideband when varying the repumper parameters. A new imaging system was installed in order to suppress spurious background light that was blinding the camera. The optimization of the fluorescence is discussed and a mean signal-to-noise ratio of about six is obtained for an exposure time of 1 s. Using the cavity-based atom detection we independently measure the probability that a single atom survives the exposure time. We obtain survival probabilities exceeding 80 % and lifetimes up to 55 s which are believed to be vacuum-limited. In conclusion, Raman imaging is successfully applied to image small atomic ensembles inside the resonator. This constitutes the first step towards photon storage experiments with multiple atoms.

In addition, I presented theoretical calculations regarding photon generation in an atom-cavity system. The shaping of the single-photon temporal wavefunction is discussed which is based on tailoring the corresponding control laser pulse. For sufficiently smooth temporal envelopes any pulse shape can be generated as long as the dynamics are adiabatic [36]. We study the breakdown of the adiabatic approximation for our cavity parameters by means of numerical simulations and find that the photon generation fidelity drops when the characteristic pulse time T_c approaches the inverse cavity linewidth $\kappa^{-1} \approx 4$ ns. The control laser pulse with time-dependent Rabi frequency $\Omega(t)$ induces light shifts on the atomic levels. Thereby, a phase chirp is imprinted onto the generated photon which reduces the photon generation fidelity if no chirp-compensation is applied [40]. As an alternative to chirp compensation via active phase modulation of the control laser beam, I presented a mechanism

for passive chirp compensation based on a bichromatic driving field. This scheme makes use of two optical frequency components that mutually cancel each others light shifts. Implementing the latter requires only a single amplitude modulator and no additional phase modulator.

Theoretical work mostly describes photon generation by means of an atomic Λ -system with one electronic excited state [36, 39]. In real atoms there are, however, additional excited states present. The off-resonant coupling to several excited states can cause a destructive interference which reduces the photon emission efficiency for certain parameter choices. I presented an extension of the calculations in Ref. [40] to model photon generation in a Tripod level configuration [29]. This model takes into account a second degenerate cavity mode with orthogonal polarization and includes off-resonant couplings to multiple excited states. In this case, the off-resonant couplings can be exploited to tune the branching ratio of photon emission into the two degenerate orthogonal polarization modes of the cavity. Thereby, the photon emission can be guided into a balanced polarization superposition state. This provides means of maximizing the Bell state projection probability of entanglement distribution schemes [27, 41].

Outlook

In order to facilitate photon storage and retrieval experiments with multiple atoms, we are currently working on techniques to prepare small atomic ensembles inside the resonator mode. To this end, we would like to count the number of atoms. Since we do not spatially resolve individual lattice sites, we rely on the integrated fluorescence for counting. However, the preliminary fluorescence histogram presented in Sec. 3.3 shows that the detected fluorescence is so far insufficient for counting. We envisage to investigate the influence of the motional ground state onto fluorescence histograms. Note that the motional ground state of the $|F = 2, m_f = -2\rangle$ state is dark with respect to the Raman coupling and the repumper beam and thus does not generate fluorescence. In order to “brighten” the dark state we will apply a weak parametric excitation by modulating the dipole trap intensity at twice its trapping frequency [60, 74]. Thereby, atoms are expected to be heated out of the motional dark state and are reintroduced into the fluorescence cycle. Fluorescence based atom counting enables the post-selection of measurement on the size of the atomic ensemble. It thus paves the way towards exploring the collective coupling of multiple atoms to the same resonator mode. This not only enhances the effective coupling strength, but also permits the study of entangled multi-particle states [30, 92] which consequently facilitates many interesting experiments.

Bibliography

- [1] A. L. Schawlow and C. H. Townes, *Infrared and Optical Masers*, *Phys. Rev.* **112** (6 1958) 1940, URL: <https://link.aps.org/doi/10.1103/PhysRev.112.1940> (cit. on p. 1).
- [2] T. H. Maiman, *Stimulated Optical Radiation in Ruby*, *Nature* **187** (1960) 493, URL: <https://doi.org/10.1038/187493a0> (cit. on p. 1).
- [3] E. L. Raab et al., *Trapping of Neutral Sodium Atoms with Radiation Pressure*, *Phys. Rev. Lett.* **59** (23 1987) 2631, URL: <https://link.aps.org/doi/10.1103/PhysRevLett.59.2631> (cit. on p. 1).
- [4] A. Ashkin et al., *Observation of a single-beam gradient force optical trap for dielectric particles*, *Optics Letters* **11** (1986) 288, URL: <https://doi.org/10.1364/ol.11.000288> (cit. on p. 1).
- [5] C. Adams and E. Riis, *Laser cooling and trapping of neutral atoms*, *Progress in Quantum Electronics* **21** (1997) 1, URL: [https://doi.org/10.1016/s0079-6727\(96\)00006-7](https://doi.org/10.1016/s0079-6727(96)00006-7) (cit. on p. 1).
- [6] A. M. Steane and C. J. Foot, *Laser Cooling below the Doppler Limit in a Magneto-Optical Trap*, *Europhysics Letters (EPL)* **14** (1991) 231, URL: <https://doi.org/10.1209%2F0295-5075%2F14%2F3%2F008> (cit. on pp. 1, 3).
- [7] C. Monroe et al., *Resolved-Sideband Raman Cooling of a Bound Atom to the 3D Zero-Point Energy*, *Phys. Rev. Lett.* **75** (22 1995) 4011, URL: <https://link.aps.org/doi/10.1103/PhysRevLett.75.4011> (cit. on p. 1).
- [8] A. J. Kerman et al., *Beyond Optical Molasses: 3D Raman Sideband Cooling of Atomic Cesium to High Phase-Space Density*, *Phys. Rev. Lett.* **84** (3 2000) 439, URL: <https://link.aps.org/doi/10.1103/PhysRevLett.84.439> (cit. on p. 1).
- [9] A. Einstein, B. Podolsky and N. Rosen, *Can Quantum-Mechanical Description of Physical Reality Be Considered Complete?*, *Phys. Rev.* **47** (10 1935) 777, URL: <https://link.aps.org/doi/10.1103/PhysRev.47.777> (cit. on p. 1).
- [10] W. Tittel et al., *Violation of Bell Inequalities by Photons More Than 10 km Apart*, *Phys. Rev. Lett.* **81** (17 1998) 3563, URL: <https://link.aps.org/doi/10.1103/PhysRevLett.81.3563> (cit. on p. 1).

- [11] G. E. Marti et al.,
Imaging Optical Frequencies with 100 μ Hz Precision and 1.1 μ m Resolution,
Phys. Rev. Lett. **120** (10 2018) 103201,
URL: <https://link.aps.org/doi/10.1103/PhysRevLett.120.103201> (cit. on p. 1).
- [12] A. Acín et al., *The quantum technologies roadmap: a European community view*,
New Journal of Physics **20** (2018) 080201,
URL: <https://doi.org/10.1088%2F1367-2630%2Faad1ea> (cit. on p. 1).
- [13] C. H. Bennett and G. Brassard,
Quantum cryptography: Public key distribution and coin tossing,
Theoretical Computer Science **560** (2014) 7,
URL: <https://doi.org/10.1016/j.tcs.2014.05.025> (cit. on p. 1).
- [14] C. O'Dwyer et al.,
A feed-forward measurement scheme for periodic noise suppression in atomic magnetometry,
Review of Scientific Instruments **91** (2020) 045103,
URL: <https://doi.org/10.1063/5.0002964> (cit. on p. 1).
- [15] J. I. Cirac and P. Zoller, *Goals and opportunities in quantum simulation*,
Nature Physics **8** (2012) 264, URL: <https://doi.org/10.1038/nphys2275> (cit. on p. 1).
- [16] I. Bloch, J. Dalibard and S. Nascimbène, *Quantum simulations with ultracold quantum gases*,
Nature Physics **8** (2012) 267, URL: <https://doi.org/10.1038/nphys2259> (cit. on p. 1).
- [17] H. J. Kimble, *The quantum internet*, *Nature* **453** (2008) 1023,
URL: <https://doi.org/10.1038/nature07127> (cit. on pp. 1, 46).
- [18] D. Jaksch et al., *Fast Quantum Gates for Neutral Atoms*, *Phys. Rev. Lett.* **85** (10 2000) 2208,
URL: <https://link.aps.org/doi/10.1103/PhysRevLett.85.2208> (cit. on p. 1).
- [19] H. P. Specht et al., *A single-atom quantum memory*, *Nature* **473** (2011) 190,
URL: <https://doi.org/10.1038/nature09997> (cit. on p. 1).
- [20] W. K. Wootters and W. H. Zurek, *The no-cloning theorem*, *Physics Today* **62** (2009) 76,
URL: <https://doi.org/10.1063/1.3086114> (cit. on p. 1).
- [21] C. H. Bennett et al., *Teleporting an unknown quantum state via dual classical and Einstein-Podolsky-Rosen channels*, *Phys. Rev. Lett.* **70** (13 1993) 1895,
URL: <https://link.aps.org/doi/10.1103/PhysRevLett.70.1895> (cit. on p. 1).
- [22] H.-J. Briegel et al.,
Quantum Repeaters: The Role of Imperfect Local Operations in Quantum Communication,
Phys. Rev. Lett. **81** (26 1998) 5932,
URL: <https://link.aps.org/doi/10.1103/PhysRevLett.81.5932> (cit. on pp. 1, 46).
- [23] J. Gallego et al., *Strong Purcell Effect on a Neutral Atom Trapped in an Open Fiber Cavity*,
Phys. Rev. Lett. **121** (17 2018) 173603,
URL: <https://link.aps.org/doi/10.1103/PhysRevLett.121.173603>
(cit. on pp. 1–3).
- [24] L. Béguin et al., *On-demand semiconductor source of 780-nm single photons with controlled temporal wave packets*, *Phys. Rev. B* **97** (20 2018) 205304,
URL: <https://link.aps.org/doi/10.1103/PhysRevB.97.205304> (cit. on p. 2).

-
- [25] H. Wang et al., *On-Demand Semiconductor Source of Entangled Photons Which Simultaneously Has High Fidelity, Efficiency, and Indistinguishability*, *Phys. Rev. Lett.* **122** (11 2019) 113602, URL: <https://link.aps.org/doi/10.1103/PhysRevLett.122.113602> (cit. on p. 2).
- [26] M. K. Bhaskar et al., *Experimental demonstration of memory-enhanced quantum communication*, *Nature* **580** (2020) 60, URL: <https://doi.org/10.1038/s41586-020-2103-5> (cit. on p. 2).
- [27] H. Takahashi et al., *Strong Coupling of a Single Ion to an Optical Cavity*, *Physical Review Letters* **124** (2020), URL: <https://doi.org/10.1103/physrevlett.124.013602> (cit. on pp. 2, 33, 46, 48).
- [28] M. Mücke et al., *Generation of single photons from an atom-cavity system*, *Phys. Rev. A* **87** (6 2013) 063805, URL: <https://link.aps.org/doi/10.1103/PhysRevA.87.063805> (cit. on pp. 2, 33).
- [29] T. Macha et al., *Nonadiabatic storage of short light pulses in an atom-cavity system*, *Phys. Rev. A* **101** (5 2020) 053406, URL: <https://link.aps.org/doi/10.1103/PhysRevA.101.053406> (cit. on pp. 2, 33, 35, 48).
- [30] F. Haas et al., *Entangled States of More Than 40 Atoms in an Optical Fiber Cavity*, *Science* **344** (2014) 180, URL: <https://doi.org/10.1126/science.1248905> (cit. on pp. 2, 48).
- [31] M. Martinez-Dorantes et al., *State-dependent fluorescence of neutral atoms in optical potentials*, *Phys. Rev. A* **97** (2018) 023410 (cit. on pp. 2, 20, 22, 23, 47).
- [32] J. F. Sherson et al., *Single-atom-resolved fluorescence imaging of an atomic Mott insulator*, *Nature* **467** (2010) 68, URL: <https://doi.org/10.1038/nature09378> (cit. on pp. 2, 23).
- [33] A. Omran et al., *Microscopic Observation of Pauli Blocking in Degenerate Fermionic Lattice Gases*, *Phys. Rev. Lett.* **115** (26 2015) 263001, URL: <https://link.aps.org/doi/10.1103/PhysRevLett.115.263001> (cit. on pp. 2, 23).
- [34] L. W. Cheuk et al., *Quantum-Gas Microscope for Fermionic Atoms*, *Phys. Rev. Lett.* **114** (19 2015) 193001, URL: <https://link.aps.org/doi/10.1103/PhysRevLett.114.193001> (cit. on pp. 2, 21–24, 47).
- [35] P. B. R. Nisbet-Jones et al., *Highly efficient source for indistinguishable single photons of controlled shape*, *New Journal of Physics* **13** (2011) 103036, URL: <https://doi.org/10.1088/1367-2630/13/10/103036> (cit. on pp. 2, 34).
- [36] A. V. Gorshkov et al., *Photon storage in Λ -type optically dense atomic media. I. Cavity model*, *Physical Review A* **76** (2007), URL: <https://doi.org/10.1103/physreva.76.033804> (cit. on pp. 2, 33–35, 41, 43, 47, 48, 57, 58).

- [37] J. Dilley et al., *Single-photon absorption in coupled atom-cavity systems*, *Phys. Rev. A* **85** (2 2012) 023834, URL: <https://link.aps.org/doi/10.1103/PhysRevA.85.023834> (cit. on pp. 2, 34, 35).
- [38] M. Fleischhauer, S. Yelin and M. Lukin, *How to trap photons? Storing single-photon quantum states in collective atomic excitations*, *Optics Communications* **179** (2000) 395, URL: [https://doi.org/10.1016/s0030-4018\(99\)00679-3](https://doi.org/10.1016/s0030-4018(99)00679-3) (cit. on pp. 2, 34, 35).
- [39] L. Giannelli et al., *Optimal storage of a single photon by a single intra-cavity atom*, *New Journal of Physics* **20** (2018) 105009, URL: <https://doi.org/10.1088/1367-2630/aae725> (cit. on pp. 2, 34, 35, 48, 61, 63).
- [40] O. Morin et al., *Deterministic Shaping and Reshaping of Single-Photon Temporal Wave Functions*, *Phys. Rev. Lett.* **123** (13 2019) 133602, URL: <https://link.aps.org/doi/10.1103/PhysRevLett.123.133602> (cit. on pp. 2, 3, 33–36, 39, 41, 42, 44, 47, 48, 57, 59).
- [41] L.-M. Duan et al., *Long-distance quantum communication with atomic ensembles and linear optics*, *Nature* **414** (2001) 413, URL: <https://doi.org/10.1038/35106500> (cit. on pp. 2, 46, 48).
- [42] V. Paulisch et al., *Beyond adiabatic elimination: A hierarchy of approximations for multi-photon processes*, *The European Physical Journal Plus* **129** (2014), URL: <https://doi.org/10.1140/epjp/i2014-14012-8> (cit. on pp. 3, 33, 40–42).
- [43] J. Zachorowski, T. Pałasz and G. Wojciech, *Magneto-optical trap for cold rubidium atoms*, *Optica Applicata* **28** (1998) 239 (cit. on p. 3).
- [44] R. Grimm, M. Weidemüller and Y. B. Ovchinnikov, “Optical Dipole Traps for Neutral Atoms”, *Advances In Atomic, Molecular, and Optical Physics*, Elsevier, 2000 95, URL: [https://doi.org/10.1016/s1049-250x\(08\)60186-x](https://doi.org/10.1016/s1049-250x(08)60186-x) (cit. on pp. 3, 7, 12).
- [45] D. Schrader et al., *An optical conveyor belt for single neutral atoms*, *Applied Physics B* **73** (2001) 819, URL: <https://doi.org/10.1007/s003400100722> (cit. on p. 3).
- [46] T. N. Macha, *Storage of Short Light Pulses in a Fiber-Based Atom-Cavity System*, PhD thesis: Universität Bonn, 2018 (cit. on p. 3).
- [47] E. Uruñuela et al., *Ground-State Cooling of a Single Atom in a High-Bandwidth Cavity*, *Phys. Rev. A* **101** (2020) 023415 (cit. on pp. 3, 23).
- [48] R. W. P. Drever et al., *Laser phase and frequency stabilization using an optical resonator*, *Applied Physics B Photophysics and Laser Chemistry* **31** (1983) 97, URL: <https://doi.org/10.1007/bf00702605> (cit. on p. 3).
- [49] M. Ammenwerth, *Analysing a phase-frequency lock of a laser to an optical frequency comb*, Bachelor thesis: Universität Bonn, 2017 (cit. on p. 3).

-
- [50] L. Ahlheit, *Frequenzvariable Phasenstabilisierung eines Diodenlasers auf einen optischen Frequenzkamm*, Bachelor thesis: Universität Bonn, 2017 (cit. on p. 3).
- [51] J. C. G. Fernández, *Strong Coupling between Small Atomic Ensembles and an Open Fiber Cavity*, PhD thesis: Universität Bonn, 2017 (cit. on pp. 4, 5, 14, 16).
- [52] C. J. Foot, *Atomic physics*, Oxford master series in atomic, optical and laser physics, Oxford University Press, 2007, URL: <https://cds.cern.ch/record/1080846> (cit. on pp. 4, 8).
- [53] D. A. Steck, *Rubidium 87 D Line Data*, available online at <http://steck.us/alkalidata> (revision 2.2.1, 21 November 2019). (cit. on pp. 4, 15, 16).
- [54] E. Jaynes and F. Cummings, *Comparison of quantum and semiclassical radiation theories with application to the beam maser*, *Proceedings of the IEEE* **51** (1963) 89, URL: <https://doi.org/10.1109/proc.1963.1664> (cit. on p. 4).
- [55] S. Haroche, “Course 2 Mesoscopic state superpositions and decoherence in quantum optics”, *Quantum Entanglement and Information Processing, École d’été de Physique des Houches Session LXXIX*, Elsevier, 2004 55, URL: [https://doi.org/10.1016/s0924-8099\(03\)80026-4](https://doi.org/10.1016/s0924-8099(03)80026-4) (cit. on p. 4).
- [56] H. Perrin et al., *Sideband cooling of neutral atoms in a far-detuned optical lattice*, *Europhysics Letters (EPL)* **42** (1998) 395, URL: <https://doi.org/10.1209/2Fepl%2Fi1998-00261-y> (cit. on pp. 7, 9).
- [57] R. Reimann et al., *Carrier-free Raman manipulation of trapped neutral atoms*, *New Journal of Physics* **16** (2014) 113042, URL: <https://doi.org/10.1088/1367-2630/16/11/113042> (cit. on pp. 7, 9, 10).
- [58] P. Malik, *Linewidth-reduced DBR Laser for Raman Sideband Cooling*, Masterthesis: Universität Bonn, 2020 (cit. on pp. 7, 9, 10, 30).
- [59] T. A. Hilker, *Spin-Resolved Microscopy of Strongly Correlated Fermionic Many-Body States*, PhD thesis: LMU München, 2017 (cit. on pp. 7, 13, 22, 47).
- [60] W. Alt et al., *Single atoms in a standing-wave dipole trap*, *Phys. Rev. A* **67** (3 2003) 033403, URL: <https://link.aps.org/doi/10.1103/PhysRevA.67.033403> (cit. on pp. 8, 48).
- [61] T. Arpornthip, C. A. Sackett and K. J. Hughes, *Vacuum-pressure measurement using a magneto-optical trap*, *Phys. Rev. A* **85** (3 2012) 033420, URL: <https://link.aps.org/doi/10.1103/PhysRevA.85.033420> (cit. on p. 11).
- [62] H. J. Charmichael, *Statistical Methods in Quantum Optics 1: Master Equations and Fokker-Planck Equations*, Springer, 2002 (cit. on pp. 13, 61).
- [63] N. Moiseyev, *Quantum theory of resonances: calculating energies, widths and cross-sections by complex scaling*, *Physics Reports* **302** (1998) 212, URL: [https://doi.org/10.1016/s0370-1573\(98\)00002-7](https://doi.org/10.1016/s0370-1573(98)00002-7) (cit. on pp. 14, 34).

- [64] C. W. Gardiner and P. Zoller, *Quantum noise*, 3rd Ed, Springer-Verlag, 2004 (cit. on p. 14).
- [65] L. Hao et al., *Transition from electromagnetically induced transparency to Autler–Townes splitting in cold cesium atoms*, *New Journal of Physics* **20** (2018) 073024, URL: <https://doi.org/10.1088%2F1367-2630%2Faaad153> (cit. on p. 15).
- [66] S. H. Autler and C. H. Townes, *Stark Effect in Rapidly Varying Fields*, *Phys. Rev.* **100** (2 1955) 703, URL: <https://link.aps.org/doi/10.1103/PhysRev.100.703> (cit. on p. 15).
- [67] K. B. Lee et al., *Application of the Stretched Exponential Function to Fluorescence Lifetime Imaging*, *Biophysical Journal* **81** (2001) 1265, URL: [https://doi.org/10.1016/s0006-3495\(01\)75784-0](https://doi.org/10.1016/s0006-3495(01)75784-0) (cit. on p. 16).
- [68] C. P. Pearman et al., *Polarization spectroscopy of a closed atomic transition: applications to laser frequency locking*, *Journal of Physics B: Atomic, Molecular and Optical Physics* **35** (2002) 5141, URL: <https://doi.org/10.1088%2F0953-4075%2F35%2F24%2F315> (cit. on p. 16).
- [69] C.-Y. Shih and M. S. Chapman, *Nondestructive light-shift measurements of single atoms in optical dipole traps*, *Phys. Rev. A* **87** (6 2013) 063408, URL: <https://link.aps.org/doi/10.1103/PhysRevA.87.063408> (cit. on p. 21).
- [70] M. Martinez-Dorantes et al., *Fast Nondestructive Parallel Readout of Neutral Atom Registers in Optical Potentials*, *Phys. Rev. Lett.* **119** (18 2017) 180503, URL: <https://link.aps.org/doi/10.1103/PhysRevLett.119.180503> (cit. on p. 23).
- [71] E. Haller et al., *Single-atom imaging of fermions in a quantum-gas microscope*, *Nature Physics* **11** (2015) 738, URL: <https://doi.org/10.1038/nphys3403> (cit. on p. 23).
- [72] M. F. Parsons et al., *Site-Resolved Imaging of Fermionic ${}^6\text{Li}$ in an Optical Lattice*, *Phys. Rev. Lett.* **114** (21 2015) 213002, URL: <https://link.aps.org/doi/10.1103/PhysRevLett.114.213002> (cit. on p. 23).
- [73] M. M. Dorantes, *Fast non-destructive internal state detection of neutral atoms in optical potentials*, PhD thesis: Universität Bonn, 2016 (cit. on p. 24).
- [74] B. J. Lester, A. M. Kaufman and C. A. Regal, *Raman cooling imaging: Detecting single atoms near their ground state of motion*, *Phys. Rev. A* **90** (1 2014) 011804, URL: <https://link.aps.org/doi/10.1103/PhysRevA.90.011804> (cit. on pp. 24, 31, 48).
- [75] Rayleigh, *XXXI. Investigations in optics, with special reference to the spectroscope*, *The London, Edinburgh, and Dublin Philosophical Magazine and Journal of Science* **8** (1879) 261, URL: <https://doi.org/10.1080/14786447908639684> (cit. on p. 29).
- [76] M. Born and E. Wolf, *Principles of optics: electromagnetic theory of propagation, interference and diffraction fo light*, Cambridge University Press, 1999 (cit. on p. 29).

-
- [77] A. Alberti et al., *Super-resolution microscopy of single atoms in optical lattices*, *New Journal of Physics* **18** (2016) 053010, URL: <https://doi.org/10.1088%2F1367-2630%2F18%2F5%2F053010> (cit. on p. 29).
- [78] W. Zhou, *Analyse der Punktspreizfunktion des Abbildungssystems vom DQSIM-Experiment anhand der Fluoreszenzaufnahmen*, Bachelor thesis: Universität Bonn, 2016 (cit. on p. 29).
- [79] E. Uruñuela, *Imaging and addressing of neutral atoms inside a fiber cavity*, Master thesis: Universität Bonn, 2017 (cit. on p. 29).
- [80] H. G. Barros et al., *Deterministic single-photon source from a single ion*, *New Journal of Physics* **11** (2009) 103004, URL: <https://doi.org/10.1088%2F1367-2630%2F11%2F10%2F103004> (cit. on p. 33).
- [81] A. Kuhn, M. Hennrich and G. Rempe, *Deterministic Single-Photon Source for Distributed Quantum Networking*, *Phys. Rev. Lett.* **89** (6 2002) 067901, URL: <https://link.aps.org/doi/10.1103/PhysRevLett.89.067901> (cit. on p. 33).
- [82] F. Reiter and A. S. Sørensen, *Effective operator formalism for open quantum systems*, *Phys. Rev. A* **85** (3 2012) 032111, URL: <https://link.aps.org/doi/10.1103/PhysRevA.85.032111> (cit. on pp. 33, 61).
- [83] L.-M. Duan and H. J. Kimble, *Efficient Engineering of Multiatom Entanglement through Single-Photon Detections*, *Phys. Rev. Lett.* **90** (25 2003) 253601, URL: <https://link.aps.org/doi/10.1103/PhysRevLett.90.253601> (cit. on p. 33).
- [84] A. E. B. Nielsen and J. Kerckhoff, *Efficient all-optical switch using a Λ atom in a cavity QED system*, *Phys. Rev. A* **84** (4 2011) 043821, URL: <https://link.aps.org/doi/10.1103/PhysRevA.84.043821> (cit. on p. 34).
- [85] C. M. Bender, *Making sense of non-Hermitian Hamiltonians*, *Reports on Progress in Physics* **70** (2007) 947, URL: <https://doi.org/10.1088%2F0034-4885%2F70%2F6%2Fr03> (cit. on p. 34).
- [86] O. Morin et al., *Accurate photonic temporal mode analysis with reduced resources*, *Phys. Rev. A* **101** (1 2020) 013801, URL: <https://link.aps.org/doi/10.1103/PhysRevA.101.013801> (cit. on p. 39).
- [87] S. Goreslavskii and V. Krainov, *Two-level atom in a bichromatic resonance field*, *Zh. Eksp. Teor. Fiz.* 76, 26-33 (1979) (cit. on pp. 40, 63).
- [88] D. X. Li and X. Q. Shao, *Rapid population transfer of a two-level system by a polychromatic driving field*, *Scientific Reports* **9** (2019), URL: <https://doi.org/10.1038/s41598-019-45558-5> (cit. on pp. 40, 63).
- [89] E. Brion, L. H. Pedersen and K. Mølmer, *Adiabatic elimination in a lambda system*, *Journal of Physics A: Mathematical and Theoretical* **40** (2007) 1033, URL: <https://doi.org/10.1088%2F1751-8113%2F40%2F5%2F011> (cit. on p. 40).

- [90] A. Stute et al., *Tunable ion–photon entanglement in an optical cavity*, *Nature* **485** (2012) 482,
URL: <https://doi.org/10.1038/nature11120> (cit. on p. 46).
- [91] N. Sangouard et al., *Quantum repeaters based on atomic ensembles and linear optics*,
Rev. Mod. Phys. **83** (1 2011) 33,
URL: <https://link.aps.org/doi/10.1103/RevModPhys.83.33> (cit. on p. 46).
- [92] F. Reiter, M. J. Kastoryano and A. S. Sørensen,
Driving two atoms in an optical cavity into an entangled steady state using engineered decay,
New Journal of Physics **14** (2012) 053022,
URL: <https://doi.org/10.1088/1367-2630/14/5/053022> (cit. on p. 48).
- [93] A. V. Gorshkov et al.,
Photon storage in Λ -type optically dense atomic media. II. Free-space model,
Phys. Rev. A **76** (3 2007) 033805,
URL: <https://link.aps.org/doi/10.1103/PhysRevA.76.033805> (cit. on p. 58).

Photon Generation in the Adiabatic Regime

In this section we present the derivation of the photon retrieval efficiency for an atom with multiple excited states using the standard adiabatic elimination method following Ref. [40]. An extension of the system of differential equations derived in Ref. [36] is presented in order to consider the effect of off-resonant couplings to multiple excited states. To derive the maximally achievable photon retrieval efficiency and the shape of the corresponding control laser pulse, we start with the set of coupled differential equations

$$\dot{\mathcal{E}} = -\kappa\mathcal{E} + ig_1P_1 + ig_2P_2 + \sqrt{2\eta_{\text{esc}}}\kappa\mathcal{E}_{\text{in}} \quad (\text{A.1})$$

$$\dot{P}_1 = -(\gamma + i\Delta_1)P_1 + ig_1\mathcal{E} + i\frac{1}{2}\Omega_1S \quad (\text{A.2})$$

$$\dot{P}_2 = -(\gamma + i\Delta_2)P_2 + ig_2\mathcal{E} + i\frac{1}{2}\Omega_2S \quad (\text{A.3})$$

$$\dot{P}_3 = -(\gamma + i\Delta_3)P_3 + i\frac{1}{2}\Omega_3S \quad (\text{A.4})$$

$$\dot{S} = i\frac{1}{2}\Omega_1^*P_1 + i\frac{1}{2}\Omega_2^*P_2 + i\frac{1}{2}\Omega_3^*P_3 \quad (\text{A.5})$$

Upon assuming the bad cavity limit (i.e. $\kappa \gg g$) adiabatic elimination is done by imposing $\dot{\mathcal{E}} \approx 0$ and $\dot{P}_i \approx 0$. This simplifies the system of equations to

$$\mathcal{E} = \frac{1}{\kappa} \left(ig_1P_1 + ig_2P_2 + \sqrt{2\eta_{\text{esc}}}\kappa\mathcal{E}_{\text{in}} \right) \quad (\text{A.6})$$

$$P_1 = \frac{1}{(\gamma + i\Delta_1)} \left(ig_1\mathcal{E} + i\frac{1}{2}\Omega_1S \right) \quad (\text{A.7})$$

$$P_2 = \frac{1}{(\gamma + i\Delta_2)} \left(ig_2\mathcal{E} + i\frac{1}{2}\Omega_2S \right) \quad (\text{A.8})$$

$$P_3 = \frac{1}{(\gamma + i\Delta_3)} \left(i\frac{1}{2}\Omega_3S \right) \quad (\text{A.9})$$

$$\dot{S} = i\frac{1}{2}\Omega_1^*P_1 + i\frac{1}{2}\Omega_2^*P_2 + i\frac{1}{2}\Omega_3^*P_3 \quad (\text{A.10})$$

Assuming photon retrieval (i.e. setting $\mathcal{E}_{\text{in}} = 0$) and inserting Eq. (A.7) and Eq. (A.8) into Eq. (A.6) yields a relation for the intra-cavity field amplitude \mathcal{E} as function of the initial state probability

amplitude S shown in Eq (A.11).

$$\mathcal{E} = \frac{-\frac{1}{2} \left[\frac{g_1 c_{s1}}{(\gamma+i\Delta_1)} + \frac{g_2 c_{s2}}{(\gamma+i\Delta_2)} \right]}{\kappa + \frac{g_1^2}{(\gamma+i\Delta_1)} + \frac{g_2^2}{(\gamma+i\Delta_2)}} \Omega S \quad (\text{A.11})$$

With relation (A.11) at hand we can express $P_i = P_i(\mathcal{E}, S) = P_i(S)$ and insert these relations into Eq. (A.10). Using the definition $g_i = c_{gi}g$ and $\Omega_i = c_{si}\Omega$ one finds a single ordinary linear differential equation (A.12) describing the evolution of the initial ground state with probability amplitude S .

$$\dot{S} = -K |\Omega|^2 S \quad (\text{A.12})$$

Here the time-independent prefactor K depends on system parameters and atomic level choices and is defined in Eq. (A.13).

$$K = \frac{1}{4} \left[\frac{c_{s1}^2 a_2 + c_{s2}^2 a_1 - 2c_{s2}c_{s1}b}{a_1 a_2 - b^2} + \frac{c_{s3}^2}{a_3} \right] \quad (\text{A.13})$$

We introduced $a_j = \gamma(1 + 2C_j) + i\Delta_j$ and $b = \frac{g_1 g_2}{\kappa}$ with $C_j = \frac{g_j^2}{2\kappa\gamma}$ in order to simplify the expressions. A solution of the differential equations (A.12) is given by:

$$S(t) = S(t_0) \exp \left(-K \int_{t_0}^t |\Omega(t')|^2 dt' \right) \quad (\text{A.14})$$

Using the input-output relation $\mathcal{E}_{\text{out}} = \sqrt{\eta_{\text{esc}}} \sqrt{2\kappa} \mathcal{E}$ and relation (A.11) we can express the output field as $\mathcal{E}_{\text{out}} = \sqrt{\eta_{\text{esc}}} L \Omega S$. Here the time-independent constant L is given by Eq. (A.15).

$$L = \sqrt{\gamma C} \frac{c_{g1}(c_{s1}a_2 - c_{s2}b) + c_{g2}(c_{s2}a_1 - c_{s1}b)}{b^2 - a_1 a_2} \quad (\text{A.15})$$

With the known analytic solution for adiabatic photon generation we can compute the retrieval efficiency η_R

$$\begin{aligned} \eta_R &= \int_{t_0}^{\infty} |\mathcal{E}_{\text{out}}|^2 dt \\ &= \eta_{\text{esc}} |L|^2 \int_{t_0}^{\infty} \partial_t h(t) \cdot e^{-2\Re(K \cdot h(t))} dt \end{aligned} \quad (\text{A.16})$$

$$\begin{aligned} &= \eta_{\text{esc}} \frac{|L|^2}{2\Re(K)} \left[e^{-2Kh(t \rightarrow \infty)} - e^{-2Kh(t_0)} \right] \\ &\approx \eta_{\text{esc}} \frac{|L|^2}{2\Re(K)} \end{aligned} \quad (\text{A.17})$$

Note that according to Ref. [36, 93] photon storage – instead of photon generation that is considered here – is described by the time-reversed process with the same efficiency.

Optimal control laser pulse In order to derive an expression for the required control laser pulse with time-dependent Rabi frequency $\Omega(t)$ we introduce the temporal shape of the outgoing photon [40].

$$e(t) = \sqrt{\eta_R}^{-1} \mathcal{E}_{\text{out}} \quad (\text{A.18})$$

Using Eq. (A.16) we obtain

$$\int_0^t |e(t')|^2 dt' = 1 - \exp(-2\Re(K)h(t)) \quad (\text{A.19})$$

$$|e(t)|^2 = 2\Re(K) |\Omega(t)|^2 \exp(-2\Re(K)h(t)) \quad (\text{A.20})$$

Eq. (A.20) provides an expression describing the modulus of the control laser Rabi frequency $\Omega(t)$:

$$|\Omega(t)| = \frac{1}{\sqrt{2\Re(K)}} \frac{|e(t)|}{\sqrt{\int_t^\infty |e(t')|^2 dt'}} \quad (\text{A.21})$$

In order to obtain the phase of the control laser pulse we note that $\mathcal{E}_{\text{out}}(t) = \sqrt{\eta_{\text{esc}}} L \Omega(t) \exp(-Kh(t))$ and obtain

$$\arg(\mathcal{E}_{\text{out}}) = \arg(e) = \arg(L) + \arg(\Omega) - \Im(K)h(t) \quad (\text{A.22})$$

Here \Im takes the imaginary part. Note that L is time-independent and thus contributes only a constant phase that can be omitted. Using Eq. (A.19) we rewrite

$$h(t) = \frac{-1}{2\Re(K)} \ln \left(\int_t^\infty |e(t')|^2 dt' \right) \quad (\text{A.23})$$

and obtain the time-dependent complex valued Rabi frequency $\Omega(t)$ that has to be applied on order to generate a single photon with arbitrary temporal shape in the adiabatic regime.

$$\Omega(t) = \frac{e(t)}{\sqrt{2\Re(K) \int_t^\infty |e(t')|^2 dt'}} \exp \left(-i \frac{\Im(K)}{2\Re(K)} \ln \left(\int_t^\infty |e(t')|^2 dt' \right) \right) \quad (\text{A.24})$$

Describing Photon Generation with an Effective Operator Formalism

Ref. [82] presents an effective operator formalism that describes the effective dynamics of a ground-state Hamiltonian upon adiabatic elimination of an excited state Hilbert sub-space. In order to apply this formalism to photon generation, we consider a combined Hilbert space $\mathcal{H} = \mathcal{H}_{\text{atom}} \otimes \mathcal{H}_{\text{cavity}} \otimes \mathcal{H}_{\text{t}}$ that considers the atomic state, the intra-cavity field as well as the transmission line [39]. A general state $|i, n_c, n_t\rangle =: |i\rangle \otimes |n_c\rangle \otimes |n_t\rangle$ describe an atom in state $|i\rangle$ and n_c (n_t) photons in the intra-cavity field (transmission line).

Restricting the number of excitations to one, the dynamics can be described via the five states as shown in Fig. B.1(a). In order to simplify the notation we define the following abbreviations $|1\rangle = |g_1, 0, 0\rangle$, $|2\rangle = |e, 0, 0\rangle$, $|3\rangle = |g_2, 1, 0\rangle$, $|4\rangle = |g_2, 0, 1\rangle$, $|5\rangle = |g_2, 0, 0\rangle$ and present the Hamiltonian in Eq. (B.1) following the notation of Ref. [82].

$$\begin{aligned}
 H &= H_g + H_e + V_+ + V_- & (\text{B.1}) \\
 H_g &= 0 \\
 H_e &= \Delta |2\rangle \langle 2| + \delta |3\rangle \langle 3| + g [|2\rangle \langle 3| + |3\rangle \langle 2|] \\
 V_+ &= \Omega(t) |2\rangle \langle 1| \\
 V_- &= (V_+)^{\dagger} = \Omega^*(t) |1\rangle \langle 2|
 \end{aligned}$$

In addition to the unitary evolution given by the Hamiltonian the system is subject to decay described by Lindblad type decay operators [62] shown below.

$$\begin{aligned}
 L_5 &= \sqrt{2\gamma/2} |5\rangle \langle 2| \\
 L_1 &= \sqrt{2\gamma/2} |1\rangle \langle 2| \\
 L_{\kappa_c} &= \sqrt{2\kappa_c} |4\rangle \langle 3| \\
 L_{\kappa_t} &= \sqrt{2\kappa_t} |5\rangle \langle 3|
 \end{aligned}$$

Here Δ denotes the single-photon detuning of the control laser beam from the atomic resonance and δ denotes the two-photon detuning of the cavity-resonance with respect to the control beam. In addition $\Omega(t)$ denotes the time-dependent control laser Rabi frequency and $(g, \kappa_c, \kappa_t, \gamma)$ are the CQED

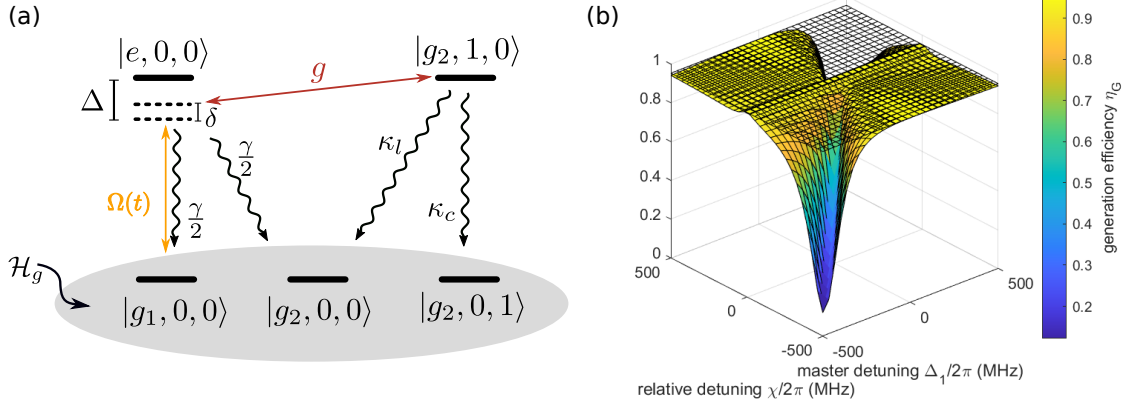


Figure B.1: (a) Relevant level diagram used to describe photon generation via an effective operator formalism. The solution is obtained by adiabatic elimination of the excited states which yields effective decay rates from the initial state $|g_1, 0, 0\rangle$ into the other ground-states. (b) Solution for the photon generation efficiency under two-tone driving conditions derived using the effective operator formalism. The figure shows a plot of Eq. (B.17) for two-photon resonance $\delta = 0$ and a relative field strength $\xi = 1$. The grid shows the maximally achievable efficiency of $2C/(2C + 1)$.

parameters. In order to find the effective dynamics via the effective operator formalism we compute the non-Hermitian Hamiltonian H_{NH}

$$\begin{aligned} H_{NH} &= H_e - \frac{i}{2} \sum_k L_k^\dagger L_k \\ &= \tilde{\Delta} |2\rangle \langle 2| + \tilde{\delta} |3\rangle \langle 3| + g [|2\rangle \langle 3| + |3\rangle \langle 2|] \end{aligned} \quad (\text{B.2})$$

Here the complex valued detunings are defined by $\tilde{\Delta} = \Delta - i\gamma$ and $\tilde{\delta} = \delta - i\kappa$. The next step consists in finding the inverse of the non-Hermitian Hamiltonian H_{NH}^{-1} :

$$H_{NH}^{-1} = \delta' |2\rangle \langle 2| + \Delta' |3\rangle \langle 3| - g' [|2\rangle \langle 3| + |3\rangle \langle 2|] \quad (\text{B.3})$$

Here the primed coefficients are defined as $\Delta' = \frac{\tilde{\Delta}}{\tilde{\Delta}\tilde{\delta} - g^2}$, $\delta' = \frac{\tilde{\delta}}{\tilde{\Delta}\tilde{\delta} - g^2}$ and $g' = \frac{g}{\tilde{\Delta}\tilde{\delta} - g^2}$ and have units of inverse frequency. Following the effective operator formalism we compute the effective Hamiltonian according to Eq. (B.4).

$$\begin{aligned} H_{\text{eff}} &= -\frac{1}{2} V_- \left(H_{NH}^{-1} + (H_{NH}^{-1})^\dagger \right) V_+ + H_g \\ &= -|\Omega|^2 \text{Re}(\delta') |1\rangle \langle 1| \end{aligned} \quad (\text{B.4})$$

$$L_{\text{eff}}^k = L_k H_{NH}^{-1} V_+ \quad (\text{B.5})$$

In addition to the effective unitary evolution that describes a light-shift induced by the control laser beam the effective evolution includes non-unitary decay channels given by the effective Lindblad operators defined in Eq. (B.5). The effective decay operators describe the dissipative branching from the excited state Hilbert space down to the ground state Hilbert space. The processes and their respective rates are summarized in Tab. B.1. In order to evaluate the expressions presented so far it is

process	effective decay operator	rate
dephasing	$L_{\text{eff}}^1 = \sqrt{\gamma} \delta' \Omega(t) 1\rangle \langle 1 $	$\Gamma_1 = \left \langle 1 L_{\text{eff}}^1 1 \rangle \right ^2 = \gamma \delta' ^2 \Omega ^2$
atomic decay	$L_{\text{eff}}^5 = \sqrt{\gamma} \delta' \Omega(t) 5\rangle \langle 1 $	$\Gamma_5 = \left \langle 5 L_{\text{eff}}^5 1 \rangle \right ^2 = \gamma \delta' ^2 \Omega ^2$
photon loss	$L_{\text{eff}}^{\kappa_l} = \sqrt{2\kappa_l} g' \Omega(t) 5\rangle \langle 1 $	$\Gamma_{\kappa_l} = \left \langle 5 L_{\text{eff}}^{\kappa_l} 1 \rangle \right ^2 = 2\kappa_l g' ^2 \Omega ^2$
photon generation	$L_{\text{eff}}^{\kappa_c} = \sqrt{2\kappa_c} g' \Omega(t) 4\rangle \langle 1 $	$\Gamma_{\kappa_c} = \left \langle 4 L_{\text{eff}}^{\kappa_c} 1 \rangle \right ^2 = 2\kappa_c g' ^2 \Omega ^2$

Table B.1: Effective processes and their respective rates.

useful to note the following properties of the primed variables shown in Tab. B.2. Here the variables $\alpha = \Delta\delta - \kappa\gamma - g'^2$ and $\beta = \Delta\kappa + \gamma\delta$ have been introduced in order to simplify the notation. In the

variable	$\text{Re}(\cdot)$	$\text{Im}(\cdot)$	$ \cdot ^2$
δ'	$\frac{\delta\alpha + \kappa\beta}{\alpha^2 + \beta^2}$	$\frac{\beta\delta - \kappa\alpha}{\alpha^2 + \beta^2}$	$\frac{\delta^2 + \kappa^2}{\alpha^2 + \beta^2}$
g'	$\frac{g\alpha}{\alpha^2 + \beta^2}$	$\frac{g\beta}{\alpha^2 + \beta^2}$	$\frac{g^2}{\alpha^2 + \beta^2}$
Δ'	$\frac{\Delta\alpha + \gamma\beta}{\alpha^2 + \beta^2}$	$\frac{\beta\Delta - \gamma\alpha}{\alpha^2 + \beta^2}$	$\frac{\Delta^2 + \gamma^2}{\alpha^2 + \beta^2}$

Table B.2: Properties of the primed variables.

following we compute the photon generation efficiency as the branching ratio of the wanted decay into the photon generation channel over all possible decay channels. The expression is shown in Eq. (B.6) and evaluated for two-photon resonance, i.e. $\delta = 0$. The obtained expression for the photon generation efficiency is equivalent to the efficiency derived in Ref. [39].

$$\begin{aligned}
 \eta_R &= \frac{\Gamma_{\kappa_c}}{\Gamma_1 + \Gamma_5 + \Gamma_{\kappa_c} + \Gamma_{\kappa_l}} = \frac{2\kappa_c |g'|^2}{\gamma |\delta'| + \gamma |\delta'| + 2\kappa_c |g'|^2 + 2\kappa_l |g'|} \\
 &= \frac{\kappa_c}{\kappa} \frac{2 |g'|^2}{2\gamma/\kappa |\delta'|^2 + 2 |g'|^2} = \frac{\kappa_c}{\kappa} \frac{2C}{2C + 1}
 \end{aligned} \tag{B.6}$$

B.1 Extension to a two-tone driving field

In order to describe photon generation with a bichromatic control laser field we make use of the *two-tone replacement* $\Omega \mapsto \Omega [1 + \xi \exp(-i\chi t)]$ introduced in Sec. 4.3. This replacement describes the Rabi frequency in the co-rotating frame of the *master beam* and includes the contribution from the *support beam* with a relative electric field strength ξ and a relative detuning $\chi = \omega_2 - \omega_1$ [87, 88]. For multiple drivings the perturbation term V is written as $V_-(t) = \sum_f V_-^{(f)} = \Omega^* |1\rangle \langle 2| \left(e^{+i\omega_1 t} + \xi e^{+i\omega_2 t} \right)$ and $V_+ = \sum_f V_+^{(f)}(t) = \Omega |2\rangle \langle 1| \left(e^{-i\omega_1 t} + \xi e^{-i\omega_2 t} \right)$. The effective Hamiltonian and the effective decay

operators are modified according to Eq. (B.7) and Eq. (B.8).

$$H_{\text{eff}} = -\frac{1}{2} \left[V_- \sum_f \left(H_{\text{NH}}^{(f)} \right)^{-1} V_+^{(f)}(t) + H.c. \right] + H_g \quad (\text{B.7})$$

$$L_{\text{eff}}^k = L_k \sum_f \left(H_{\text{NH}}^{(f)} \right)^{-1} V_+^{(f)}(t) \quad (\text{B.8})$$

The non-Hermitian Hamiltonian is now given by $\left(H_{\text{NH}}^{(f)} \right)^{-1} = \left(H_{\text{NH}} - \omega_f \right)^{-1}$ and takes the same form as previously but with different coefficients. The primed variables do now depend on the index $f = 1, 2$ and are shown below. Here the detunings are defined as $\tilde{\Delta}_f = \omega_e - \omega_f - i\gamma$ and $\tilde{\delta}_f = \omega_c - \omega_f - i\kappa$.

$$\delta'_f = \frac{\tilde{\delta} - \omega_f}{(\tilde{\Delta} - \omega_f)(\tilde{\delta} - \omega_f) - g^2} = \frac{\tilde{\delta}_f}{\tilde{\Delta}_f \tilde{\delta}_f - g^2} \quad (\text{B.9})$$

$$\Delta'_f = \frac{\tilde{\Delta} - \omega_f}{(\tilde{\Delta} - \omega_f)(\tilde{\delta} - \omega_f) - g^2} = \frac{\tilde{\Delta}_f}{\tilde{\Delta}_f \tilde{\delta}_f - g^2} \quad (\text{B.10})$$

$$g'_f = \frac{g}{(\tilde{\Delta} - \omega_f)(\tilde{\delta} - \omega_f) - g^2} = \frac{g}{\tilde{\Delta}_f \tilde{\delta}_f - g^2} \quad (\text{B.11})$$

Next we compute the effective Hamiltonian according to the definition in Eq. (B.7).

$$\begin{aligned} H_{\text{eff}} &= -\frac{1}{2} \left[\Omega^* |1\rangle \langle 2| (e^{i\omega_1 t} + \xi e^{i\omega_2 t}) \right] \times \\ &\quad \left[\delta'_1 \Omega e^{-i\omega_1 t} |2\rangle \langle 1| + \delta'_2 \Omega \xi e^{-i\omega_2 t} |2\rangle \langle 1| - g'_1 \Omega e^{-i\omega_1 t} |3\rangle \langle 1| - g'_2 \Omega \xi e^{-i\omega_2 t} |3\rangle \langle 1| \right] + H.c. \\ &= -\frac{1}{2} |\Omega|^2 |1\rangle \langle 1| \left[\delta'_1 (1 + \xi e^{i(\omega_2 - \omega_1)t}) + \delta'_2 \xi (1 + \xi e^{-i(\omega_2 - \omega_1)t}) \right] + H.c. \\ &= -|\Omega|^2 |1\rangle \langle 1| \text{Re} \left[\delta'_1 (1 + \xi e^{i(\omega_2 - \omega_1)t}) + \delta'_2 \xi (1 + \xi e^{-i(\omega_2 - \omega_1)t}) \right] \end{aligned} \quad (\text{B.12})$$

Note that as long as the real part in Eq. (B.12) is zero, there is no net light-shift induced by the control laser beam. This is for example reached for the ‘‘symmetric configuration’’ where $\Delta_1 = -\Delta_2$. In this case one finds $\alpha_1 = \alpha_2$ and $\beta_1 = -\beta_2$. The light shift drops to zero for the case of $\xi = 1$. The effective decay operators are found to be

$$L_{\text{eff}}^1 = \sqrt{\gamma} \Omega(t) |1\rangle \langle 1| \left[\delta'_1 e^{-i\omega_1 t} + \delta'_2 \xi e^{-i\omega_2 t} \right] \quad (\text{B.13})$$

$$L_{\text{eff}}^5 = \sqrt{\gamma} \Omega(t) |5\rangle \langle 1| \left[\delta'_1 e^{-i\omega_1 t} + \delta'_2 \xi e^{-i\omega_2 t} \right] \quad (\text{B.14})$$

$$L_{\text{eff}}^{\kappa_c} = \sqrt{2\kappa_c} \Omega(t) |4\rangle \langle 1| \left[g'_1 e^{-i\omega_1 t} + g'_2 \xi e^{-i\omega_2 t} \right] \quad (\text{B.15})$$

$$L_{\text{eff}}^{\kappa_l} = \sqrt{2\kappa_l} \Omega(t) |5\rangle \langle 1| \left[g'_1 e^{-i\omega_1 t} + g'_2 \xi e^{-i\omega_2 t} \right] \quad (\text{B.16})$$

and the effective rates are summarized in Tab. B.3. In order to compute the photon retrieval efficiency $\eta_R = \frac{\Gamma_{\kappa_c}}{\Gamma_1 + \Gamma_5 + \Gamma_{\kappa_c} + \Gamma_{\kappa_l}}$ we have to evaluate the time-dependent expressions for the rates. In principle one has to constrain the time to a duration T at which the initial population was transferred

process	rate
dephasing	$\Gamma_1 = \left \langle 1 L_{\text{eff}}^1 1 \rangle \right ^2 = \gamma \left \delta'_1 + \delta'_2 \xi e^{-i(\Delta_2 - \Delta_1)t} \right ^2 \Omega ^2$
atomic decay	$\Gamma_5 = \left \langle 5 L_{\text{eff}}^5 1 \rangle \right ^2 = \gamma \left \delta'_1 + \delta'_2 \xi e^{-i(\Delta_2 - \Delta_1)t} \right ^2 \Omega ^2$
photon loss	$\Gamma_{\kappa_l} = \left \langle 5 L_{\text{eff}}^{\kappa_l} 1 \rangle \right ^2 = 2\kappa_l \left g'_1 + g'_2 \xi e^{-i(\Delta_2 - \Delta_1)t} \right ^2 \Omega ^2$
photon generation	$\Gamma_{\kappa_c} = \left \langle 4 L_{\text{eff}}^{\kappa_c} 1 \rangle \right ^2 = 2\kappa_c \left g'_1 + g'_2 \xi e^{-i(\Delta_2 - \Delta_1)t} \right ^2 \Omega ^2$

Table B.3: Effective processes and their respective rates for two tone driving.

completely. However demanding that $\int_0^T \Gamma_1 + \Gamma_5 + \Gamma_{\kappa_c} + \Gamma_{\kappa_l} dt = 1$ yields an expression of the form $A \cdot T + B \cos((\Delta_2 - \Delta_1)T) + C \sin((\Delta_2 - \Delta_1)T) + D = 1$. In order to circumvent this problem we perform a *mean rate approximation* and drop the oscillating contribution of the rates. This is justified, since the oscillating contribution averages to zero on a time-scale much faster than the photon generation process. We then find an expression for the photon retrieval efficiency shown in Eq. (B.17). Here $\bar{\Gamma}_x$ denotes the mean of Γ_x . A plot of Eq. (B.17) is provided in Fig. B.1(b) as function of the master beam detuning Δ_1 and the relative detuning χ for a relative field strength of $\xi = 1$ and two-photon resonance $\delta = 0$.

$$\begin{aligned}
 \eta_R &\approx \frac{\bar{\Gamma}_{\kappa_c}}{\bar{\Gamma}_1 + \bar{\Gamma}_5 + \bar{\Gamma}_{\kappa_c} + \bar{\Gamma}_{\kappa_l}} \\
 &= \frac{2\kappa_c \left(|g'_1|^2 + \xi^2 |g'_2|^2 \right)}{2\gamma \left(|\delta'_1|^2 + \xi^2 |\delta'_2|^2 \right) + 2\kappa \left(|g'_1|^2 + \xi^2 |g'_2|^2 \right)} \quad (\text{B.17})
 \end{aligned}$$

Photon generation efficiency for two-tone driving In Fig. B.1(b) it is shown that for certain parameter choices of two-tone driving the photon generation efficiency approaches the limit given by $2C/(2C + 1)$, which was also derived for single-tone driving. No enhancement to even higher efficiencies is observed. However for $\Delta_1 \approx \chi$ which implies $\Delta_2 \approx 0$ the efficiency is strongly reduced. This can be understood by noting that we have here assumed two-photon resonance ($\delta = 0$) of the cavity resonance with the *master* beam. However for $\Delta_2 = 0$ the atom is resonantly driving by the support beam which is highly two-photon off-resonant with respect to the cavity. The photon generation efficiency is reduced, since the scattering of the support beam dominated with respect to the coupling of the master beam. This effect is discussed in more detail in the main text in Sec. 4.3.

Acknowledgements

First of all, I would like to thank Prof. Dieter Meschede for giving me the opportunity to join his research group. I am thankful for the opportunity to extend theoretical knowledge with hands-on lab experience throughout my master studies. The lab work and daily discussions during the master thesis, furthermore, provided great insight into the fascinating field of quantum optics. In addition, I thank Prof. Simon Stellmer for being my second advisor.

I am grateful to Dr. Wolfgang Alt for countless enlightening discussions about the modelling of physical processes, data analysis and the design of electronic circuits. The detailed explanations clarified many technical steps in a comprehensive and also understandable way.

A big thanks goes to Eduardo Uruñuela for teaching me the lab basics and for the numerous discussions of measurements. The lab team is completed by Pooja Malik and Lukas Ahlheit, whom I sincerely thank for many scientific discussions and the enjoyable office atmosphere. Together we implemented many technical improvements and took data at a remarkable rate.

Likewise, I want to thank Dr. Deepak Pandey and Dr. Hannes Pfeifer for many discussions and useful suggestions. Moreover, I would like to thank Dr. Andrea Alberti for granting me access to the computing machine, that I used extensively for numerical calculations.

Furthermore, I want to thank the whole group for their support and the borrowed equipment. I am thankful to everyone involved in proofreading this thesis.

Finally, I want to thank my parents for their unconditional support.